CARBON, CAPTURE & STORAGE

THE BEHAVIOUR OF CO_2 IN CONTROL VALVES FOR CARBON SEQUESTRATION

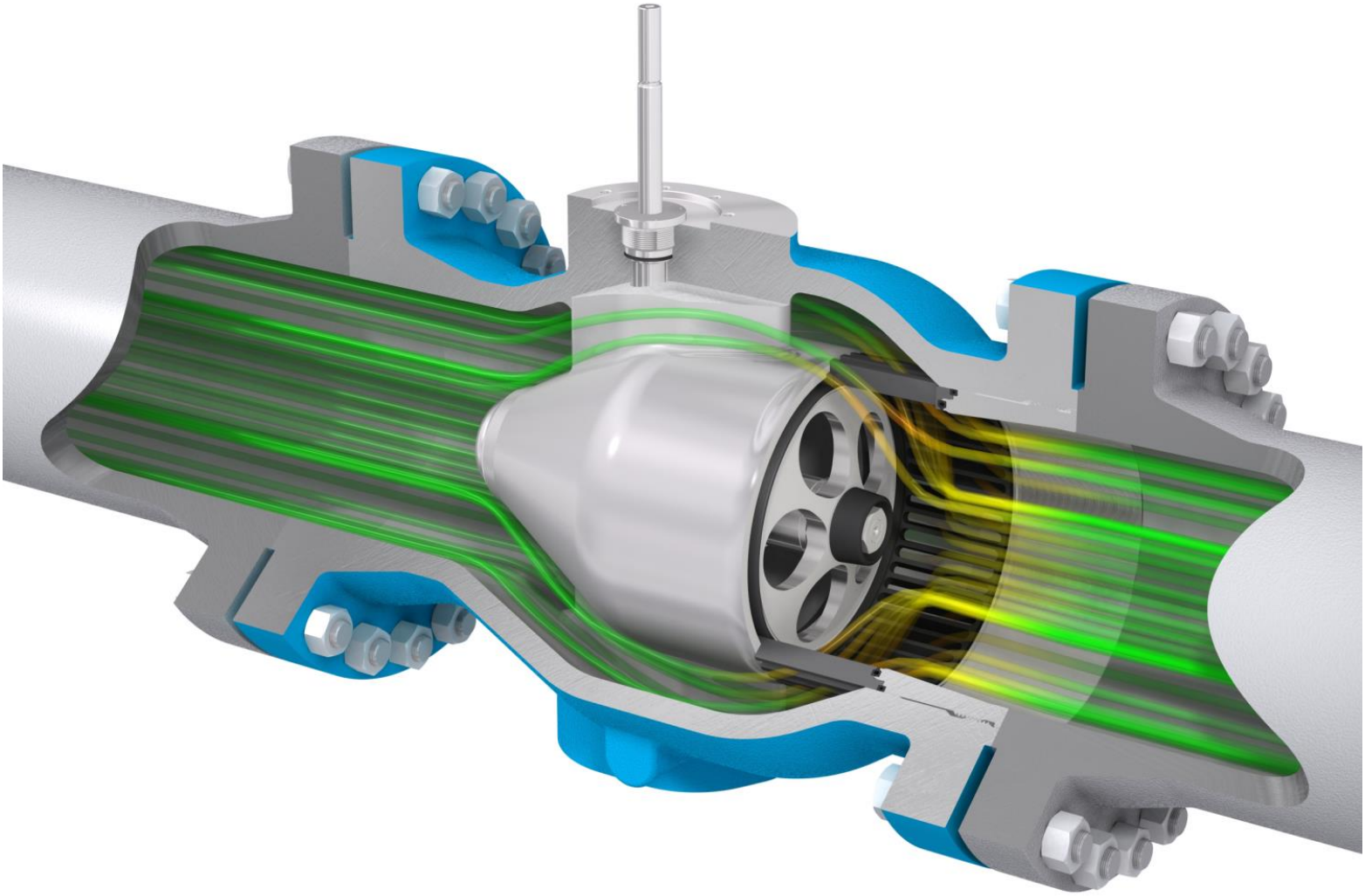

TU Delft TNO B.S. FLUTTERT

A numerical study of the behaviour of carbon dioxide in control valves for optimising carbon sequestration

by

Bob Sebastiaan Fluttert

Master thesis submitted to Delft University of Technology
in partial fulfilment of the requirements for the degree of

Master of Science
in Mechanical Engineering

to be publicly defended on Friday October 21st, 2022 at 09:30.

Student:	B.S. Fluttert	
Student number:	4393422	
Contact:	bob.fluttert@gmail.com	
Thesis committee:	Prof.Dr.ir. R. Pecnik	TU Delft, supervisor
	Dr.ir. W.-P. Breugem	TU Delft, supervisor
	Dr. A. Twerda	TNO, supervisor
	Dr.ir. M.J.B.M. Pourquie	TU Delft

A numerical study of the behaviour of carbon dioxide in control valves for optimising carbon sequestration

Abstract

The Intergovernmental Panel on Climate Change (IPCC) believes that multiple solutions must be deployed simultaneously to reduce the emission of greenhouse gases into the atmosphere. Carbon, Capture & Storage (CCS) is an unavoidable technique within this portfolio as an intermediate solution. CCS requires transport of CO_2 through pipeline systems and into wells. There are still large uncertainties on the thermodynamics of the CO_2 in flow through valves. The CO_2 flow undergoes significant changes in pressure, temperature and phase distribution when it passes this control valve. Therefore, the behaviour of the CO_2 flow flowing through a control valve is examined in this study.

The simulation of CO_2 in a 3D valve including phase transitions is complex. Furthermore, few validation experiments are available. As a first step, more simple nozzles are simulated. In these devices, the same processes occur and validation data is available. These simulations are validated with experimental data by Nakagawa et al. [1] [2] to examine the accuracy. Three types of models (isenthalpic, Euler and Enhanced Mass Transfer (EMT)) are implemented in increasing levels of complexity to investigate the differences between these models and to consider when complexity is needed or simplifications are valid.

The validation cases show experimental pressure data of high-pressure CO_2 flow through converging-diverging nozzles with phase transitions. The results showed that the EMT model matched the experimental data best. A substantial similarity was achieved regarding the pressure data. The mass transfer mechanism, however, needed adjustments in its coefficients to match the experimental data. Finally, after finding the right values, the EMT shows the best technique for modelling flashing or cavitation.

In short, the overall consequences of the transition in a valve are substantial and must be considered. The behaviour of the high-pressure CO_2 flow is heavily influenced by flowing through a valve. Substantial amounts of vapour are formed, but only after the throat. This is the same for choking condition, which is achieved in the diverging section of the nozzle. The large expected drop in temperature due to pressure reduction has also been noted.

Although a high degree of similarity between the results of the model with experimental data is obtained, there is room for improvement regarding the model. A flaw was discovered in the handling of the thermodynamic properties of the fluid near critical points. Also, the surface tension has not been considered, but might have a substantial influence. Next steps in the research are 2D and 3D simulations of actual valves, but require experimental validation data.

Acknowledgements

I want to express my gratitude to all who have contributed to making this study possible. Working with many intelligent and sophisticated people on this project, which I find greatly interesting, has been a privilege.

Firstly, I would like to sincerely thank my supervisors at the TU Delft, Prof.Dr.ir. R. Pecnik and Dr.ir. W.-P. Breugem. Their expertise in the field of study helped me to focus on the relevant elements and they have encouraged me all the time in my academic research. Also, I'd like to recognise the assistance I got in coding from R. Pecnik. This helped to keep the momentum going and not concentrate too long on less important matters.

Also, I would like to express profound appreciation to my supervisor at TNO, Dr. A. Twerda, for providing constructive criticism of my work throughout the project and keeping me on track. Moreover, special thanks to Dr. D. van Nimwegen at TNO who gave me new insights at critical points in the process. Their support together during the weekly progress meetings was truly valuable.

At last, the image at the front page was used by courtesy of Mokveld Valves BV. For this, I would like to thank them.

B.S. Fluttert
Delft, October 2022

Contents

List of Figures

List of Tables

Nomenclature

Latin symbols

A	Area	[m^2]
c_p	Specific heat capacity at constant pressure	[kJ/(kg K)]
c_v	Specific heat capacity at constant volume	[kJ/(kg K)]
c	Speed of sound	[m/s]
e	Specific internal energy	[kJ/kg]
F_{cond}	Condensation coefficient	[-]
F_{vap}	Vaporisation coefficient	[-]
G	Mass flow	[kg/s]
h	Specific enthalpy	[kJ/kg]
M	Mach number	[-]
n_{b}	Bubble density	[-]
p	Pressure	[Pa]
R_{B}	Bubble radius	[m]
s	Specific entropy	[kJ/(kg K)]
T	Temperature	[K]
u	Velocity	[m/s]
v	Specific volume	[m^3/kg]
x	Quality	[-]

Greek symbols

α	Volume fraction	[-]
α_{nuc}	Nucleation site volume fraction	[-]
ϵ	Turbulence dissipation	[J/(kg s)]
Γ	First Grüneisen parameter	[-]
γ	Surface tension	[N/m]
κ	Turbulent kinetic energy	[J/kg]
λ	Thermal conductivity	[W/(m K)]
μ_{JT}	Joule-Thomson coefficient	[K/bar]
μ	Dynamic viscosity	[kg/(m s)]
ν	Kinematic viscosity	[m^2/s]
ρ	Density	[kg/m^3]
θ	Nozzle divergent angle	[degrees]

Subscripts

$*$	Sonic conditions
k	Arbitrarily phase
l	Liquid phase
m	Mixture
sat	Saturated state
t	Total conditions
v	Vapour phase

Abbreviations

1D One Dimensional

2D Two Dimensional

3D Three Dimensional

AUSM Advection Upstream Splitting Method

CFD Computational Fluid Dynamics

CO_2 Carbon dioxide

EMT Enhanced Mass Transfer

EOS Equation of State

GUI Graphical User Interface

HEM Homogeneous Equilibrium Model

RANS Reynolds-Averaged Navier-Stokes

RGP Real Gas Properties

RHS Right Hand Side

SST Shear Stress Transport

SVA Source Variable Area

SW Span and Wagner

TUI Text-based User Interface

Chapter 1

Introduction

1.1 Societal relevance

Human actions unequivocally influence the current state of the climate [3]. These activities have caused rapid changes in temperature in the atmosphere, the ocean, and land. This climate change has already affected many weather extremes in every region globally and heavily increased the level of greenhouse gasses in the atmosphere. If global warming continues, every location is expected to see several changes in climatic impact drivers simultaneously. Limiting this human-induced global warming requires restricting CO_2 emissions, as it is the most significant contributor to the rise of greenhouse gasses.

Carbon Capture & Storage (CCS) can reduce the atmospheric level of CO_2. The Intergovernmental Panel on Climate Change (IPCC) states that no single technology alone will provide all of the emission reduction; instead, a portfolio of many technologies is needed. In addition, CCS can reduce overall mitigation costs and increase flexibility in greenhouse gas emission reduction. This interest in CCS arises from the world's significant dependence on fossil fuels today (about 80% of global energy use). Also, the ability of CCS to cut down CO_2 emissions in the short term is of great interest. Moreover, there is no need for a whole new infrastructure as CCS is compatible with current energy infrastructures [3]. Therefore, it is necessary to investigate this topic further along with many other possible technologies.

However, CCS is one of the more controversial options in climate change policy. Arguments usually arise when the roll-out of CCS is discussed: how does CCS compare (if deployed in the Netherlands) with other reduction options, what is the social and political support base, and who pays the bill for the various options? These differences of opinion can easily lead to a stalemate, with the option not being developed or being developed much too late. This risk is particularly acute for technology like CCS, as it is an option that requires immediate and relatively large-scale investment in equipment.

There is widespread agreement that CCS can only be successfully introduced if

there is broad support for the option and its specific role in the energy transition. Although there are many objections to CCS, almost all scientific studies show that it is an inevitable option for keeping global warming below 1.5 to 2 degrees Celsius, as agreed in the Paris climate accord [4]. Hence, CCS will take on the role of a temporary solution, allowing more time for the transition to carbon-neutral solutions.

1.2 Present developments

In 2020, there were 13 (1 in Ireland, 1 in The Netherlands, 4 in Norway, 7 in the United Kingdom) commercial CCS facilities working or in different levels of construction across Europe [5]. Also, more than eleven commercial parties are planning to operate before 2030. One of the more advanced programs is a project in the Netherlands called Porthos where they are planning to be in operation from 2024. The following information regarding this project is reported using the information on their website [6].

Porthos is developing a project whereby CO_2 from industry in the port of Rotterdam is collected, transported and stored in depleted gas fields under the North Sea. The CO_2 can originate from several companies that capture it directly from their plants. The companies deliver their CO_2 to a collector through the Rotterdam port area. Next, this CO_2 is then compressed at a station near shore. The CO_2 is transported by undersea pipelines to a platform in the North Sea, roughly 20 km off the coast. From the platform, the CO_2 is pumped into empty gas fields. The empty gas fields are located in a closed reservoir, more than 3 km under the North Sea. Porthos will store about 37 Mton CO_2, about 2.5 Mton CO_2 per year for the coming 15 years [6]. In comparison, the annual CO_2 emission in the Netherlands was 138 Mton in 2021, which means that Porthos can store 1.8% of that per year [7]. Figure 1.1 shows a visual representation of the project.

1.3 Classification

The CCS chain can best be categorised into three subsystems: capture, transportation, and storage. There are still numerous challenges and uncertainties to be investigated in every segment. For instance, capturing CO_2 directly from existing fossil fuel-burning plants is challenging. At sub-surface storage sites, there are concerns that the CO_2 could leak into the environment and eventually even contribute to the climate problem. Similarly, there are obstacles to the transportation of CO_2.

Although the CCS chain has been used for enhanced oil recovery (EOR) for a long time, it has only recently been investigated for climate change mitigation [8]. Various CO_2 capture and separation systems are used to extract CO_2 from significant polluters, such as fossil-fuel power plants. Next, it is compressed, purified,

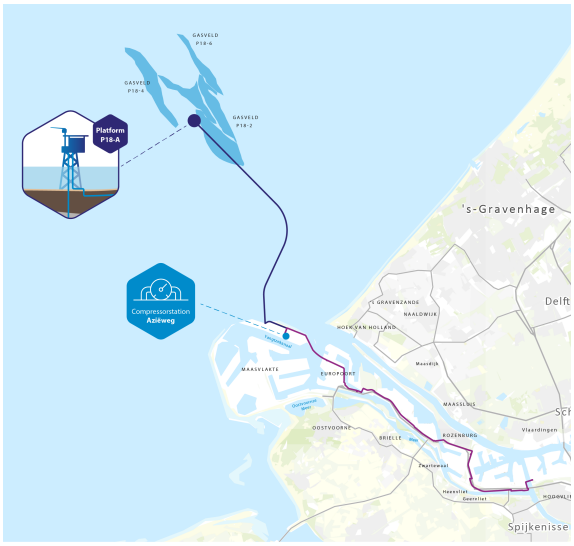

Figure 1.1: Map of the Porthos project in the Netherlands. The purple lines represent the collected CO_2 in on-land pipelines, whereas the dark blue lines represent the underwater pipelines. Image is taken from the website of Porthos [6].

and transported to a sub-surface storage site. Here it is injected underground and stored for an extended period, usually in an empty oil and gas reservoir or deep saline aquifer. This CO_2 can be transported through a pipeline (dense phase) or trucks, rail, and ships (liquid phase) depending on the phase of CO_2 [8].

The transportation of CO_2 in the pipelines is similar to that of the oil and gas industry in many ways but reversed. These sectors are well understood and heavily researched in multiphase flow modelling. The CCS chain should be able to benefit from this experience. Although using the same system is not a complication, CO_2 differs from the oil-gas flow. For example, carbon dioxide behaves differently during transport because of the contrast in thermodynamic properties like compressibility and the Joule-Thomson coefficient. Also, pressures and temperatures are more often in the vicinity of the critical point and the phase line than hydrocarbons. This means that appearances like phase transitions and supercritical conditions must be considered.

The ability to operate CO_2 transport safely and cost-effectively is crucial. Therefore, testing this technology is of importance, both experimentally and numerically. Accurate models that anticipate CO_2 behaviour are required to design safe pipelines. Experimental operations must be used to validate these models. A high degree of similarity between these two should mean full-scale projects can be operated safely and are predictable.

1.4 Challenges of pipeline CO_2 transport

To ensure the transportation takes place in the dense phase, the CO_2 is often compressed to high pressures. Depressurisation in the pipeline can arise due to a calamity, prepared maintenance, or during the transition in a valve where the flow can become choked [9]. This depressurisation can generate a phase transition and temperature drop in the fluid. Here, a decrease in temperature results from a high Joule-Thomson coefficient and causes the material of the pipe or the valve to become brittle and coatings to lose their functionality [10]. Hence, transporting the CO_2 in the dense phase also involves potential problems besides its advantages.

Pressure and mass flow rate control are an absolute necessity at the wellhead. Although the transportation in the pipelines takes place at high pressures, this pressure must be reduced here to make sure that the pressure at the bottom of the well is not too high. On the other hand, it must overcome the reservoir pressure to provide a driving force. Also, the flow rate must be controlled for both normal startup operations and accidental events. For these reasons, a valve is implemented to control these operations both directly and indirectly.

In transportation applications, choked flow can occur when pressure is reduced through the control components. The cross-sectional areas of the inlet and exit of a valve are substantially larger than the control area. Because the total flow is constant throughout the valve, the liquid velocity in the smallest region (vena contracta) must be substantially higher to pass the same flow. The fluid accelerates as it passes past the restriction, decreasing the pressure at that point. Vapour bubbles will emerge if the instantaneous pressure in the vena contracta falls below the vapour pressure. The fluid volume grows as it is converted to vapour, which restricts flow. This effect will grow to the point where flow throughput cannot be increased anymore, regardless of how low the downstream pressure is decreased. This phenomenon is called choked flow.

Additional complexity arises when the CO_2 emitting power plants will have a varying load, which they are likely to have. This variation alters CO_2 production rates over time and can be challenging to handle [11]. Transient cases are another issue for pipelines and injection wells, such as shut-ins and uncontrolled depressurisations. A final concern involves the transport of CO_2 in the presence of impurities. These impurities change the fluid properties and can significantly impact the flow behaviour. Although it strongly depends on the capturing process, CO_2 in the context of CCS operations usually indicates a multi-component CO_2 rich mixture [12]. Ensuring successful transport of this fluid even though its potential hazards is often called flow assurance [9].

1.5 Problem Statement

CCS is of great importance since it will be a crucial factor in reducing human-induced CO_2 emissions in line with the EU regulations and the Paris agreement. Accurate models are vital for the safe design and optimal operation of CO_2 transport systems. Properties of CO_2 differ significantly from oil and natural gas for which current infrastructure is built. Therefore, both experimental and numerical investigations are necessary to test this technology.

Several challenges were highlighted during the transport stage of CO_2 to the storage sites. Transient cases must be considered, a varying load can bring additional complexities, and even the slightest impurities can influence the behaviour of the CO_2. In addition, valves were indicated as an essential part of the transport infrastructure. In these valves, fast phase changes occur because of the pressure and temperature drop. This has an influence on the mass flow through the valve and heat transfer between the fluid and the wall. It was noted that this could introduce complexities to the infrastructure.

Little is known about the exact flow behaviour of CO_2 in these situations. The understanding of the behaviour of CO_2 across a valve with accurate flow distribution and thermodynamic characteristics is still inadequate. However, since it is of great importance, this will be the spotlight of this thesis. Therefore, the research question of this study will be:

"How is the behaviour of a CO_2 flow influenced by passing through a control valve, and what are the consequences for the CCS operations?"

To answer this research question, it will be divided into several sub-goals. First, the underlying physics must be understood. This will be performed with one-dimensional numerical simulations to examine the valve's flow behaviour upstream, in, and downstream. This can be done with relatively simple methods, but also complex mass transfer effects can be incorporated into these simulations. The complexity will increase within these 1D models to replicate the effects of an actual valve in a complete way. What can be learned from these simulations must be discussed using the similarity with experimental data.

1.6 Rationale and Structure of Study

In this work, simulations of high-pressure CO_2 are performed, and the flow through valves will be discussed. Effects of this transit are presented and, if possible, compared. This work will emphasise the pressure, temperature and mass flow effects. As will be discussed, the flow through valves can have a significant impact on all of these

three parameters. This effect is investigated numerically in this work. Furthermore, phase change mechanisms can occur and will be presented and discussed.

The simulations in this research are carried out in multiple numerical models. Some of these models were made and extended based on previous versions by Prof.Dr.ir. R. Pecnik. This significantly reduced the computing time of these models and allowed to focus on the extensions that had to be made.

First, in Chapter 2, the theoretical background is given of the underlying and relevant physics that takes place in this work. The numerical methodology of this study is set out in Chapter 3. The consecutive results are presented in Chapter 4. Furthermore, they will be compared to reference cases and discussed in the context of the theory set out in 2. Conclusions will be drawn in Chapter 5, and lastly, recommendations and suggestions for future work are included in Chapter 6.

Chapter 2

Theoretical Background

Both experimental and numerical analyses can be used to predict the behaviour of carbon dioxide in control valves. These predictions are crucial to designing industrial-scale CCS projects, as described in Chapter 1. A good agreement between the experiments and numerics implies a proper understanding of the actual events. This chapter will present an overview of the underlying physics that form the basis for the behaviour. Also, previous work into CO_2 flow will be discussed in a separate section.

2.1 Physical Modelling

For more than 50 years, multiphase flow has been actively investigated. The energy sector has been a significant driver of this development. For example, multiphase flow is critical in reactor cooling systems in the nuclear industry. The RELAP model, designed by the United States Nuclear Regulatory Commission, is now the industry guideline for modelling multiphase flow in water-cooled reactors [13]. Pipeline models that enable safe and cost-effective oil and gas transportation have long been needed in the petroleum sector. This study has resulted in methods for dynamic pipeline modelling of multiphase (oil-gas-water) flow. The dynamic multiphase flow simulator OLGA is an example of such a tool [14].

Several unique properties of CO_2 transport distinguish it from oil and gas transport in modelling. The triple point (517 kPa at 216.55 K) and critical point (7.38 MPa at 304.13 K) of carbon dioxide differ from those of hydrocarbons. CO_2 will usually be transported in the dense state (liquid or supercritical), which is different for natural gas. Another distinction must be made regarding its composition. Whereas gas and oil are never pure fluids, the transported CO_2 is often very pure. In a pressure-temperature diagram like Figure 2.1, CO_2 has a phase line, while hydrocarbons have a significant phase envelope. Hydrocarbons, therefore, do not depressurise along a phase line, and pressure and temperature are not tightly coupled as for CO_2. Although it is out of the scope of this thesis, it is good to point out that

even minute contaminants can significantly impact the mixture's thermodynamic and transport characteristics [15].

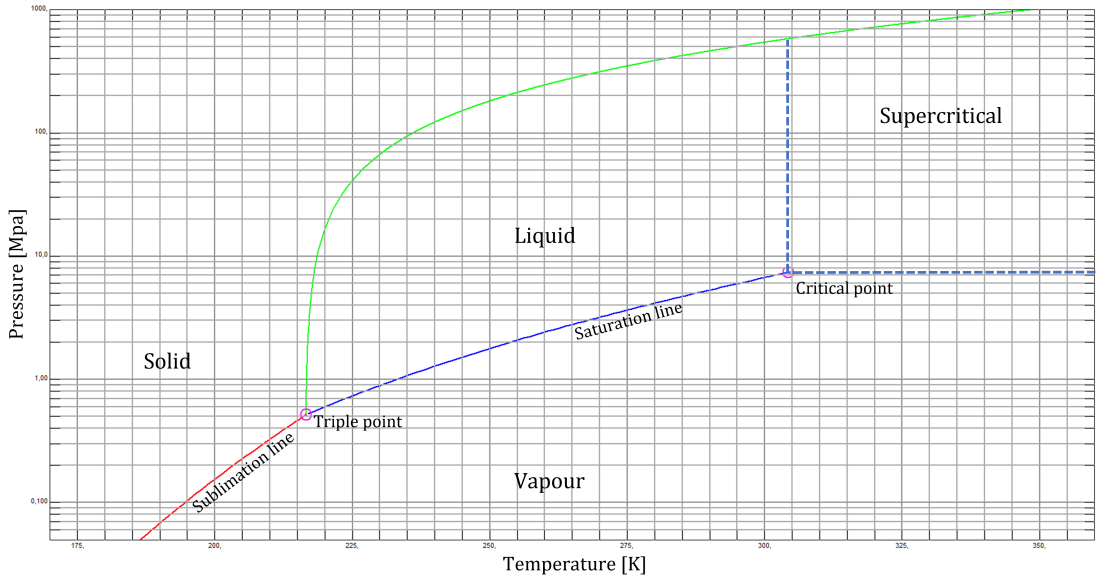

Figure 2.1: Phase diagram of CO_2 with temperatures from 170K to 360K and pressures from 0.1 MPa to 1000 MPa. The red, green, and blue lines represent the sublimation, melting, and saturation lines respectively. The triple and critical points are denoted by a purple circle.

Additionally, the viscosity and surface tension of CO_2 are noteworthy. Viscosity plays an essential role in flow behaviour during transport and strongly depends on temperature, especially near the critical point. When comparing this property with respect to other fluids, CO_2 has a relatively low viscosity. Whereas for water and oil condensates the viscosity is 1 mPa·s and 2 mPa·s at 293 K, respectively, for liquid CO_2 it is much lower: 0.07 mPa·s at 293 K. The surface tension is also low compared to these other fluids: 73 mN/m for air-water, 30 mN/m for air-oil condensates at 293 K and 1 atm and only 1 mN/m for CO_2 in the two-phase state (293 K and 60 bar) [16].

Another thermodynamic property of CO_2 must be highlighted. During depressurisation, there is often a change in temperature as well. This change in temperature because of the change in pressure is denoted by the Joule-Thomson coefficient:

$$\mu_{\mathrm{JT}} = \left(\frac{\partial T}{\partial P}\right)_H . \tag{2.1}$$

The value of this coefficient is often expressed as °C/bar and is both pressure and temperature dependent for each substance. CO_2 experiences a relatively high coefficient during expansion along the phase boundary. This can be seen in Figure 2.2

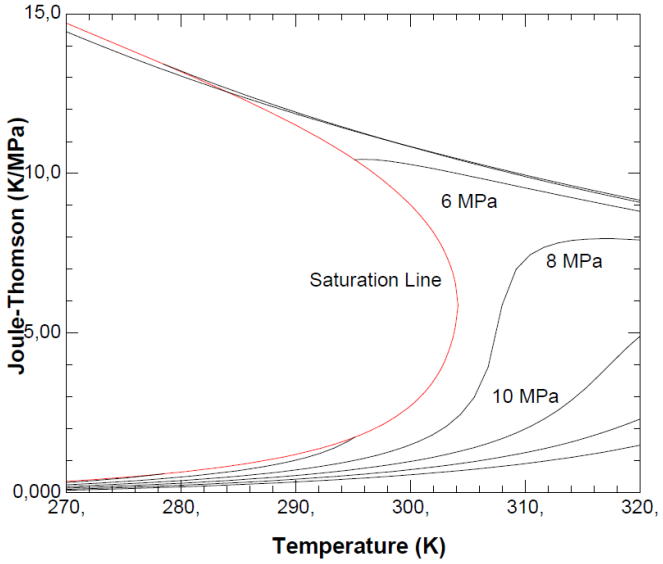

Figure 2.2: Isobars plotted in a diagram where the Joule-Thomson coefficient is shown with respect to the temperature. The red crossed line denotes the phase boundary (liquid and vapour saturation line).

In Figure 2.2, the Joule-Thomson coefficient is always positive for the isobars that are plotted (2 to 14 MPa). According to Equation 2.1, this means that the change in temperature must also be negative since the change in pressure during an isenthalpic expansion is negative too. Hence, CO_2 will cool during an isenthalpic expansion. This cooling effect is relatively strong for CO_2 compared to hydrocarbons. Where CO_2 can experience 1 °C/bar, natural gas only cools 0.5 °C/bar

Next to the differences between CO_2 and hydrocarbons and the presence of impurities, the distinction between steady-state and time-dependent (transient) simulations should be considered. As noted before, the favourable transport conditions of CO_2 are located in the dense phase since this is the most transport-efficient state: higher density, so smaller pipelines are sufficient to transport the CO_2 [17]. Pressure drop calculations can be performed with a simple correlation for friction factors when considering only this phase under normal operating conditions [18]. These can easily be found in textbooks like those of White [19]. However, some CO_2 sources, like electricity-generating power plants, will fluctuate since they are run in response to independent needs. This will result in a transitory CO_2 flow in the pipeline, and the pressure will fluctuate due to the volatile mass flow, and the state of the pipeline may shift from single-phase to two-phase [11]. However, change in phase is more common in a well. Typically, wells are closed to prevent depressurising the pipeline.

The transients also occur during start-up, shutdown or accidents. Hence, applying the steady-state methodology will be highly inappropriate. During matters of depressurisation, a decompression wave will emerge. This wave will cause a phase

change in the dense phase. Due to this phase change, the following cooling may cause embrittlement and cracking of the pipe material [10]. As a result, accurate estimates of depressurisation and cooling are critical for ensuring a CCS pipeline's safe and dependable operation.

Depressurisation waves propagate at the local sound velocity of the fluid in transportation. For a single-phase fluid, this property can easily be determined. However, the multiphase sound speed is responsive to various physical equilibrium assumptions. Consequently, it is necessary to include the speed of sound in a simulation in a physically realistic manner to resolve the transient events appropriately [20]. Different models for the speed of sound will be discussed in subsequent sections.

It is also worth noting that a simulation's precision is controlled not just by the precision of the physical model, but also by the capacity of the numerics to properly resolve the underlying model. [18]. Numerical diffusion linked with specific numerical approaches has been proven to have a negative impact on the resolution of a depressurisation wave in a pipeline [21][22].

2.2 Flashing Flow Modelling

Before exploring the physics and the numerical methods for the modelling of flashing flows, first, the definition of flashing must be understood. Also, the differences and agreements with cavitation must be clear. Flashing and cavitation are both processes where the local pressure of a liquid drops below the vapour pressure. As mentioned before, this happens at the vena contracta. If the flow downstream of the vena contracta remains below this vapour pressure, it is called flashing. On the other hand, it is called cavitation if the local pressure downstream regains above the vapour pressure. In the latter, shock waves can emerge from the bubble implosions. This can lead to severe damage to the equipment as these implosions create microjets that impinge on components. With flashing, these effects are less extreme. The damage caused by both flashing and cavitation is called erosion. The differences between cavitation and flashing are also schematically depicted in Figure 2.3.

A substantial quantity of material has been produced to model two-phase mixtures created by the flashing process since the middle of the past century [24]. Most research concentrates on the critical flow rate because of its security importance. This critical rate exists when the flow is choked. The Bernoulli equation for single-phase fluids usually overestimates this, whereas the homogeneous equilibrium equation underestimates it [25].

Modelling two-phase flow non-equilibrium events are either disregarded altogether or addressed partly or entirely. Depending on the level of interpretation, the number of solved equations varies from three to seven. The majority of the models have been coded in 1D system codes [26] [27]. A growing number of studies employing multi-dimensional Computational Fluid Dynamics (CFD) have lately been presented [28] [29]. In comparison to the one-dimensional compressible solvers, the

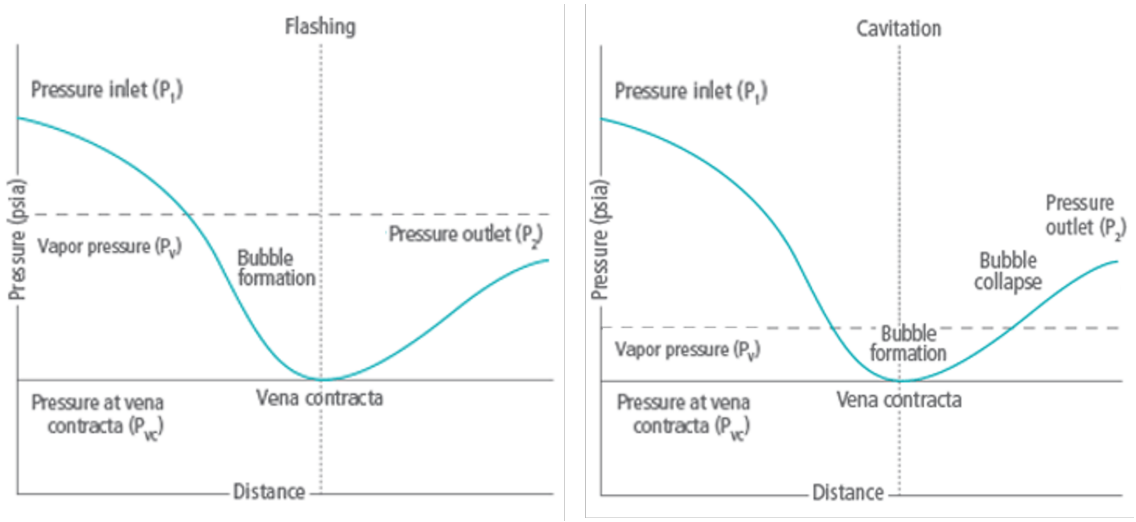

Figure 2.3: The difference between flashing and cavitation. The image shows pressure curves along a restriction like a valve. The left image shows the flashing process and the right image the cavitation process. Image taken from ISA [23].

multi-dimensional distribution of the phases may be obtained in great detail using CFD technology. A separate section discusses the state-of-the-art multi-dimensional simulating of flashing flows.

2.3 Isenthalpic Modelling

The objective of this section is to illustrate a simple method for solving a compressible flow through in a one-dimensional cross-sectional area. When no discontinuities are present, a steady isentropic flow can be easily solved by means of the energy and mass equation. When these assumptions are accounted for, the energy equation can reduce to an enthalpy equation in which the total enthalpy is taken constantly throughout the nozzle. This can be seen in the following equation:

$$h_{\mathrm{t}} = h + \frac{1}{2}u^2, \tag{2.2}$$

$$h_{\mathrm{t}} = e + pv + \frac{1}{2}u^2 \tag{2.3}$$

with h_{t} and h the total and the static enthalpies, respectively, and u the velocity.

In the absence of any sources, mass flow is continuous all the way across the nozzle (this is just a simplified version of the continuity equation):

$$\rho u A = G \tag{2.4}$$

with G the mass flow in kg/s and A the cross-sectional area in m^2/s.

With $M = u/c$, the velocity in the energy equation can be formulated Mach-based. This slight modification of Equation 2.2 results in the following formulation:

$$h_t = h + \frac{(Mc)^2}{2}. \tag{2.5}$$

Since Mach equals unity in the throat of the nozzle, the mass flow can be determined by multiplying the speed of sound, the area at the throat and the density. Basically making use of Equation 2.4 where the velocity is replaced by the speed of sound. Subsequently, this mass flow can be used to determine the remaining flow variables together with the area distribution in the nozzle, which results in:

$$h_t = h + \frac{1}{2}\left(\frac{G}{\rho A}\right)^2. \tag{2.6}$$

Equation 2.6 is solved by achieving the right temperature for the enthalpy and the density. Entropy is constant and is determined only by the flow total conditions (s = s(T_t, p_t)), which are defined as modes in which the flow velocity is zero (in the initial conditions). This is also the case for the total enthalpy: h_t = h(T_t, p_t).

With the current hypothesis of assumptions, the momentum equation can be reduced to the following:

$$\frac{dp}{\rho} + udu = 0 \tag{2.7}$$

where du and dp are the changes in velocity and pressure, respectively. This equation, together with the continuity equation, can produce a famous result for isentropic expansion:

$$(M^2 - 1)\frac{du}{u} = \frac{dA}{A}. \tag{2.8}$$

The flow behaviour of any convergent-divergent (CD) nozzles - also called De Laval nozzles - can be described by means of this equation. It explains whether the flow is subsonic ($M < 1$) or supersonic ($M > 1$). For the latter, the flow will counter-intuitively accelerate in the divergent section. Also, the transition from subsonic to supersonic (where $M = 1$) implies the existence of a throat. In Equation 2.8 this is the the point where dA/A equals zero. The outlet, however, can show multiple different behaviours.

Firstly, the flow will not reach any sonic conditions if the outlet pressure is too high. For this scenario, the flow behaves just like any incompressible flow. Secondly, if the outlet pressure is low enough, sonic conditions have reached the throat and expanded along the divergent section and operate fully supersonically. These two scenarios can be fully resolved by an isenthalpic solver since the isentropic expansion

law holds. In between these two cases, however, a shock wave will occur. At this point, the isentropic expansion law fails and a shock capturing scheme, as will be described in Section 2.7 is necessary.

2.4 Mass transfer

It is clear now, that the CO_2 is expected to cavitate or flash during the flow through a valve. For the purpose of thoroughness, this section seeks to give insight into this physical phenomenon modelled.

2.4.1 Theory

A $p - v$ diagram, as in Figure 2.4, is often used to show the phase transition in a boiling process. At constant pressure, this mechanism happens in the two-phase region under thermal-equilibrium [30]. In actuality, the phase transition within nozzles is highly connected to nonequilibrium phenomena; hence, this figure cannot be utilised to forecast fluid dynamics during phase change [31].

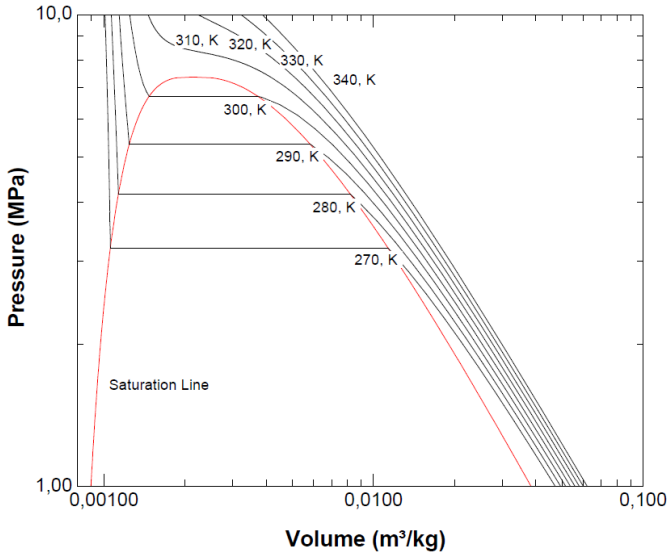

Figure 2.4: The $p - v$ diagram of CO_2 with the two-phase region beneath the two saturation lines depicted as red lines. Image created in REFPROP [16].

When a subcooled CO_2 flow comes in the nozzle, the abrupt depressurisation causes superheated CO_2 and, as a result, phase change. The bubble nucleation process is linked to nonequilibrium factors in this scenario [32]. In general, the phase change process caused by a sudden pressure decrease is divided into three stages, as seen in Figure 2.5 and summarised below:

Firstly, as the pressure falls below saturation, tiny nuclei in non-wettable rough wall cavities and in the bulk flow begin to increase. The surface tension forces, which restrict the expansion of the nuclei, dominate the behaviour of the dispersed phase (i.e. the bubbles) at this stage (often called a delay period [33]). This lag, which accounts for thermal non-equilibrium, affects global fluid dynamic parameters (i.e., the total mass flow and the vapour holdup at the exit). Since surface tension forces are relatively small for vapour-liquid CO_2, it is expected this delay period is a relatively short period of time.

At the moment the bubble surpasses a threshold radius, the second stage begins [32]. The pressure differential between the bubble (i.e. the dispersed phase) and the neighbouring liquid (i.e. the continuous phase) dominates bubble growth at this stage. The Rayleigh-Plesset equation can be used to approximate the bubble development rate at this point [34].

Heat transfer around the bubble interface dominates the third step [31]. Turbulence variations and relative motion between bubbles and the neighbouring liquid have a substantial impact on the heat transfer mechanism at the liquid-vapour interface at this stage [35].

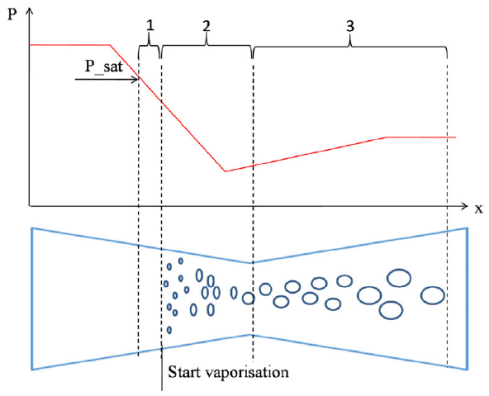

Figure 2.5: Schematic of the physical behaviour of a flashing flow with the start op vaporisation. Image is taken from Dang Le et al. [31].

Modelling interphase mass transfer in CFD codes is thus quite complex and creates a challenge in terms of numerical implementation. Basically, there are two schools of thought: Eulerian-Eulerian and Eulerian-Lagrangian. The former represents the approach in which both phases are expressed in Eulerian terms, and thus are properties represented by the flow field. Contrarily, for the Eulerian-Lagrangian approach, one phase is represented by single particles. These particles can all have their own properties and are not bound by the surrounding flow. For evaporating flows, this particle phase is often represented by the vapour phase, as it is the nucleating phase. This is reversed for condensing flows.

For steam condensation, Eulerian-Lagrangian models available in commercial CFD codes have been developed and extensively validated; they refer to the classical

nonequilibrium condensation theory for steam turbines that dates back to the 1960s and is based on the free energy analysis of a two-phase system for a single, pure substance [36]. In practice, this phenomenon must be combined with the so-called heterogeneous condensation, which is caused by wall contact, contaminants, and other factors, and also plays an essential role. Most solutions combine these two condensation models, which represent the nucleation rate (how many particles form in a given volume). A third set of equations, describing particle development and interaction with the surrounding flow, must also be solved.

There are numerous publications on the applications of these models for steam-expanding flows. For CO_2, however, these references are less common. These models' overall accuracy and precision would make them the best choice for the phenomena at hand. They were designed, however, for a different material (H_2O) and different thermodynamic conditions - pressure in the final stages of a steam turbine is one order of magnitude lower than the pressure in critical or near-critical carbon dioxide [31]. This suggests that adapting them to the current instance will need extensive fine adjustment of semi-experimental parameters as well as the use of alternative sub-models. Some of these may not even be immediately accessible to the user in commercial CFD codes.

As a result, they will not be studied in depth; instead, the major focus of this study will be on Eulerian-Eulerian two-phase models. Also, with high volume fractions of the secondary dispersed phase, the accuracy of Eulerian-Lagrangian approach decreases significantly. Moreover, the Eulerian-Eulerian approach can be beneficial if the goal of the research is to evaluate mass transfer and its effect (in terms of volume or mass fractions) on total flow quantities (pressure, temperature).

These models may be classified based on how many flow fields (velocity, pressure, and temperature) are shared between the phases. This significantly simplifies the numerical solution since equations may be summed up and solved for the mixture rather than for individual phases, resulting in superior convergence qualities. In particular, if the velocity field is the same, the model is said to be homogeneous.

The delayed evaporation or nonequilibrium effects can be taken into account by considering metastable CO_2 properties. These metastable properties of subcooled vapour or superheated liquid can exist to a certain point: the spinodal limit. After this point, it is impossible for fluid to exist in a metastable phase and hence, phase change will occur. By considering these metastable states of the fluid during the phase change, it is possible to account for nonequilibrium effects. Lettieri et al. made use of this mechanism in simulating nonequilibrium condensation of supercritical CO_2 in a de Laval nozzle [37].

2.4.2 Cavitation models

For a single-fluid approach, there are several models available to describe cavitation. These are all 'one-equation models', which means that only one additional equation

is needed: the vapour transport equation,

$$\frac{\partial \alpha_{\mathrm{v}} \rho_{\mathrm{v}}}{\partial t} + \nabla \cdot (\alpha_{\mathrm{v}} \rho_{\mathrm{v}} u) = R_{\mathrm{e}} - R_{\mathrm{c}} \tag{2.9}$$

where: R_e, R_c are source terms in [kgm^{-3}s^{-1}]. These source terms are often determined empirically, but can be analytically described too by means of the Rayleigh-Plesset equation [38]

$$R_{\mathrm{B}} \frac{d^2 R_{\mathrm{B}}}{dt^2} + \frac{3}{2}\left(\frac{dR_{\mathrm{B}}}{dt}\right)^2 = \left(\frac{p_{\mathrm{B}} - p}{\rho_{\mathrm{l}}}\right) - \frac{4\nu_{\mathrm{l}}}{R_{\mathrm{B}}}\frac{dR_{\mathrm{B}}}{dt} - \frac{2\gamma}{\rho_{\mathrm{l}} R_{\mathrm{B}}} \tag{2.10}$$

where: R_{B} is the bubble radius in meters, p_{B} the pressure of the bubble in Pascal, ν_{l} the kinematic viscosity in m^2/s and γ the surface tension in N/m. This equation describes all of the dynamics in the fluid of spherical bubbles. If the pressure differential is sufficiently large, Equation 2.10 can be considered as an adequate description for the inertia controlled bubble growth [39]. Doing so, the second order terms, viscous terms and the surface tension can be neglected and the equation reduces to the following:

$$\frac{dR_{\mathrm{B}}}{dt} = \sqrt{\frac{2}{3}\left(\frac{p_{\mathrm{B}} - p}{\rho_{\mathrm{l}}}\right)}. \tag{2.11}$$

Most of the possible cavitation models in CFD codes are based on this equation. They all have their evaporation and condensation source terms empirically determined by means of the Rayleigh-Plesset equation. In CFD codes, it is often possible to turn on the following cavitation models: Singhal et al. [40], Zwart-Gerber-Belamri (ZGB) [41], or Schnerr and Sauer [39].

The first is the most extensive model and also called 'the full cavitation model' [42]. It takes into account the effects of turbulence and includes the non-condensable gases. However, it is also the most unstable model. For example, it can only be activated via text commands in ANSYS Fluent and other models are recommended.

The second model, Zwart-Gerber-Belamri, assumes that all bubbles in the continuous fluid have the same size. Therefore, it treats cavitation using bubble number density n, described as the vapour volume fraction divided by the volume of a single bubble ($4/3\pi R_{\mathrm{B}}^3$). The final form of this cavitation model gives the following source terms:

$$R_{\mathrm{e}} = F_{\mathrm{vap}} \frac{3\alpha_{\mathrm{nuc}}(1 - \alpha_{\mathrm{v}})\rho_{\mathrm{v}}}{R_{\mathrm{B}}} \sqrt{\frac{2}{3}\frac{p_{\mathrm{v}} - p}{\rho_{\mathrm{l}}}} \tag{2.12}$$

$$R_{\mathrm{c}} = F_{\mathrm{cond}} \frac{3\alpha_{\mathrm{v}}\rho_{\mathrm{v}}}{R_{\mathrm{B}}} \sqrt{\frac{2}{3}\frac{p - p_{\mathrm{v}}}{\rho_{\mathrm{l}}}} \tag{2.13}$$

where R_B is the bubble radius (default 10^{-6}m), α_{nuc} the nucleation site volume fraction (default $5 \cdot 10^{-4}$m), F_{vap} the evaporation coefficient (default 50) and F_{cond} the condensation coefficient (default 0.01). Although they are constant, they can be changed in the software. According to the authors, these default values should apply to a wide range of fluids.

The last model, the Schnerr and Sauer model, follows the model of Singhal et al. to determine the expression for the net mass transfer. However, it uses another expression to combine the vapour volume fraction with the bubble number density:

$$\alpha_v = \frac{n_b \frac{4}{3}\pi R_B^3}{1 + n_b \frac{4}{3}\pi R_B^3}. \tag{2.14}$$

This led to the following formulas for the source terms:

$$R_e = \frac{\rho_v \rho_l}{\rho_m} \alpha_v (1 - \alpha_v) \frac{3}{R_B} \sqrt{\frac{2}{3} \frac{p_v - p}{\rho_l}}, \tag{2.15}$$

$$R_c = \frac{\rho_v \rho_l}{\rho_m} \alpha_v (1 - \alpha_v) \frac{3}{R_B} \sqrt{\frac{2}{3} \frac{p - p_v}{\rho_l}} \tag{2.16}$$

where the values of R_B and n_b can be set before the calculation.

2.5 Homogeneous Equilibrium Model

The HEM is the most often used two-phase model for CO_2 computations. The HEM is a two-phase model that is very simplistic. In the equations, just the variables of the mixture are calculated; there are no inter-phase source terms. Compared to two-fluid models, the numerical resilience and cheap computational cost of this model are its key advantages. As a result, the HEM is the primary focus of this research for one-dimensional calculations.

The HEM is described by a set of partial differential equations for the two-phase mixture that includes mass, momentum, and total energy conservation. In this notation, wall friction and energy dissipation are omitted.

$$\frac{\partial}{\partial t}\rho + \frac{\partial}{\partial x}(\rho u) = 0 \tag{2.17}$$

$$\frac{\partial}{\partial t}(\rho u) + \frac{\partial}{\partial x}(\rho u^2 + p) = 0 \tag{2.18}$$

$$\frac{\partial}{\partial t}(\rho e_t) + \frac{\partial}{\partial x}[(\rho e_t + p)u] = 0 \tag{2.19}$$

This system of equations is known as the conservative form, and its variables represent the following of the mixture: ρ the density, ρu the momentum and ρe_t the total energy. In these variables, u and e_t represent the velocity and the specific total energy, respectively. e_t can be further be broken down to: $e_\mathrm{t} = e + u^2/2$, where e is the specific internal energy.

This system of equations can be written in a compact 1D formulation with vector notation:

$$\frac{\partial}{\partial t}(\mathbf{U}) + \frac{\partial}{\partial x}\mathbf{F}(\mathbf{U}) = 0 \tag{2.20}$$

where the vectors $\mathbf{U}$ and $\mathbf{F}$ are:

$$\mathbf{U} = \begin{vmatrix} \rho \\ \rho u \\ \rho e_\mathrm{t} \end{vmatrix}, \mathbf{F} = \begin{vmatrix} \rho u \\ \rho u^2 + p \\ (\rho e_\mathrm{t} + p)u \end{vmatrix}. \tag{2.21}$$

The dynamics of a two-phase flow without external forces are governed by this non-linear hyperbolic conservative equation system [43]. Also, it is assumed to be inviscid and adiabatic. Its structure is mathematically identical to that of the single-phase Euler system. The HEM's assumption of complete thermodynamic and mechanical equilibrium results in the following constraints:

$$\begin{aligned} T_\mathrm{v} &= T_\mathrm{l} = T_\mathrm{sat}, \\ p_\mathrm{v} &= p_\mathrm{l} = p_\mathrm{sat}, \\ u_\mathrm{v} &= u_\mathrm{l} = u_\mathrm{m}, \\ g_\mathrm{v} &= g_\mathrm{l} = g_\mathrm{m}. \end{aligned}$$

In these expressions, l and v represent the liquid and vapour phases, respectively. The mixture property is denoted by the subscript m. The g term represents the Gibbs free energy, $g = h - Ts$. Here, s is the specific entropy, and h is the specific enthalpy. Temperature, pressure and velocity are the remaining variables, denoted with T, p and u, respectively.

Since the density and specific internal energy are the independent variables, these are described with a mixture property using the thermodynamic quality, x:

$$\begin{aligned} e &= xe_\mathrm{v} + (1-x)e_\mathrm{l}, \\ v &= xv_\mathrm{v} + (1-x)v_\mathrm{l}, \\ v &= 1/\rho. \end{aligned} \tag{2.22}$$

Here, the subscripts again represent the vapour and liquid phases at saturation.

The quality is calculated using the specific enthalpy, $h = e + pv$, together with the saturated values of the enthalpy, which results in the following formulation:

$$x = \frac{h - h_\mathrm{l}}{h_\mathrm{v} - h_\mathrm{l}}. \tag{2.23}$$

The saturated values of the specific enthalpy can be calculated using pressure. Another thermodynamic property that is relevant for multiphase modelling is the speed of sound. It can be described with the following relation:

$$c^2 = \left(\frac{\partial p}{\partial \rho}\right)_s \tag{2.24}$$

where it is defined by the change in pressure divided by the change in density at constant entropy (s). This value is needed for the wave propagating speed of the model, which in turn is a relevant characteristic of the equation system. However, as will be discussed in Section 2.8.4, this velocity depends on the composition of the mixture or on the level of equilibrium between the phases. As known from the literature, the HEM has a discontinuous speed of sound at the line of saturation [20]. It is calculated using the void fraction, which can be calculated using the quality together with the saturated densities:

$$(\alpha)^{-1} = 1 + \frac{1 - x}{x}\frac{\rho_\mathrm{v}}{\rho_\mathrm{l}}. \tag{2.25}$$

Here, the void fraction is specified by the part of a total volume that is filled by the vapour phase and is represented by α in equation 2.25.

The system of equations (Equation: 2.17 - 2.19) is however under-defined. Since there are fewer equations (3) than there are unknowns (4), an Equation of State (EoS) is necessary to close this system. It enables the calculation of the pressure from the two independent variables: density and specific internal energy.

2.6 Equation of State

To compute the pressure and close the system, an equation of state (EoS) is required to solve the conservative equations. However, this is not always that simple. For one-dimensional modelling and future CFD simulations, a function is needed to calculate fluid properties in liquid, vapour, supercritical, and two-phase states at an acceptable computational cost. As a result, an accurate and efficient method for computing thermodynamic properties is required. To compute thermodynamic properties, there are a few approaches when performing dynamic simulations [44]: (1) select an EoS and use an iterative algorithm to get the correct properties, (2) make a direct call to a program like REFPROP [45] that automatically executes

the most accurate EoS for each calculation or (3) making use of tabular data where specific properties will be interpolated in between.

Different EoS can be used for dynamic simulations. A reasonably simple EoS, like the stiffened gas (SG) or the Peng-Robinson (PR), is often chosen. However, these EoS lack accuracy and there are preferred alternatives with higher accuracy for pure CO_2. From the triple-point temperature to 1100 K at pressures up to 800 MPa, the Span-Wagner (SW) [46] EoS is regarded as the standard EoS for CO_2. The SW EoS is derived from the Helmholtz free energy A and is based on many variables that are empirically defined. However, the density and the specific internal energy are the two independent variables for a compressible solver which is based on Equations (2.17 - 2.19). As a result, a method has been built to calculate the thermodynamic properties with the SW EoS using a density-energy state function [47].

The other two methods, tabulated data and direct calls to programs like REFPROP, are primarily used. It is often computationally less costly, and REFPROP also uses the SW EoS. The tabulated data are made in advance and can be stored. Different interpolation methods are used to calculate properties that lie between the limits of this table. When performing extensive calculations, tabulated data is often created to reduce CPU time. On the other hand, the direct call to REFPROP is generally considered for less extensive simulations.

2.7 Shock Capturing Scheme

Solutions to the problem described in Equation 2.20 are called weak solutions and discontinuous solutions are allowed. Therefore, this problem should be approached in a way that smooth solutions can be obtained. The system can be rewritten in quasi-linear form [48],

$$\frac{\partial}{\partial t}(\mathbf{U}) + \mathbf{A}(\mathbf{U})\frac{\partial}{\partial x}\mathbf{U} = 0 \tag{2.26}$$

where $\mathbf{A}(\mathbf{U}) = \frac{\partial \mathbf{F}}{\partial \mathbf{U}}$ and represents the Jacobian matrix of the system. So, $\mathbf{A}(\mathbf{U})\frac{\partial \mathbf{U}}{\partial x} = \frac{\partial \mathbf{F}}{\partial \mathbf{U}}\frac{\partial \mathbf{U}}{\partial x} = \frac{\partial \mathbf{F}(\mathbf{U})}{\partial x}$, where the chain rule $\mathbf{F} = \mathbf{F}(\mathbf{U})$ has been used. The full derivation of this matrix can be found in the study by Log et al. [48]. Here, it was shown that the eigenvalues of this matrix are:

$$\lambda_1 = u - c, \lambda_2 = u, \lambda_3 = u + c.$$

Hence, the 1D Euler equations described in Section 2.5 constitute to a hyperbolic system.

These eigenvalues can be interpreted as characteristic lines which describe three different waves propagating at the speed that is defined by that eigenvalue. These

can be seen in Figure 2.6. Because some thermodynamic properties on these waves remain constant, data about the state where the waves come from is carried along. Throughout these waves, some quantities remain constant. Riemann invariants are the names given to these quantities [48]:

$$\begin{aligned} \text{constant } s, u + \frac{2c}{\Gamma} \text{ across } \lambda_1 = u - c \\ \text{constant } u, p \text{ across } \lambda_2 = u \\ \text{constant } s, u - \frac{2c}{\Gamma} \text{ across } \lambda_3 = u + c \end{aligned} \tag{2.27}$$

where s is the entropy, u the velocity, p the pressure and Γ the first Grüneisen parameter. This last property is defined by:

$$\Gamma = \frac{1}{\rho c_v} \left(\frac{\partial p}{\partial T} \right)_\rho \tag{2.28}$$

where c_v is the specific heat capacity at constant volume. The Riemann problem, on the other hand, is stated as an initial value problem:

$$\begin{aligned} \tfrac{\partial}{\partial t}(\mathbf{U}) + \tfrac{\partial}{\partial x}\mathbf{F}(\mathbf{U}) = 0 \\ \mathbf{U}(x,0) = \begin{cases} \mathbf{U}_\mathrm{L}, \text{ if } x < 0 \\ \mathbf{U}_\mathrm{R}, \text{ if } x \geq 0 \end{cases} \end{aligned} \tag{2.29}$$

where two different states are represented by $\mathbf{U}_\mathrm{L}$ and $\mathbf{U}_\mathrm{R}$. The waves that are possible for the solution of the Riemann problem are therefore only rarefactions and shocks associated with λ_1, λ_3 and a contact discontinuity associated with λ_2. The characteristics are parallel near a contact discontinuity. p and u remain constant over a contact discontinuity, whereas ρ and e (and hence s) are discontinuous. On each side of a shock, the characteristics converge. All of the variables (u, e, and p) are discontinuous across shocks. It is also feasible that the one or both waves corresponding to λ_1 or λ_3 are a rarefaction. The variables ρ, u, e, and p vary smoothly in rarefaction waves. The entropy remains constant along smooth flow lines. A rarefaction wave will flow inside a pipe during depressurisation, whereas a shock and a contact discontinuity will escape the pipe. The entropy conservation over the rarefaction may then be utilised to provide a boundary condition for the flow outlet [49]. An example of the characteristics of such waves can be found in Figure 2.6.

The different waves described here can be combined to connect the left and right states stated in Equation 2.29. It is feasible to get accurate numerical solutions

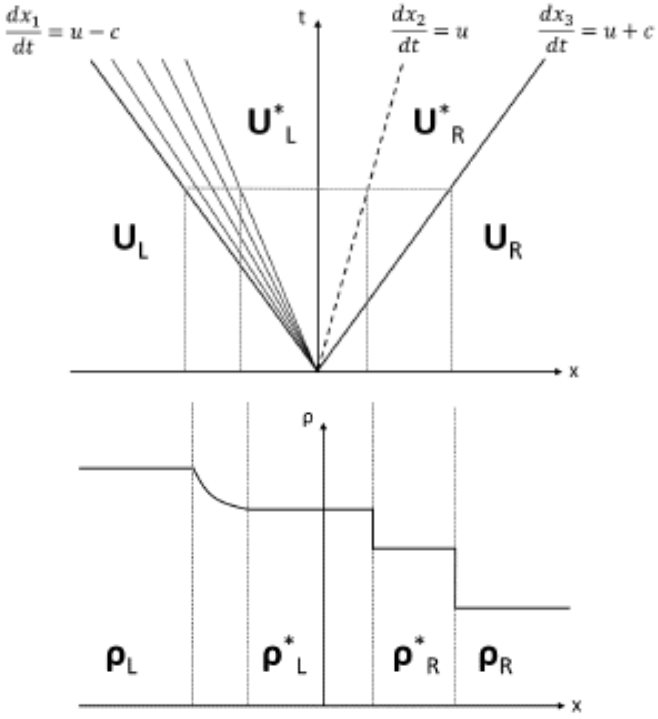

Figure 2.6: The characteristics for a Riemann problem where the density and the pressure of the left state are larger than the right state. This results in a rarefaction to the left, a contact discontinuity, and a shock to the right. Image is taken from Log et al. [48].

for the Riemann issue using knowledge about the characteristics and Riemann invariants. For complicated equations of state, however, obtaining the exact solution can be computationally very costly. Approximate Riemann solvers are employed for this reason. The approximate Riemann solver AUSM is one example and stands for Advection Upstream Splitting Method. This method is based on a flux-splitting method. This method splits the flux into two components and considers the net effect on the flux from characteristic waves pointing to the face from both sides. It is a technique first used by Liou et al. [50] in 1993 but is still used today as a method for a compressible flow solver. For example, Brown et al. [51] used this method to simulate two-phase flow through ducts with discontinuous cross-sections.

2.8 State of the Art

The one-dimensional (1D) modelling of CO_2 is a standard approach to examining the thermophysical properties of a fluid along a path. However, complex multi-dimensional processes, such as vorticity, shock wave interaction with boundary layers, and turbulent mixing, cannot be explored because of the simplicity of 1D mod-

els. To examine these, multi-dimensional CFD simulations must be applied. The accuracy of the 1D model also depends on the underlying assumptions and simplifications.

A few 1D models are available that describe the flow of CO_2 through valves [52][53]. However, there are other applications in which phase changes occur. Many studies have been performed on CO_2 ejector models for refrigeration applications with nozzle simulations [26][54][55]. Also, converging-diverging models have been widely examined [2][1]. A CO_2 flow is modelled with the variable area, phase change, and depressurisation in both of these processes. These studies will also be included in this literature overview.

2.8.1 Ejector & Nozzle

To discretize the flow behaviour of the supercritical CO_2 for an ejector, Banasiak and Hafner [26] created a one-dimensional model. In the mixing duct and diffuser, a mixture model was utilized to account for the mixing of the two streams. Multiple effects were taken into account with this one-dimensional model, such as the metastability effects and the shock waves. Also, the mixing and the geometry of the ejector were integrated. A schematic description of this concept can be seen in Figure 2.7. These metastability effects take into account that for example, liquid CO_2 can exist in a state where vapour is favoured, which is the state of minimal value of the Gibbs free energy. A well-known example is that of very pure water. It can remain in the liquid phase even down to -42 °C when cooled very slowly. However, it is not thermodynamically stable and any perturbation can cause its crystallisation [56].

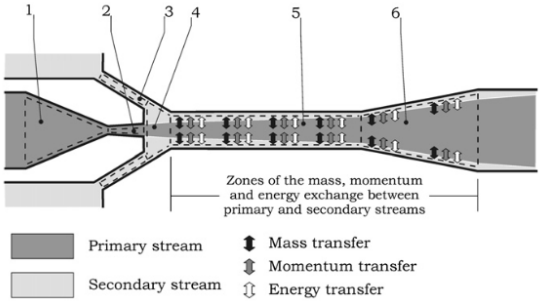

Figure 2.7: Schematic description of a two-phase ejector. Numbers 1 and 2 represent the converging-diverging section of the nozzle. Numbers 4 and 5 illustrate the mixing chambers, and 6 the diffuser. Image is taken from Banasiak and Hafner [26].

For CO_2 nozzle simulations, Angielczyk et al. [27] suggested a 1D Homogeneous Relaxation Model (HRM). The numerical findings were compared to the measurements of Nakagawa et al.[2]. A 1D gas dynamic model was also utilised by Berana et al. [57] and Raman and Kim [58] to model shock waves inside the nozzle. A

typical shock wave was produced, which was substantially thinner and more robust than that recorded in the experiments.

2.8.2 Restrictions

Modelling of multiphase critical flow via an orifice is required to simulate transient phenomena such as depressurisation or fracture development in CO_2 pipes. Critical flow occurs at the sonic point for homogeneous flows, where the fluid velocity equals the speed of sound. Phase transfer must be considered when integrating the conservation equations for multiphase flow. There are two alternative assumptions in use here, each of which represents a limiting case:

- **Homogeneous Equilibrium Model**: The choked flow is considered in thermal equilibrium. The phase fractions change instantaneously through the choke with changing pressure and enthalpy.
- **Frozen model**: Throughout the choke, the phase composition is expected to stay constant. The mass fractions remain constant but the chemical potential differs between the phases.

There are several empirical correlations in frequent usage, in addition to the two extreme situations discussed above. The Henry–Fauske model [59], which may be considered as an adjustment of the frozen model, is widely known. In general, altering phase equilibrium assumptions will yield different results: a different pressure drop for when the flow becomes choked and, as a result, a different mass-flow rate. [18]. Figure 2.8 depicts a comparison of the three models described. When compared to a non-equilibrium model, a HEM will result in choked flow at a smaller pressure drop over the valve. The variation in estimated mass flow will be significant in many circumstances. As a result, the acceptance of phase equilibrium in valves and fractures can significantly impact time-dependent multiphase pipeline models. According to Aursund et al. [18], the theory of homogeneous flow through a valve might be wrong in multiphase flow. Although it depends on the flow regime, there may be a large difference in acceleration between the two phases.

The flow through valves or constraints is usually included as a boundary condition in the modelling for the depressurisation of pipelines or valves. Choked flow is expected in the early phases of depressurisation, where the actual two-phase speed of sound limits the flow velocity. A very popular method to model choked flow is to use a HEM and assume steady-state flow. Associating the expanding fluid's velocity equally with the speed of sound yields the choking condition.

2.8.3 Decompression Behaviour

The velocity of the rarefaction wave travelling through a pipeline was shown to be equal to decompression wave speed in Section 2.7. This has been also widely ex-

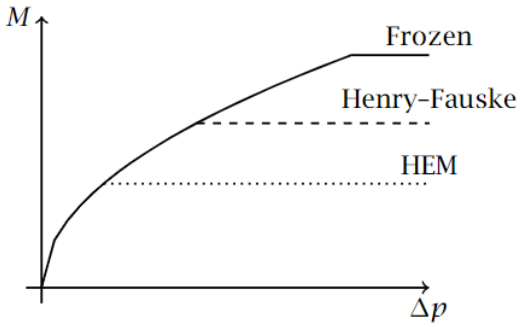

Figure 2.8: Mass flow of CO_2 for multiple models with respect to a pressure differential across a restriction. Image is taken from Aursand et al. [18]

amined in the literature. Mahgerefteh et al. [60] looked at the difference between the experimental and calculated decompression-wave speed for carbon dioxide in a gaseous state. Moreover, they studied this effect in mixtures of carbon dioxide. Contaminants decreased the phase-transition pressure plateau in the situations studied. As can be read below, this is the opposite during depressurisations from a liquid or supercritical state.

The decompression wave speeds of pure and CO_2-rich combinations were investigated by Cosham et al. for the liquid and supercritical phase [61]. From several experiments, decompression curves were displayed. In two of these experiments, they further investigated in which they compared pressure values with their time of recording. The research was prompted due to the reason that predicting the steel toughness was necessary to stop a running-ductile fracture. This, according to the authors, required awareness of the decompression behaviour [62]. Compared with gas-phase CO_2, the authors determined that dense-phase CO_2 follows a distinct trend: the measured pressure plateaus in the decompression trials were constantly inferior to those anticipated by deployed EoS. Furthermore, throughout the pipe, the recorded pressure plateau grew. Cosham et al. speculated that a possible reason for this might have something to do with the 'delayed nucleation,' or thermodynamic non-equilibrium. They urged that additional research should be done to understand the phenomenon fully.

Jie et al. [63] numerically modelled the HEM using the PR EoS. They compared the data from Cosham et al [61] and the plateau pressures were found to be overestimated, particularly for depressurisations that began in the gas phase. According to Jie et al., this might be because of non-equilibrium factors not being recorded by the HEM. This is something that is seen now more often while employing the HEM.

Brown et al. [64] provided pressure calculations with respect to time from two depressurisation tests for pure CO_2 for the affirmation of the relaxation model (HRM). In contrast to the HEM, the phase shift in the HRM is not immediate. Instead, a 'relaxation time' is used. As a result, the expected pressure was somewhat lower.

According to the published pressure charts, the relaxation vs full-equilibrium modelling did not turn out to be the major source of error in the experimental data.

In further research from many of the same authors, Brown et al. [65] also provided both pressure measurements taken at various sites throughout the depressurization of a pipe from the first portion to the process. Moreover, temperature traces were recorded too. They used both a HEM as well as a TFM to investigate this, with the interphase mass transfer being modelled using the relaxation of the calculated enthalpy. In general, the TFM outperformed the HEM, with an increasing difference while getting a greater distance from the outflow. The authors discovered that a rather short relaxation time of $5{\cdot}10^{-6}$ s during the first 1 s of depressurization achieved an adequate understanding of calculation and measurements. After one second, a prolonged relaxation time of $5{\cdot}10^{-4}$ s resulted in improved agreement [62]. It remains a mystery, however, to find an exact explanation for the flow to achieve equilibrium faster in the early phases of the depressurisations.

Munkejord and Hammer [66] expanded the modelling work on TFM. In general, the TFM could not be stated to produce superior outcomes to the HEM, despite its additional complexity. More extensive modelling and experimental research, according to these scientists, might enhance the modelling using a TFM.

2.8.4 Wave Propagation

The propagation of pressure waves is a crucial feature in a number of phenomena of practical significance. The flow will frequently be choked at the exit during a pipeline depressurisation. This implies, as mentioned before, that the velocity of the fluid at that place is of the same magnitude as the local pressure-propagation velocity, which is equal to the speed of sound [62]. This is a thermodynamic characteristic property for a fluid and can be described by the following relation for phase k:

$$c_{\mathrm{k}}^2 = \left(\frac{\partial p_{\mathrm{k}}}{\partial \rho_{\mathrm{k}}}\right)_{s_{\mathrm{k}}} \tag{2.30}$$

The situation is more difficult in a two-phase flow. Munkejord et al. owe this to the fact that "the observable pressure-propagation speed is a function of the flow topology" [62]. The HEM is the most basic model, with the pressure-propagation speed being only influenced by the gas volume fraction. Hence, this pressure-propagation speed is just the speed of sound of the total mixture. The speed of sound for pure gas and liquid is usually higher.

According to the pipe depressurisation data of Cosham et al. [61], the flow appears to be non-equilibrium, particularly during the early moments of depressurization and near the exit. However, models that appropriately account for this phenomenon while using the HEM, have yet to be developed and validated. Usually, this means that flow models account for non-equilibrium in at least one of the following: thermal (temperature), chemical (chemical potential) and mechanical

(pressure), in addition, to slip between phases. As a result, the HEM is not always assumed to be the best fit for pipe-depressurisation cases, despite its excellent performance in many circumstances. As is clear now and discussed before, this is due to the fact that the speed of sound does not show continuous behaviour at the phase line and approaches zero near the triple point in the HEM [62]. This trait is not thought to be physical, and thus complicates the development of numerical techniques and simulations.

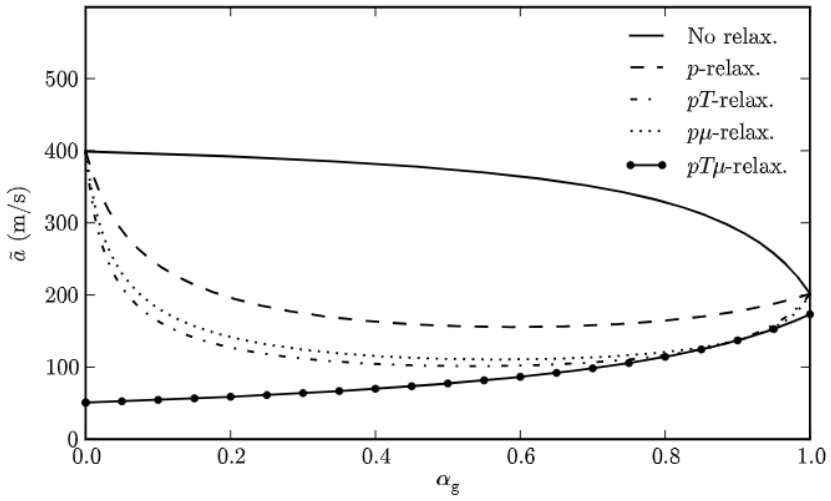

Figure 2.9: The speed of sound with respect to the void fraction for equilibrium conditions for CO_2 at 50 bar. Image is taken from Flätten and Lund [20].

Figure 2.9 shows the speed of sound ($\tilde{a}$) for the various models with respect to the holdup fractions (α). The velocities of the middle three models are virtually close to each other. However, the full equilibrium velocity, denoted with the black dots, is significantly lower. These low velocities predicted by the homogeneous equilibrium model are unphysical. This relation indicates that for numerical simulations of CO_2 pipeline transport, the single or double relaxed models are the best to use. The full equilibrium model would be unphysical since it would generate slow propagation of pressure waves. Also, the discontinuities are noticeable when examining the limits of functions of the wave propagation speeds. It is expected that the two-phase speed of sound would be reduced to the single-phase speed of sound in the limit of only one volume fraction [67]. This is the case for all relaxation models, except for the full equilibrium:

$$\lim_{\alpha_k \to 1} \tilde{a}_p = \lim_{\alpha_l \to 1} \tilde{a}_0 = c_k \tag{2.31}$$

$$\lim_{\alpha_k \to 1} \tilde{a}_{pT\mu} \neq c_k \tag{2.32}$$

where the wave propagation speeds are denoted by :

$$\tilde{a}_0 = \frac{m_{\mathrm{g}} c_{\mathrm{g}}^2 + m_{\mathrm{l}} c_{\mathrm{l}}^2}{\rho} \tag{2.33}$$

$$\tilde{a}_p^{-2} = \rho \left(\frac{\alpha_{\mathrm{g}}}{c_{\mathrm{g}}^2 \rho_{\mathrm{g}}} + \frac{\alpha_{\mathrm{l}}}{c_{\mathrm{l}}^2 \rho_{\mathrm{l}}} \right) \tag{2.34}$$

$$\tilde{a}_{pT\mu}^{-2} = \tilde{a}_p^{-2} + \rho T \left[\frac{\alpha_{\mathrm{g}} \rho_{\mathrm{g}}}{c_{p,\mathrm{g}}} \left(\frac{\partial s_{\mathrm{g}}}{\partial p} \right)_{\mathrm{sat}}^2 + \frac{\alpha_{\mathrm{l}} \rho_{\mathrm{l}}}{c_{p,\mathrm{l}}} \left(\frac{\partial s_{\mathrm{l}}}{\partial p} \right)_{\mathrm{sat}}^2 \right] \tag{2.35}$$

where the subscripts $0, p, pT\mu$ represent the basic mixture, pressure relaxation and full equilibrium model, respectively.

Relaxation models are frequently used in flow models that allow for some degree of non-equilibrium (see Aursand et al. [18]). Munkejord [68] [69] used a two-fluid model to study pressure relaxation. This model approximated a mixture model with spontaneous relaxation where only pressure is determined. However, the numerical relaxation process created a large amount of numerical diffusion.

Flätten and Lund [20] used a multi-component flow model with thermal relaxation to generate formulas for wave velocities. For the two-phase example, Martnez Ferrer et al. [70] looked at relaxation models too. In their model, they had a temperature and velocity relaxation. For no-slip two-phase flow models, Lund [67] created a relaxation-model hierarchy with a joint determination for the two-phase speed of sound. The full equilibrium model was proven always to have a lower sound speed than the other relaxation models. That is to say, the HEM has the minimum two-phase mixing speed of sound. Linga [71] enlarged the relaxation-model hierarchy, enabling slip between phases.

So far, nearly all relaxation models have considered that phase transfer is either 'quick' or regulated by a set relaxation period. Physical modelling of phase transfer, accounting for key dynamics, should be included in future models. In a study by Lund and Aursand, they initiated a different method accounting for evaporation and condensation mass transfer [72]. This approach was based on statistical rate theory and according to the authors could provide a framework. They acknowledge that it is yet to be validated using experimental data.

Benintendi [73] examined non-equilibrium effects. He focused mainly on phase transitions of liquid and supercritical CO_2 expansions after the stagnation point. The author outlined the shortcomings of the HEM and proposed that adopting a relaxation model (HRM) might enhance the modelling of the CO_2 characteristics after the restriction. To justify the non-equilibrium behaviour, he identifies the relaxation time and the liquid phase metastability as the intrinsic properties of CO_2 for that. The HEM was used to do a simplified steady-state numerical computation along an expansion route. However, it was not immediately relevant to non-equilibrium

phase transitions. To get a proper estimate of pressure and temperature for quick depressurisations, it seems that considering the delayed homogeneous nucleation is required. Additionally, non-equilibrium thermodynamics must be used to overcome the triple-point singularity caused by the complete equilibrium presumption [62].

2.8.5 Multi-dimensional Modelling

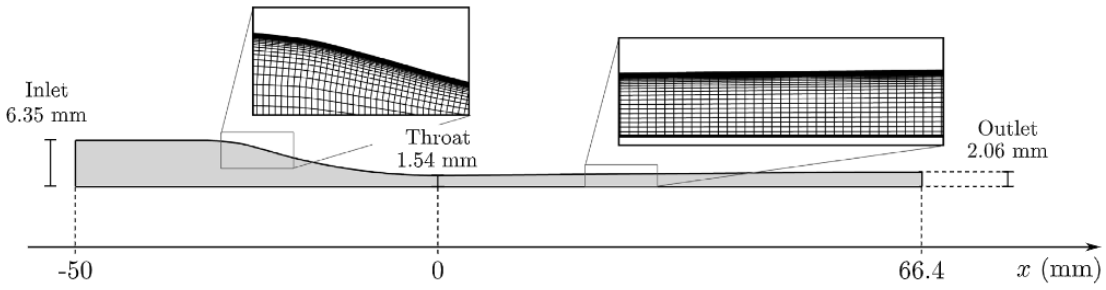

Figure 2.10: An example of a multi-dimensional numerical assessment of a flashing flow. Image taken Romei and Persico [74].

The literature discussed for one-dimensional modelling is of course also relevant for multi-dimensional modelling. However, there are some issues in which multi-dimensional CFD modelling differs from one-dimensional modelling, as already mentioned at the beginning of this chapter. Precisely for those issues, it is still interesting to investigate how this has been handled so far.

Yazdani et al. [28] simulated a supersonic two-phase flow in a converging-diverging nozzle. The authors used Fluent in which they compiled a mass transfer UDF to replicate the Singhal et al. [40] cavitation model. In a 2D geometry, they simulated high-pressure CO_2 flow and were able to properly replicate experimental data. They found that the two-phase flow choked at a later stage in the nozzle, as opposed to the location of the throat.

Another application of CFD simulations in the field of flashing flows is performed by Giacomelli et al. [29]. The authors created an extensive model to incorporate the right PVT data into the software using a multi-species UDRGM. With the help of this model, they investigated different formulations of the speed of sound. They concluded that the formulation by Brennen [75] might give improved results as opposed to the default formulation by the software.

In the study by Liu et al., [76] the decompression behaviour of high-pressure CO_2 pipelines is studied. To account for the inter-phase mass transfer, they introduced an extra mass transfer coefficient in the mass source term. For the energy balance, they did something similar: an energy source term was included to account for latent heat owing to vaporisation. It was validated with the modelling performed by Botros et al. [77], and the impacts of delayed nucleation on CO_2 decompression characteristics

were explored using the suggested model [76]. This allowed the modelling of delayed nucleation during depressurisation. The authors found good agreement with the measurements once they fine-tuned the mass-transfer coefficients.

In a paper by Romei and Persico [74], two computational strategies are examined to simulate the two-phase flow of CO_2 in supercritical conditions. Both strategies make use of the mixture model in the program ANSYS Fluent. Because of the more simple thermodynamic treatment, these simplifications result in a decrease in total computing cost as well as enhanced solver robustness. The authors compared the results with experiments for cavitating and condensing flow and found, despite the use of the oversimplified model, remarkably good results. However, the largest deviations were found in expansions from sub-critical states, probably due to metastable effects.

Li and Deng [78] also investigated flashing CO_2 flow for the use of an ejector. They compared it with experimental data, and the findings revealed that the created CFD model was remarkably precise in forecasting mass flow rates and flow fields. Also, the proposed non-equilibrium CFD model was compared to a HEM. In contrast to Romei and Persico [74], large deviations were found between the two models. With a 34.55 per cent inaccuracy, the HEM projected a lower mass flow rate of primary flow than the non-equilibrium model [78].

The decompression wave speed was examined by Elshahomi et al. [79] with a CFD model developed using ANSYS Fluent. Two separate 'shock tube' experiments were used to confirm the projected outcomes. The results were mostly in line with the known experimental data. The simulation was able to track the pressure drop, which accounted for the phase change. Also, they investigated the effects of changing the initial operating temperature. According to the simulations done by the authors, increasing this variable resulted in a lower decompression wave speed.

Xiao et al. [80] studied the non-equilibrium phase transition during decompression. They implemented the SW EoS and used the mixture model for the multiphase flow. According to the authors, the evaporation coefficient had a significant impact on the results. By varying this parameter, they were able to get a good agreement with the test results. Also, the flow velocity was examined, whereas it had an effect on the phase transition: a smaller flow velocity resulted in a faster temperature drop, which as a consequence, accelerated the phase transition.

Chapter 3

Methodology

As already mentioned in Chapter 2, no experimental data on high-pressure CO_2 flow through valves is available yet. Also, numerical research on this specific topic is scarce. Therefore, other applications in which the same events occur, such as phase change, depressurisation and the possibility of shock waves, were considered. Shock waves for high-pressure CO_2 flow in a converging-diverging nozzle were studied by Nakagawa et al. [1]. Also, another article by the same author where no shock wave but supersonic outflow is observed is a commonly referred reference case [2]. The author does both experimental and numerical work in both papers. These papers will be used as reference cases in this study.

In this chapter, the three different models will be explained and compared. The numerical codes of the first two regarding the Quasi 1D models, originate from Prof.Dr.ir. R. Pecnik. They have been modified to solve the flow with the relevant specifications and extended to account for multiphase flow. The last model, which has been implemented in Fluent, is completely self-designed. This EMT model is, as will be described, the most extensive model.

Table 3.1: The assumptions, limitations and specifications of the different models. Extensive description will be given in separate sections in this chapter.

Model	**Assumptions**	**Limitations**	**Mass transfer**
Isenthalpic	Inviscid Constant total enthalpy Constant total entropy Single fluid	No discontinuities No surface tension	HEM
Euler	Inviscid Single fluid	No surface tension	HEM
Enhanced Mass Transfer (EMT)	Single fluid	No surface tension	Modified Zwart-Gerber-Belamri cavitation model

3.1 Quasi 1D Setup

Since no discontinuities are present for the second study by Nakagawa [2] a simpler flow solver could be used. In the first study, discontinuities occur and a shock capturing scheme must be deployed. The theory behind these schemes was explained in Section 2.7. In this chapter, it will be explained how these flow solvers are implemented. The same nozzle geometries should be studied to allow comparison with the paper by Nakagawa. As mentioned earlier, the two nozzles for both studies are slightly different and are shown in Figure 3.1.

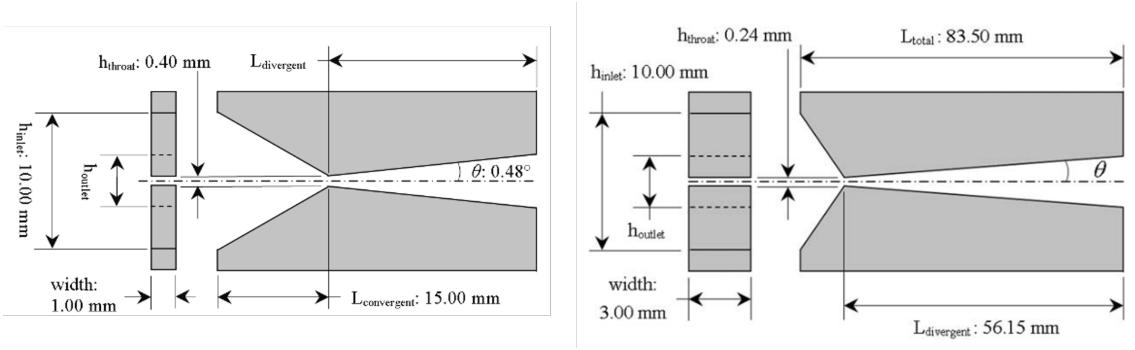

Figure 3.1: Dimensional parameters of the nozzles of the experiments conducted by Nakagawa et al. The left nozzle is used for the case with the shocks [1], while the right nozzle is used for the supersonic exits with various divergent angles [2].

These shapes can be mathematically defined for both the convergent and the divergent sections using slopes and symmetry around the axis. This way, an area distribution is made along the length of the nozzle.

3.1.1 Geometry

The computational domain of this problem is two-dimensional. Although both the nozzle with supersonic outflow and with shock waves are 3D-created actual nozzles, the choice of 2D geometry was made to save computational costs in the beginning. Moreover, a 2D problem is more convenient to start, since it is more user-friendly to find and solve complications. Also, the nozzles in the experiments are rectangular, and thus allow the geometry to be axisymmetric.

The geometries establish the inlet as the coordinate system's reference (x = 0), with both the convergent and the divergent represented by a positive value (following the flow direction from left to right). The horizontal axis (y = 0) represents the symmetry line. All graphs detailing the simulation results will follow the same convention. This applies to both reference cases. The geometries for both reference cases can be seen below in Figure 3.2 and Figure 3.3:

Not all experiments in both reference cases will be performed in this research with the EMT model. For each reference case, two or three experiments are chosen.

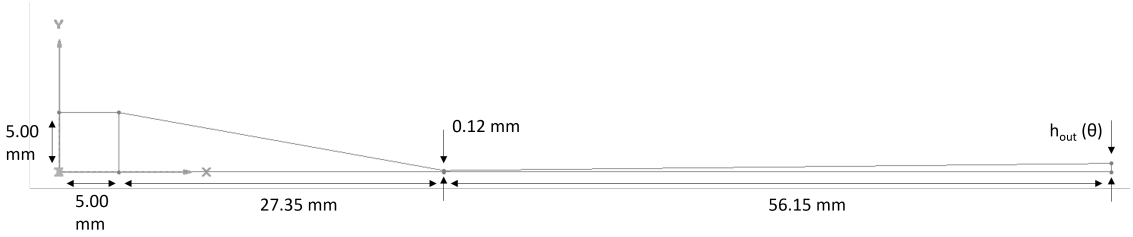

Figure 3.2: Nozzle geometry with dimensions. The experimental nozzle with the supersonic outflow. The outlet is dependent on the divergent angle θ and can vary. [2].

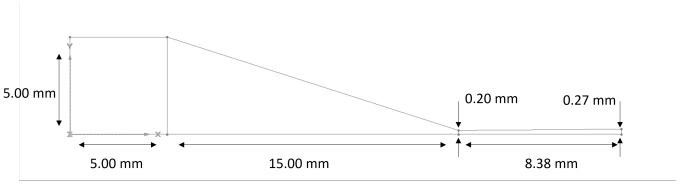

Figure 3.3: Nozzle geometry with dimensions. The experimental nozzle with a short divergent section. This nozzle is used for the reference case where shocks are observed [1].

The specifications of these simulations for both reference papers can be found in Table 3.2, whereas Table 3.2a shows the specifications for the supersonic outflow and Table 3.2b for the shock waves. The results of the simulations will be compared to these cases.

3.1.2 Numerical implementation: Isenthalpic solver

As for the isenthalpic solver, the numerical implementation is not complicated. The algorithm of this flow solver and thus how it is implemented numerically is shown in Figure 3.4. It starts with initialising the nozzle and flow conditions. Subsequently, the sonic conditions in the throat can be calculated. With the knowledge of sonic conditions, the remaining part of the nozzle is computable.

Table 3.2: The specifications and inlet conditions of the simulations that will be performed for both the supersonic and the shock wave reference cases.

Case	θ [deg]	p_{in} [bar]	T_{in} [K]
1	0.153	91	310.15
2	0.306	91	308.95

(a) Supersonic, [2]

Case	θ [deg]	p_{in} [bar]	T_{in} [K]	p_{exit} [bar]
1	0.48	90	313.15	50.1
2	0.48	90	313.15	56.9
3	0.48	90	313.15	59.6

(b) Shock waves, [1]

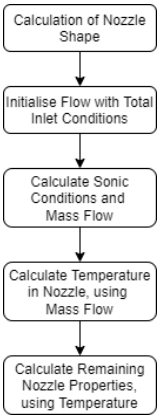

Figure 3.4: Schematic of the algorithm of the Quasi 1D Isenthalpic solver

To calculate the sonic conditions, a root finding function has been used to evaluate the corresponding temperature. The total enthalpy is known at the inlet of the nozzle and assumed constant. Furthermore, $M = 1$ is assumed at the throat and by means of temperature and constant entropy, the remaining variables can be calculated $h(T_*, s)$, $c(T_*, s)$. The entropy is the stagnation entropy which can be determined using the stagnation temperature and pressure at the inlet. This sonic calculation results in the following formulation:

$$f = h_\mathrm{t} - h - \frac{(Mc)^2}{2}, f(T_*) \to 0. \tag{3.1}$$

With a known temperature in the throat, the density and speed of sound can be calculated for this value: $\rho(T_*, s)$, $c(T_*, s)$. At last, the mass flow can be calculated by means of Equation 2.4, where $u = Mc$ which obviously reduces to $u_* = c$ at the throat.

Since mass is conserved, the mass flow is constant throughout the nozzle. Hence, Equation 2.6 can be solved similarly with a root finding function for the rest of the nozzle. This results in the following formulation:

$$f = h_\mathrm{t} - h - \frac{1}{2}\left(\frac{G}{\rho A}\right)^2, f(T) \to 0. \tag{3.2}$$

Consequently, the temperature field throughout the nozzle is known and together with the constant entropy, the rest of the variables can be determined.

3.1.3 Numerical implementation: 1D Euler

For the flow solver with discontinuities, the flow field can be characterised by the Equations 2.17 - 2.19. These 1D Euler equations without energy dissipation and wall

friction can describe any flow. For the nozzle with the changing area, the following quasi-1D Euler equations can be formulated for the mixture:

$$\frac{\partial}{\partial t}\begin{vmatrix}\rho\\ \rho u\\ \rho e_\mathrm{t}\end{vmatrix} + \frac{\partial}{\partial x}\begin{vmatrix}\rho u\\ \rho u^2 + p\\ \rho h_\mathrm{t} u\end{vmatrix} = -\frac{1}{A}\frac{dA}{dx}\begin{vmatrix}\rho u\\ \rho u^2\\ \rho h_\mathrm{t} u\end{vmatrix} \tag{3.3}$$

where, $h_\mathrm{t} = e_\mathrm{t} + p/\rho$ and $e_\mathrm{t} = e + u^2/2$.

The area of the nozzle is described by the first part of the right-hand side. Hence, the area is differentiated with respect to the flow direction and multiplied by its negative inverse. After the nozzle, the shape has been defined in the code, and total pressure and temperature inputs have been given, the flow field initialises. Subsequently, the solving procedure starts. In the end, convergence criteria must be met. The whole algorithm can be schematically seen in Figure 3.5.

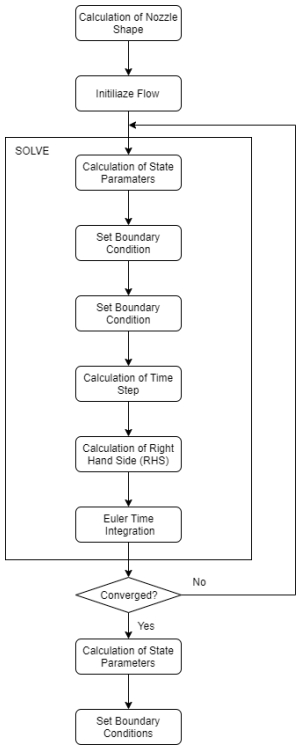

Figure 3.5: Schematic of the algorithm of the Quasi 1D Euler solver

The solving procedure begins with the implementation of the boundary conditions at the inlet and the outlet which are defined as inputs to the problem. Next, the time step and the Right Hand Side (RHS) are calculated. So far, these steps are determined using the 'old' variable values. Finally, with the time period just calculated, the new state can be determined by means of explicit Euler time integration: $q^{n+1} = q^n + \mathrm{RHS}(q^n) \cdot dt$, where q represents the state and the superscript n the state.

As already mentioned in Section 2.7, the RHS needs a more unique treatment since discontinuities are present. Approximate Riemann solvers are used to resolve this problem. In this code, the AUSM method has been implemented. AUSM is a flux vector splitting scheme where the flux is split into two parts, based on the sign of characteristic variables. The process of numerically implementing this method is described below:

$$\mathrm{RHS}(q) = \mathrm{RHS}(\mathrm{AUSM}(q)) - \mathrm{SVA}(q) \tag{3.4}$$

$$\mathrm{SVA}(q) = -\frac{1}{A}\frac{dA}{dx}\begin{vmatrix} \rho u \\ \rho u^2 \\ \rho h_\mathrm{t} u \end{vmatrix} \tag{3.5}$$

$$\mathrm{RHS}(\mathrm{AUSM}(q)) = -\frac{1}{dx}\left(Flux_{\mathrm{right}} - Flux_{\mathrm{left}}\right) \tag{3.6}$$

where SVA stands for Source Variable Area and defines the area distribution of the nozzle and $Flux_{\mathrm{right}}$ and $Flux_{\mathrm{left}}$ are defined as follows:

$$Flux_{\mathrm{right}} = \begin{vmatrix} flux^{(0,1)} & \cdots & flux^{(0,j_{\max}-1)} & flux^{(0,j_{\max})} \\ flux^{(1,1)} & \cdots & flux^{(1,j_{\max}-1)} & flux^{(1,j_{\max})} \\ flux^{(2,1)} & \cdots & flux^{(2,j_{\max}-1)} & flux^{(2,j_{\max})} \end{vmatrix} \tag{3.7}$$

$$Flux_{\mathrm{left}} = \begin{vmatrix} flux^{(0,0)} & flux^{(0,1)} & \cdots & flux^{(0,j_{\max}-1)} \\ flux^{(1,0)} & flux^{(1,1)} & \cdots & flux^{(1,j_{\max}-1)} \\ flux^{(2,0)} & flux^{(2,1)} & \cdots & flux^{(2,j_{\max}-1)} \end{vmatrix} \tag{3.8}$$

where these fluxes are index-dependent. Namely, $flux^{(i,j)}$ can be defined as:

$$flux^{(i,j)} = \begin{cases} max(0, M_{pn})\rho^{(j)}c^{(j)} & +min(0, M_{pn})\rho^{(j+1)}c^{(j+1)} & ,\text{if i} = 0 \\ max(0, M_{pn})\rho^{(j)}u^{(j)}c^{(j)} & +min(0, M_{pn})\rho^{(j+1)}u^{(j+1)}c^{(j+1)} + p_p + p_n & ,\text{if i} = 1 \\ max(0, M_{pn})\rho^{(j)}h^{(j)}c^{(j)} & +min(0, M_{pn})\rho^{(j+1)}h^{(j+1)}c^{(j+1)} & ,\text{if i} = 2 \end{cases} \tag{3.9}$$

where i represents the appropriate row of the conservation rule (mass, momentum or energy) and j an integer of the cell in the axial direction. Hence, the index $(j+1)$ refers to the right state, and (j) refers to the left state. The remaining unknown variables p_p & p_n represent positive and negative splitting p. These are described as: $p_{p/n} = 1/2(1 \pm M)p$, , where the signs are pluses for p_p and minuses for p_n. M_{pn} is the sum of the negative and the positive splitting, M_n&M_p. These are described as: $M_{p/n} = \pm 1/4(M \pm 1)^2$, where the signs are pluses for M_p and minuses for M_n

3.1.4 Speed of sound

As for both types of solvers, the speed of sound problem arises when a phase change occurs. This treatment of this problem has already extensively been considered in Chapter 2. Both the pressure and the full equilibrium relaxation models were implemented for both solvers. The reason to choose the pressure equilibrium as well is since Fluent implements this method in its own software (which can not be adjusted). The formulation of these different speed of sound models can be found at Section 2.8.4, Equation 2.34 - 2.35.

For both solvers, the procedure is similar to some extent. First, the phase of the flow is checked at the relevant conditions. If it is a single phase or supercritical, a direct call to REFPROP is made to calculate the speed of sound. If the phase indication returns a two-phase state, the speed of sound calculation procedure is enabled. It determines saturation properties at the current pressure or temperature. Consequently, it can determine the holdup fraction in combination with the quality of fluid at that state. Finally, Equations 2.34 - 2.35 can be used.

3.1.5 Validation & Limitations

Since so far two models are used to solve the flow field through nozzles, it is also possible to compare these different models. Moreover, these two models incorporate no actual mass transfer mechanism and thus should their results be similar. The isenthalpic flow solver, however, is not able to properly solve the flow field with the presence of discontinuities. Hence, the comparison between these two models must be made for the reference case with the supersonic outflow. Minor changes should be made to the Euler model as a different outlet pressure boundary condition should be implemented (supersonic outflow) and the shock capturing scheme can be neglected.

The comparison between these models is nozzle independent as long as it is possible for both models to properly resolve the problem. In this way, if the similarity is of a high level, it is more likely the models are correct. The two models are plotted side by side in the upper plot of Figure 3.6. Beneath this plot, the percentage difference is calculated. A strong deviation is visible near the throat, where the Euler model expects a more sudden change in pressure while the isenthalpic model describes a smooth transition along this part. For the rest of the nozzle, a high degree of similarity is achieved.

With the extensive dependency of the models on the speed of sound calculation, it is also interesting to further investigate the effect of this. After implementation of the Equations 2.34-2.35 in the models, it should be possible to reproduce Figure 2.9.

Since indeed the same figure can be reproduced in Figure 3.7, a successful implementation is achieved. However, it is more interesting to compare the difference in outcome between these two speed of sound formulations. This comparison will be performed in the supersonic outflow nozzle with the isenthalpic model. This model

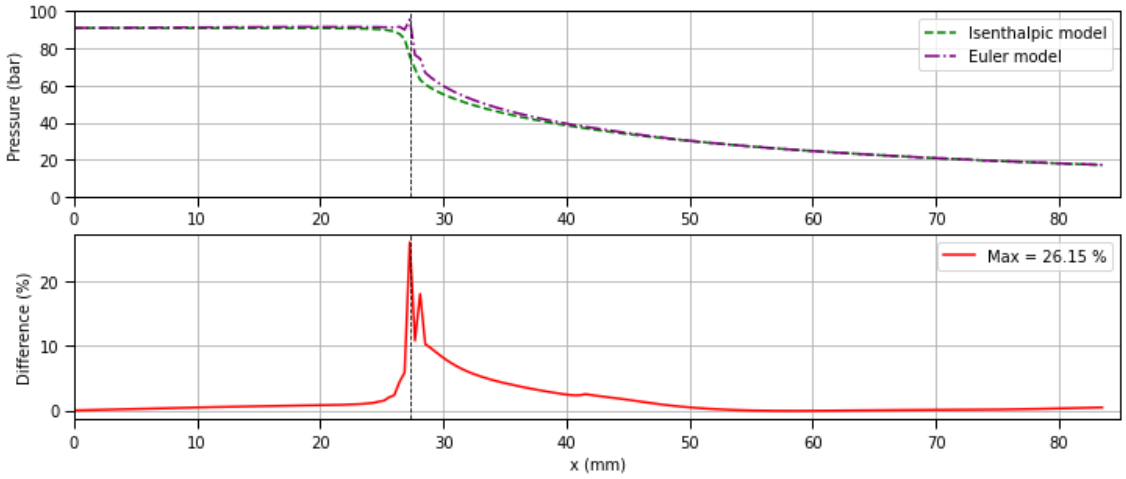

Figure 3.6: Comparison of the pressure of two flow models. In the upper plot, the two pressure curves along the nozzle are presented. In the lower plot, the percentage difference is shown.

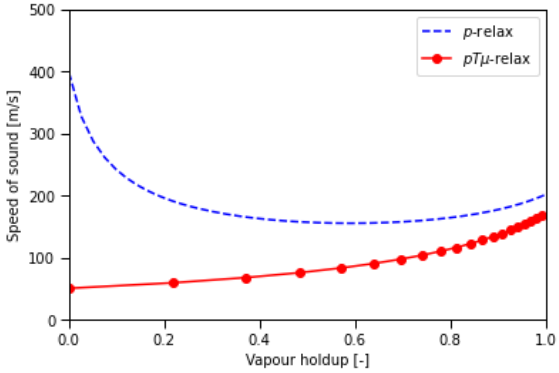

Figure 3.7: Validation of the two different speed of sound implementations.

is by far the fastest in calculating the solution so seems the logical choice.

Before doing so, it is convenient to highlight the first limitation of the isenthalpic flow model. Since with this model, a supersonic flow is desired in the divergent section, Equation 3.2 is solved with enforcement in the desired temperature. With these types of isenthalpic solvers, both a supersonic and subsonic solution exist for the diverging part of the nozzle and thus two temperatures can be found for which Equation 3.2 approaches zero. For supersonic flow, a lower temperature is required and thus the algorithm will be forced to search for the lower temperature after the throat.

In this comparison in Figure 3.8, the following is visible: the upper plot presents a repetition of the dimensions of the nozzle to identify the labels in the two plots below. The second and third plots both show the functions described in Equation 3.1 and

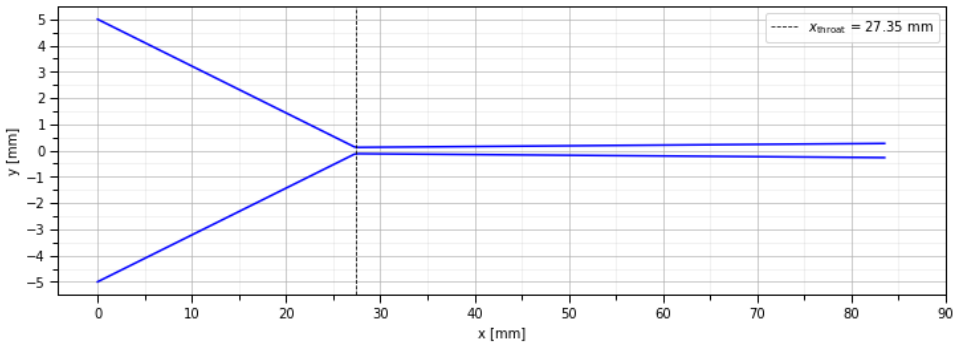

(a) Nozzle geometry

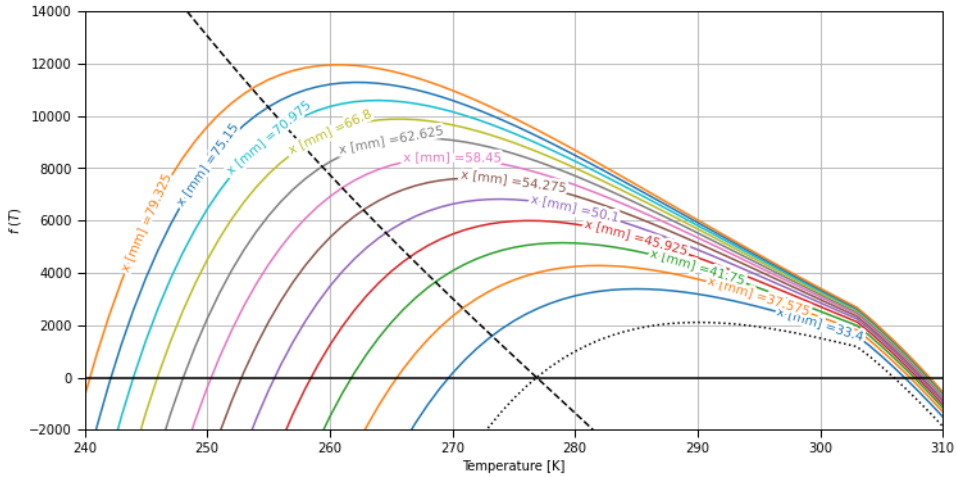

(b) Pressure equilibrium

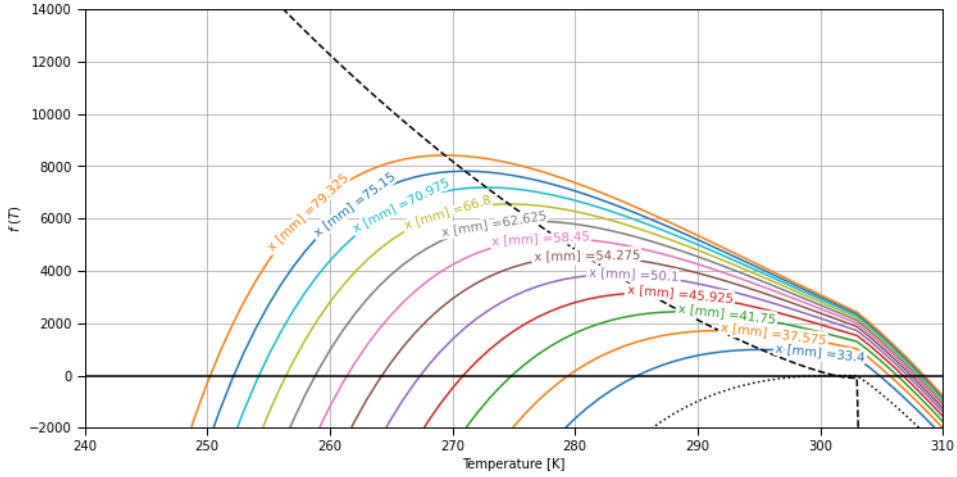

(c) Full equilibrium

Figure 3.8: In the upper plot the nozzle geometry. The lower two show function residuals of Equations 3.1 and 3.2 per area section in the diverging part of the nozzle as function of temperature.

Equation 3.2. The second figure shows the functions with the implementation of the pressure equilibrium. The third figure shows the functions with the implementation of the full equilibrium.

The two possible temperatures (subsonic and supersonic) for each area section after the throat are the intersections of Equation 3.2 with the horizontal axis. The left intersection of the area section line agrees with the supersonic solution. The right intersection with the subsonic. The function for the choked condition (Equation 3.1) is represented by the dashed black line. This line has only one solution and intersects the line at the same point for where in Equation 3.2, $x = x_{throat}$ (the black dotted line). The temperature for which the function is zero, and thus is found by the rootfinder in the model, is the choked temperature ($T^* \approx 276K$ and $T^* \approx 301K$ for the pressure and full equilibrium respectively).

There are a few things which are interesting about the figures. First of all, there exists a large difference in the found choked temperature by the models. This is due to the large difference in choked speed of sound: 155 ms^{-1} and 85 ms^{-1} in the pressure and full equilibrium respectively. Secondly, the supersonic solutions of the pressure equilibrium show much lower temperatures as well. The first area section after the throat (blue line, label: 29.225 mm) is around 275 K for the pressure equilibrium, whereas the full equilibrium expects a temperature of around 292 K.

Thirdly, the pressure equilibrium shows inconsistent behaviour between the choked solution and the solutions for the diverging part. As where for the full equilibrium the choked solution intersects the solutions for the diverging part in their maximum, the pressure equilibrium is off by a significant amount. The results of the full equilibrium model are expected, as the diverging part approaches the throat ($x \to x_{\mathrm{throat}}$), and the two possible solutions also approach the choked solution. This is, however, not the case for the pressure equilibrium.

An assumption of the full equilibrium model is, however, that the choked condition is right at the phase line. The pressure equilibrium does not make this assumption and could be able to dive into the two-phase area before reaching the throat. This of course can be checked in a $T - s$ diagram if this is true, see Figure 3.9. As expected, the choked condition starts at the phase line for the full equilibrium model, while the pressure equilibrium penetrates the two-phase area. This will have a significant impact on the pressure expansion. Obviously, this will result also in lower throat pressure. This is visible in Figure 3.10, where the dashed line represents the full equilibrium model and the line with the dots the pressure equilibrium.

The full equilibrium shows a more transition in the throat and presents expected behaviour for the rootfinder of Equations 3.1 & 3.2. Also, it matches the numerical results of Nakagawa [1] better. Therefore, the full equilibrium was chosen as the model to go forward with for these numerical simulations.

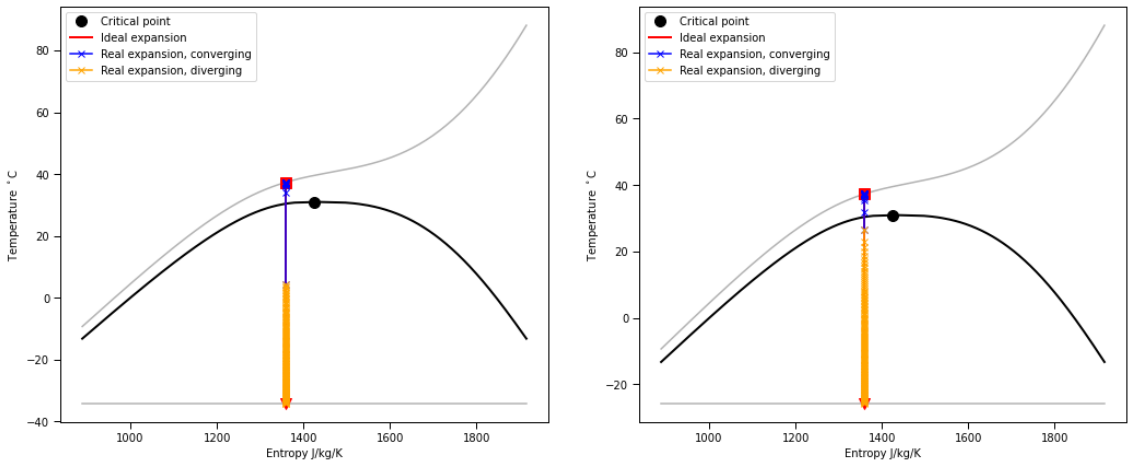

(a) Pressure equilibrium

(b) Full equilibrium

Figure 3.9: Temperature-entropy diagrams of the different speed of sound models. It can be seen in 3.9a that there is a penetration in the two-phase area. Subfigure 3.9b shows the full equilibrium model with the choked condition at the saturation line.

3.2 CFD Setup

All aspects of the CFD simulations will be covered in this section. The mesh treatment will be discussed and emphasis will be placed on the implementation of the numerical methods. In addition, extensive attention will be paid to the way in which the PVT data is applied within the software. Finally, the treatment of the mass transfer model will also be dealt with.

3.2.1 Meshing process

The meshing process was carried out in Pointwise. To make sure an adequate comparison can be done within the different models, both a 1D and a 2D mesh were made. The 1D mesh was created to precisely compare the results with the quasi-1D model in Python and heavily reduce CPU time. Subsequently, the simulations can continue in a 2D mesh.

The process of making a 1D mesh is similar to the more common 2D mesh, except that there exists only one cell along the y-axis. Hence, the flow properties differ only in the x-direction. This method greatly reduces the number of cells and thus the time needed for calculations. To capture the effects of the flow properly, a finer distance was used at regions of the nozzle where large gradients were expected (i.e. large pressure drop). The 1D mesh is shown in Figure 3.11.

The nozzle shown in Figure 3.11 is used for the supersonic outflow cases. The meshes created for the nozzles where shock waves are observed are built in a similar

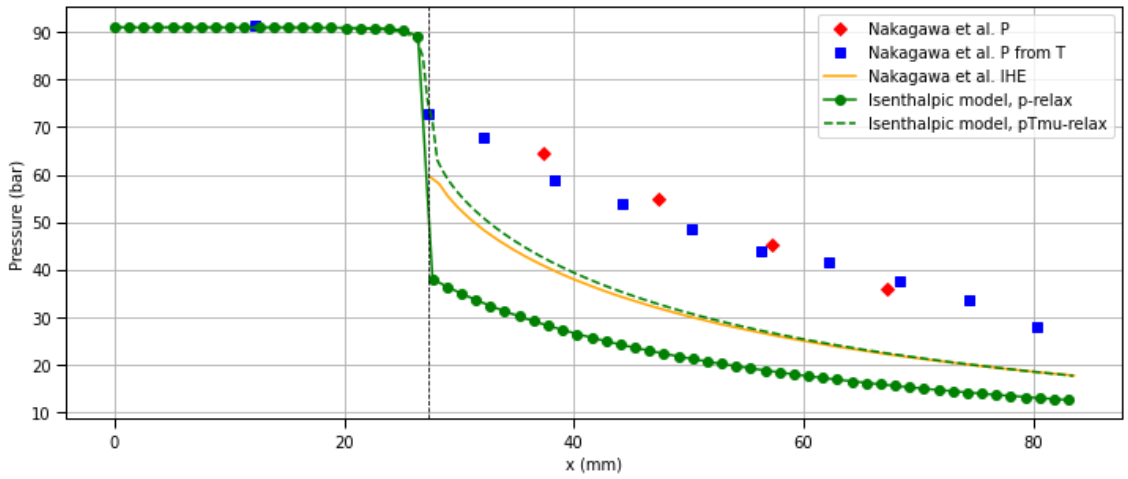

Figure 3.10: Depressurisation of the nozzle for the two different speed of sound models: the pressure equilibrium and the full equilibrium.

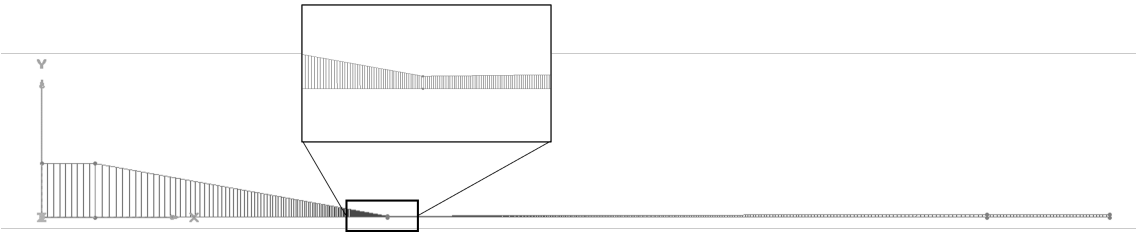

Figure 3.11: Nozzle with one-dimensional mesh. Finer mesh is observed near the throat. This nozzle is used for the reference case where the supersonic outflow is observed [2].

way and are attached to Appendix B. The mesh shown in Figure 3.11 has 845 cells in the $x-$direction. The geometry for the nozzle with the shock waves is much smaller and thus has a smaller amount of cells: 273.

3.2.2 Boundary Conditions

Four boundary conditions are needed by the model to simulate the flow properly. Obviously, the upper lines represent a smooth wall where an adiabatic no shear condition is applied. Symmetry is defined at the lower part of the geometry to replicate the results for the total nozzle. At the outlet, a fixed pressure is defined. If this was not available or known, the divergent part was prolonged and back pressure was guessed and iterated to get proper results.

In the case of the supersonic outflow, no back pressures were known. A prolonged exit was used to impose a boundary condition at the end of this section. This exit pressure was iterated to low pressure, such that all flow in the divergent section

showed supersonic behaviour. It was possible that a shock wave still was created at the beginning of this prolonged exit. It is expected this did not have any influence on the flow in the nozzle before.

In inlet conditions, pressure values were often given and hence the logical choice for the inlet boundary condition. However, this requires Fluent to calculate a velocity at the inlet to get this pressure. Numerical convergence was reached more efficiently when starting with a mass flow or velocity inlet condition. Since no slip is assumed between the phases, these inlet values need only to be set for the mixture. This value for the velocity or mass flow inlet condition was iterated to get the desired inlet pressure. When this created pressure inlet was close enough (i.e. $\pm 5bar$) to the desired inlet pressure, a pressure boundary condition could be applied.

In the case of multiphase calculations, a vapour fraction is also needed. At the inlet, this was set to zero for both reference cases as their starting point originated from the dense (liquid or supercritical) phase. At the outlet, this condition differed from case to case.

Because the Mach number in a two-phase mixture has no unambiguous definition (a comprehensive treatment of this matter is provided in Section 2.8.3), the supersonic outflow was thought to represent a possible concern. To test for the presence of critical flow at the throat, the mass-flow rate was verified to be constant while adjusting the nozzle's output pressure. Despite having a supersonic Mach number at the outflow, the absolute pressure of the flow was found to meet the static pressure applied at the outlet in many circumstances. This flow pattern is characteristic of subsonic regimes and is most likely owing to the software's inability to appropriately evaluate the supersonic outlet conditions for a mixed flow.

As a result, a sensitivity analysis was carried out to see whether various outlet boundary conditions and geometries may affect the results. Three distinct circumstances were investigated:

1. A normal pressure BC at the outlet of the nozzle without any adjustment

2. The addition of a simple straight section at the end of the divergent section. Also, a pressure BC was imposed at the end of this prolonged nozzle.

3. The addition of a diffuser downstream of the divergent section and a static BC imposed at the end of this prolonged section

The three different nozzles can be seen below in Figure 3.12. The first boundary condition was discarded rather quick since it was not able to converge a solution. The second and third boundary condition were further analysed. In the end, the prolonged exit of number two showed to more consistent results. The diffuser exit did not always converge since a shock wave happened often at the beginning of the diffuser.

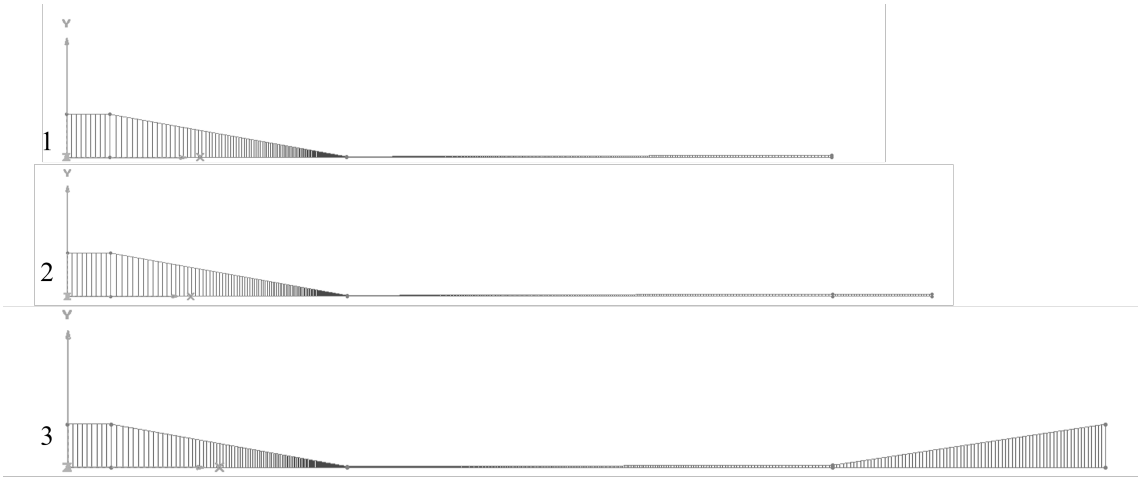

Figure 3.12: Different outlet boundary conditions for the nozzle. This type is used in the reference case where no shocks are present [2]. First, the normal nozzle, secondly the prolonged straight exit and thirdly the diffuser exit.

3.2.3 Numerical method

CFD flow equations

Fluent employs the finite volume method for the discretisation and solution of the Reynolds Averaged Navier Stokes equations. ANSYS Fluent solves mass and momentum conservation equations for the mixture flow. An extra equation for energy conservation is calculated for flows involving heat transfer or compressibility [42], which is the case for this problem.

Because the density-based solver is incompatible with multiphase models, the pressure-based solver was used (except for Wet Steam, but not of interest since the *Materials* can not be edited). For the first simulations, a pressure-velocity coupling (SIMPLE) was used. However, it was discovered over the course of the job that it was not the greatest option for obtaining convergence. Instead, a Coupled approach was used, which involved the simulation of all flow equations. Moreover, this is the recommendation of Fluent for a more robust and faster-converging model in the case of multiphase simulations [42].

Unless otherwise noted, all findings presented here use second order spatial discretisation techniques for all equations except the Volume Fraction, for which it is unavailable. Depending on the application, rather small under relaxation factors were used, particularly for the flow Courant number. When quick convergence could not be obtained, a First Order solution was calculated first and then utilised as the foundation for refinement. Also, the Pseudo-Time method seemed helpful for reaching convergence in the beginning.

When Multiphase models are enabled, Fluent proposes to use PRESTO! (short

Table 3.3: Fluent numerical solver settings.

Type setting	Treatment
Solver	Pressure Based
Gradient	Leas Squares Cell Based
Pressure	PRESTO!
Pressure-velocity coupling	Coupled
Spatial discretisation	Second Order Upwind
Volume fraction	First Order Upwind

for PREssure STaggering Option) as the Pressure discretisation scheme. Moreover, it disables First and Second order methods. PRESTO! is more unusual since it directly calculates the actual pressure values (the 'staggered pressure') on the face cell from the discretisation of the differential equations, rather than from an expression starting from the cell centre [42].

The pressure on the faces is interpolated using the cell centre values in standard pressure discretisation. PRESTO! discretisation for pressure, on the other hand, estimates pressure on the face. This is achievable with staggered grids that do not have velocity and pressure variables "co-located". Because interpolation inaccuracies and pressure gradient assumptions on boundaries are averted, PRESTO! discretisation generates more precise results. PRESTO!, on the other hand, is more computationally expensive since "alternative" grids require more memory.

A summary of the settings mentioned above can be found in Table 3.3.

No firm criterion for convergence was imposed on the simulations. Residuals were tracked to show convergent behaviour. This could mean a flat line or oscillating behaviour at low residual values (i.e. 10^{-3} for all and especially continuity). Also, mass flux reports were considered, and the difference between mass inlet and outlet should be negligible.

Multiphase Model

CFD techniques must be able to resolve two features of flashing flows (1) phase change during flashing flow and (2) interaction between the liquid and vapour phases. Both of these features are briefly discussed below. The models may be divided into two types when it comes to phase change: (1) the ones that consider the nucleation mechanism, which usually agrees to a greater degree with the actual behaviour of the flow but need experimental data to tweak the source term of this nucleation, and (2) the ones that ignore the nucleation mechanism and assume fixed bubble size or number density of nucleation points, with fabricated coefficients to control non-equilibrium effects [31].

Two techniques are widely used to model this interaction between the two phases during the vaporisation process: (1) the Euler-multi-fluid approach and (2) the

mixture approach [42]. The governing equations are averaged in the Eulerian multi-fluid method per phase, and turbulence is commonly modelled using the Reynolds-Averaged Navier–Stokes (RANS) equations for large-scale simulations. Interfacial exchange terms must take into consideration the interaction between the phases. These exchange conditions, which are generally referred to as closures, must incorporate the following: (1) momentum transfer between the two phases, (2) impacts of dispersed bubbles on continuous phase turbulence, and (3) bubble coalescence and break-up processes that define bubble size distribution [31]. However, most of the time, these closures are based on experiments, and these are hardly accessible for these usages.

The mixture approach, on the other hand, is more robust and easy to use. In general, the Mixture Model is the most basic choice for multiphase flows in Fluent; the term comes from the fact that the code solves momentum, continuity, and equations for the mixture rather than single phases. It can account for velocity slip (calculated using algebraic expressions) and thus can be used to model non-homogeneous flows (though it assumes local equilibrium at short spatial length scales); however, as previously stated, this was not of interest in the current case, so the flow was assumed to share a single velocity field between the phases.

The Mixture Model was determined to be the best option based on the software specifications. The Volume Of Fluid (VOF) Multiphase Model might also be used to solve this problem; however, this was only considered for non-interpenetrating phases (such as sludges). While the Euler-multi-fluid approach may give greater accuracy, it was found that the Mixture Model produced satisfactory results. Also, the most significant challenge is establishing convergence. As a result, the Eulerian model's extra complexity and numerical instability precluded its usage.

3.2.4 Thermodynamic implementation

The Span-Wagner EOS, described in Section 2.6, is not available in Fluent. However, Fluent allows for a complete specification of thermodynamic characteristics via so-called user-defined materials. As a result, their utilisation was required for the model's implementation.

The direct solution of the equation at runtime is technically conceivable but would be challenging to implement and would unduly slow down the solution process. As a result, a new strategy - lookup tables - was used. Essentially, a set of tables representing all essential material properties (e.g., enthalpy, entropy, specific heat) as a function of two independent thermodynamic variables are created ahead of time and kept in memory. The software may read from the tables at runtime and interpolate between the nearest values to return the desired attribute.

This method has apparent drawbacks, the most significant of which is that it can only map a specific region of the thermodynamic plane. As a result, proper table boundaries must be chosen with care to encompass all potential flow circum-

stances inside the domain. Another concern is the number of points in the table and the interpolation method used; dense enough tables must be created to minimise interpolation errors.

The CFD software requirements and architecture typically dictate the number and kind of properties necessary, as well as the two independent variables required for table compilation. ANSYS Fluent treats pressure and temperature as independent variables, though density is also supported. The provided attributes vary and are determined by the programme architecture.

In general, constructing Lookup Tables from intensive characteristics (such as $p-T$) indicates that two-phase states cannot be represented (unlike in the $T-s$-plane) and that a third variable, in the form of volume or mass fractions, is necessary for the calculation of the whole flow state. This appears to make $T-d$-tables a superior alternative, at least in terms of Fluent. However, two problems occur.

To begin, Fluent represents a single phase with a single set of tables. As a result, there is no compelling need to tabulate two-phase states. However, even if a set of tables is utilised to depict a complete two-phase mixture, a difficulty occurs in the compilation of areas falling between saturation and spinodal lines. If metastable states are to be considered, these regions are inherently ambiguous: in terms of $T-s$ (comparatively for $T-d$), a single point could correspond to both metastable vapour and a two-phase mixture.

As a result, two sets of tables must be built, similar to what is required for $p-T$ tables, and proper programming to resolve between them is relatively complicated. In contrast, uncertainty develops between metastable vapour and subcooled liquid phases in $p-T$ tables; this is considerably easier to resolve because just mass or volume fractions are required.

The transition line, on the other hand, suggests a problem with table compilation. If the entire tables are written, there will be a strong discontinuity at the transition line (whether saturation or spinodal) between vapour and liquid characteristics. Figure 3.13 displays a depiction of a sample density table with the discontinuity indicated by the saturation line. Even if a single set of tables is used to represent a single phase, this is problematic since, in general, the software may be unaware of the transition line. As a result, the solver may request an input lying beyond it during the solution process, which will result in a crash.

All lookup tables were created and saved as ASCII files using Python scripts; thermodynamic calls were made using a program that connects REFPROP and its libraries to Python and enables easy and concise syntax. The function allows requesting metastable attributes. Metastable qualities, unlike equilibrium states, are naturally ambiguous; a single input can result in two distinct thermodynamic states (e.g. metastable vapour or subcooled liquid). REFPROP overcomes this problem by adding an additional input that pushes its search into one of the phases. As a result, this value was added to the list of necessary input values. Forcing the computation of implausible thermodynamic inputs, such as vapour states below the

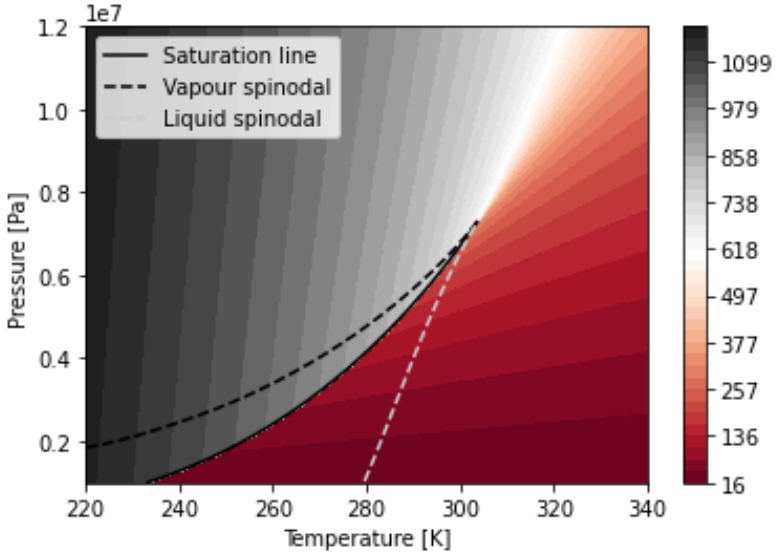

Figure 3.13: Contours of the density of CO_2 in $kg \cdot m^3$ in a $p - T$ plane. A large jump in density is observed around the transition line.

Table 3.4: LUT size specifications.

Variable	Points	Spacing
p	400	0.3 bar
T	400	0.3 K

spinodal, will result in an error.

Finally, because metastable characteristics in REFPROP may only be called using functions of temperature and pressure or temperature and density, using $p-T$ as independent variables substantially simplified the table authoring operation. If many independent variables were required, a more complex solution incorporating bi-dimensional interpolation would be necessary.

The resolution in the LuT tables will most probably have an effect on the results. Too large spacing between temperature and pressure points will cause substantial interpolation errors. However, increasing the table size excessively is not desired either, since this will result in disproportionate computing costs for the generation and reading. Therefore, a middle way will have to be found that results in a good compromise where both these extremes do not apply.

This point of balance was found in creating tables with 400 table points in both the temperature and the pressure arrays. Larger tables did not result in significantly better resolution and computing costs were within an acceptable range. The result of this dimensional analysis can be found in Appendix C. The specifications of the 400x400 Look-up Table can be found in Table 3.4.

Phase definition

Fluent provides numerous options for user-defined materials. Technically, Fluent may be coupled to REFPROP to either give the attributes directly or construct lookup tables automatically. This option, however, is limited to a single material and is directly linked to the REFPROP standard formulation - the inclusion of metastable properties is not straightforward, and, most importantly, a property request in a physically unfeasible area (beyond the spinodal; this may happen during the first iterations) would return an error from REFPROP and thus crash the software. As a result, this functionality could not be used, and a User-Defined-Real-Gas-Model (UDRGM) was created instead; this consisted of a C-file that was generated, then compiled inside Fluent to create the necessary libraries, and finally loaded.

The main difficulty with this approach is that only one UDRGM may be used at a time, and each UDRGM can only simulate a single material, i.e. a single phase. When it comes to evaporation, liquid qualities are somewhat less critical than vapour properties. As a result, the decision was simple, and this model was used to simulate the vapour phase. To get past the problem and incorporate the liquid phase, a solution was developed, which will be detailed more below.

Moreover, by using the UDF and the UDRGM, the compressibility of both phases is properly taken into account. By default, it is only possible to treat one phase as compressible. However, Fluent allows for multiple compressible phases by using UDFs. Without treating both phases as compressible, the simulations would not provide proper results as the liquid phase was always thought to be incompressible.

Primary phase: UDRGM

The UDRGM is a collection of C functions that are called directly at runtime and return the desired property values. This, without question, offers far greater flexibility in terms of approaches and solutions. First, a function for handling error messages must be defined. Secondly, the setup must be specified. This function is executed when the simulation is loaded after compiling the UDRGM. When this is implemented, the property-related functions can be defined. Fluent demands that 12 functions are provided and are defined by means of pressure, temperature, density or mass fractions (the latter in the case of mixtures, i.e. a UDRGM for air.).

Tables are read and stored in memory in a single three-dimensional array during the setup procedure. Its dimensions correspond to the number of pressure and temperature points and the number of properties. These numbers must be defined as constant beforehand. Following that, a generic bilinear interpolation function is created, using pressure, temperature, and a numerical index to determine which table will be utilised for interpolation as inputs. Out-of-bounds thermodynamic inputs are handled by clipping and setting them to the minimum (or highest) value available in the table. This is done individually for temperature and pressure; for

Table 3.5: UDRGM properties provided for the implementation of the right EoS data for CO_2.

Property	**Symbol**	**SI Unit**
Density	ρ	$[\mathrm{kg \cdot m^{-3}}]$
Enthalpy	h	$[\mathrm{J \cdot kg^{-1}}]$
Entropy	s	$[\mathrm{J \cdot kg^{-1}K^{-1}}]$
Specific heat at constant pressure	c_p	$[\mathrm{J \cdot kg^{-1}K^{-1}}]$
Molecular weight	M_w	$[\mathrm{kg \cdot kmol^{-1}}]$
Speed of sound	c	$[\mathrm{m \cdot s^{-1}}]$
Dynamic viscosity	μ	$[\mathrm{kg \cdot m^{-1}s^{-1}}]$
Thermal conductivity	λ	$[\mathrm{W \cdot m^{-1}K^{-1}}]$
Change of density with respect to temperature at constant pressure	$\left(\frac{\partial \rho}{\partial T}\right)_p$	$[\mathrm{kg \cdot m^{-3}K^{-1}}]$
Change of density with respect to pressure at constant temperature	$\left(\frac{\partial \rho}{\partial p}\right)_T$	$[\mathrm{kg \cdot m^{-3}Pa^{-1}}]$
Change of enthalpy with respect to temperature at constant pressure	$\left(\frac{\partial h}{\partial T}\right)_p$	$[\mathrm{J \cdot kg^{-1}K^{-1}}]$
Change of enthalpy with respect to pressure at constant temperature	$\left(\frac{\partial h}{\partial p}\right)_T$	$[\mathrm{J \cdot kg^{-1}Pa^{-1}}]$

example, if the temperature is outside of boundaries, the function sets it as the minimum value and proceeds to linearly interpolate between two values corresponding to the minimum temperature and nearby pressures.

Following that, each function associated with a property initialises an integer, which is handed to the interpolation function, which uses it to choose which 2D array (matrix) to utilise for bilinear interpolation. Although 12 functions are normally given, Fluent allows only 11 provided. The remaining function, the calculation of the enthalpy mixture in case of chemical reactions, can be ignored since it is of no interest in this case. The 11 functions Fluent demands (in SI units) are given in Table 3.5:

The phase transition problem, where a jump in properties can occur across the saturation line in the $p - T$ plane, was addressed during the table-writing process. In the table generator, two possibilities were implemented: clipping or extrapolation of the attributes to cover the whole $p - T$ domain. After creating a table in the physically sensible domain, the values were employed as algorithm input, and the resulting function was assessed at previously empty domain locations. The result of this method can be seen in Figure 3.14:

Secondary phase: UDF's

As previously stated, the UDRGM technique presented above can only deal with one phase (namely, vapour). The question of defining the second phase emerges. To add the liquid qualities, another material needs to be defined within the program itself.

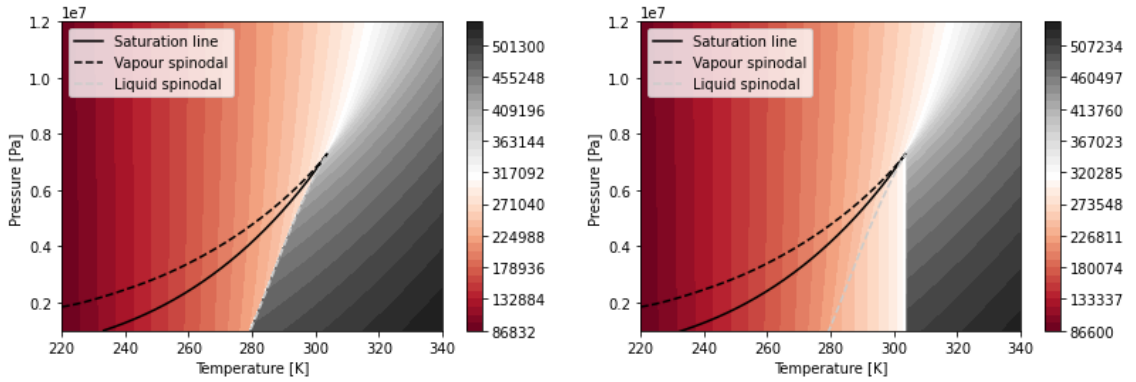

Figure 3.14: Contours of enthalpy values of CO_2 in $J \cdot kg^{-1}$. On the left realistic and feasible values till the liquid spinodal line. On the right, these values have been extrapolated.

Giacomelli [29] used a somewhat different model - a mixed UDRGM - in one study. It is simply a variation of the normal UDRGM that permits various species to be included. The characteristics, which are the same as those given above, are also specified in terms of mass fractions, in addition to the usual thermodynamic properties. It would ordinarily be used to define a mixture of species in chemical equilibrium (the software guide's mixture UDRGM template, for example, describes the air as a mixture of ideal gases). Hence, it must be modified to involve multiphase, rather than multispecies, flows.

Indeed, a two-species model with each species representing a phase should be written. Once the model has been imported into the GUI, the user-defined mixture may be replicated; now two mixtures are present. One will represent the liquid phase, while the other will represent the vapour phase. However, there are still four species, two of which must be eliminated quantitatively. If each mixture is bound to be composed entirely of one single specie - the relevant phase - at inlet and outlet, and diffusion within each mixture is prohibited (by setting the relevant coefficients to near-zero values), each mixture works effectively as a single material, and thus several user-defined materials (coded as species inside the mixture UDRGM) can be used in a single simulation. However, this approach is rather complex. Although attempts were made to incorporate this into the model, no successful implementation was realised and a more simple solution was sought.

Fluent's UDF `DEFINE_PROPERTY` and `DEFINE_SPECIFIC_HEAT` routines, in addition to the more complete models just discussed, allow for the definition of some material properties (namely, density, viscosity, thermal conductivity, speed of sound, specific heat, and sensible enthalpy; the latter two only as a function of temperature).

Strictly, density, sound speed, viscosity, and thermal conductivity all require a distinct `DEFINE_PROPERTY` method to be defined; it was chosen to use lookup tables

once more. The tables themselves are read and stored in memory inside a separate routine called `DEFINE_ON_DEMAND`, which can be executed at any time from the Fluent GUI; a separate function was written for bilinear interpolation, which is called by each routine for the respective property calculation, as mentioned above. In each `DEFINE_PROPERTY` procedure, the separate thermodynamic properties describing flow state were retrieved using Fluent's standard macros (`C_P` for pressure and `C_T` for temperature). The same extrapolation method of the phase values is used as the primary phase, which can be seen in Figure 3.15.

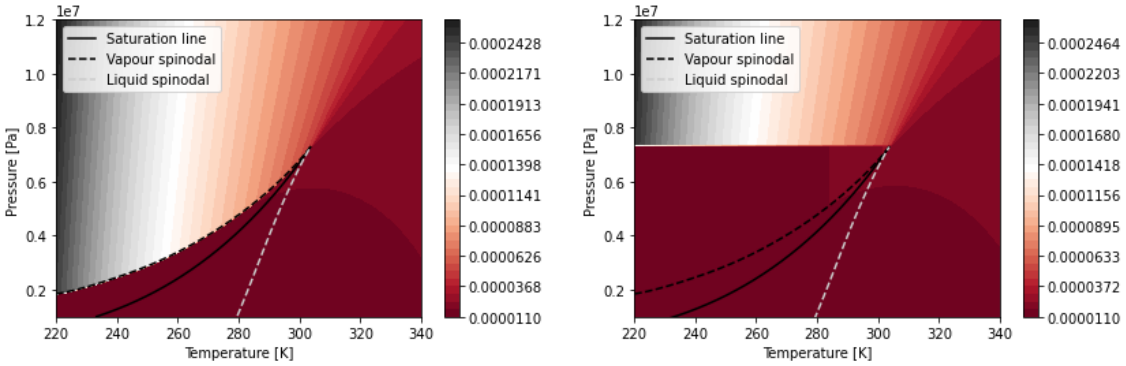

Figure 3.15: Contours of dynamic viscosity values of CO_2 in $\mathrm{kg} \cdot \mathrm{m}^{-1} \cdot \mathrm{s}^{-1}$. On the left realistic and feasible values till the vapour spinodal line. On the right, these values have been extrapolated.

The particular `DEFINE_SPECIFIC_HEAT` function was used to define specific heat. It only accepts temperature as an input and calculates both the specific heat and the sensible enthalpy. This led to the following input, as seen in Figure 3.16. Fluent calculates the sensible enthalpy as the difference with the Standard state enthalpy (as seen in Equation 3.10 which is defined in the GUI alongside the reference temperature. This must be the same value in the `DEFINE_SPECIFIC_HEAT` (divided by the Molecular weight due to a difference in notation). Fluent, on the other hand, calculates entropy internally:

$$H = \int_{T_{\mathrm{ref}}}^{T} c_p \, dT + h^0(T_{\mathrm{ref}}) \tag{3.10}$$

$$s = c_p(T_{\mathrm{mean}}) \cdot \log \frac{T}{T_{\mathrm{ref}}} \tag{3.11}$$

where, T_{mean} is the mean logarithmic temperature difference between the actual and reference temperatures.

This method lacks the accuracy associated with employing a full UDRGM; most notably, the specific heat is constrained to be a function of temperature alone, rather than pressure plus temperature as in a full UDRGM. Now, a certain pressure

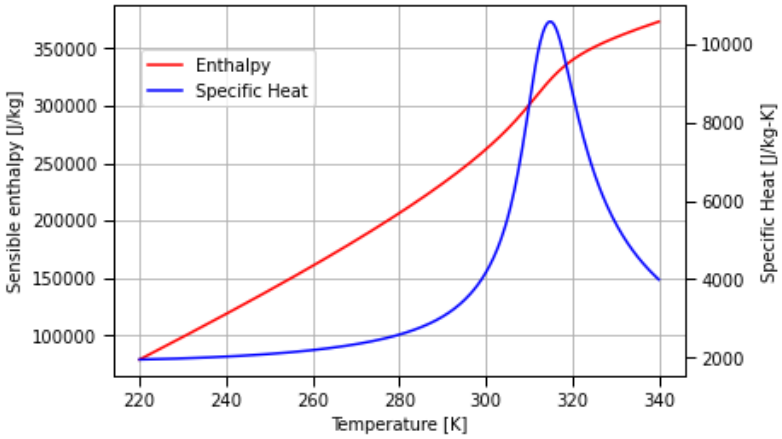

Figure 3.16: Sensible enthalpy and specific heat as a function of temperature for the liquid phase. Both were evaluated at saturation pressures.

array must be defined for which the specific heat and enthalpy are defined at each temperature. Since this property is mainly used for the calculation of the enthalpy of vaporisation, the saturation pressures were considered. This turned out to give satisfactory results. Nonetheless, the limitation should be remembered. If future software updates support several UDRGM's, that would most likely be the most efficient and accurate path.

3.2.5 Mass transfer mechanism

As already mentioned, interfacial exchange terms must be considered. ANSYS Fluent treats these as mass transfers, in which many different types of processes can be modelled. ANSYS Fluent's built-in models (such as the Cavitation model or the Evaporation-Condensation model) can be used, or a mass transfer model can be created. Since there is no universal mass transfer model, ANSYS Fluent includes a UDF that can be used to enter models for various forms of mass transfer, such as evaporation, condensation, and boiling. ANSYS Fluent will automatically add the source contribution to the applicable momentum and scalar equations when this UDF is used. This contribution assumes that the mass "produced" or "destroyed" will have the same velocity and energy as the phase from which it was formed or destroyed [42].

The cavitation models described in Section 2.4.2 may be readily implemented in the framework of the Mixture Multiphase Model using the Cavitation Mass Transfer mechanism in ANSYS Fluent. To identify which mass flux will be considered positive, all such aspects need the declaration of a sign convention in the GUI, in the form of the 'from' and 'to' phases. According to the software convention for the Cavitation model, the liquid phase is the 'from' phase, while the vapour phase is the 'to' phase. The Singhal et al. model turned out to be very unstable as indicated

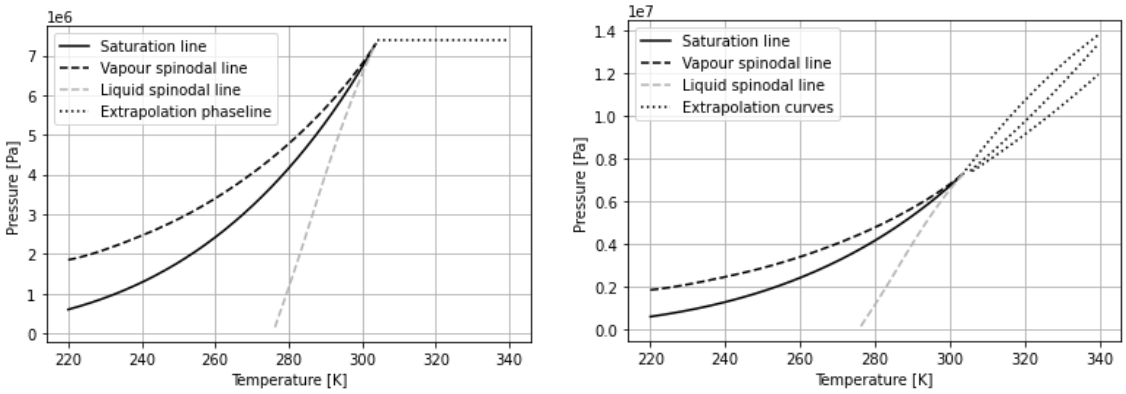

(a) Bound by critical point

(b) Extrapolation

Figure 3.17: Phase lines for the saturation pressure required by the mass transfer mechanism. All are shown for the saturation line and the two spinodal lines.

and reached to no converging solution. In the end, the Zwart-Gerber-Belamri model showed the best results and became the default cavitation model for the simulations [41].

The Mass Transfer mechanism required the saturation pressure to be specified as a constant or as a function of the saturation temperature; this was accomplished using a `DEFINE_PROPERTY` UDF that interpolates between a dense array of temperature and pressure values that was previously compiled from REFPROP with a Python script; it was then stored in memory by Fluent using a `DEFINE_ON_DEMAND` routine. The two arrays were bounded together by the triple and critical points. Another possibility is to extrapolate this curve. Also, it is good to point out that this is the saturation line. However, since this phase line is fed to the software manually, this could be any line (i.e. spinodal line, or any line in between to further/differently account for non-equilibrium effects). These lines, and the possibility of the extrapolation, are shown in Figure 3.17.

In general, the program will need the specification of characteristics for both phases during runtime, even if the phase itself is not active (i.e. its volume fraction is null). Then it activates the source terms, collects the required volume fractions, and uses the conventional lever rule to determine the overall mixture characteristics. This means that property values for both phases must exist in all situations, even if they are physically meaningless (e.g. liquid properties in superheated vapour conditions). They should not be mentioned in the final convergent solution, which is meant to have physical significance.

Chapter 4

Results & Discussion

In this chapter, results obtained from the three models (isenthalpic, Euler and EMT) will be compared to experimental and numerical data from two reference papers [1] [2]. First, the results from the Euler and isenthalpic model will be discussed. Subsequently, the results from the EMT model will follow.

4.1 Shocks

In this section, the Euler model is compared with the data published by Nakagawa et al. [1] for expanding flows in convergent-divergent nozzles. They measured the temperature along the nozzle wall with thermocouples. In the converging section, isentropic flow was assumed and together with the inlet entropy, pressure data in this section of the nozzle was obtained. At the throat, the pressure was calculated by assuming that the phase change occurred at the saturation line. After the throat, in the diverging section, the pressures were calculated by making use of saturated temperatures.

An experiment was chosen in which the inlet condition and temperatures are comparable to real CO_2 pipeline conditions and where clear shock waves were observed, see Figure 4.1. Since the divergent section of the nozzle used in this experiment is only 8.38 mm long, a shock wave must occur only a short distance from the throat. In this experiment, there are three cases considered in which the static exit pressure downstream led to a shock wave in the diverging section. This is the case for 50.1, 56.9 and 59.6 bar as a static pressure in the end. Exit pressures lower than these values have no real observed shock wave. Therefore, these three static back pressures were used.

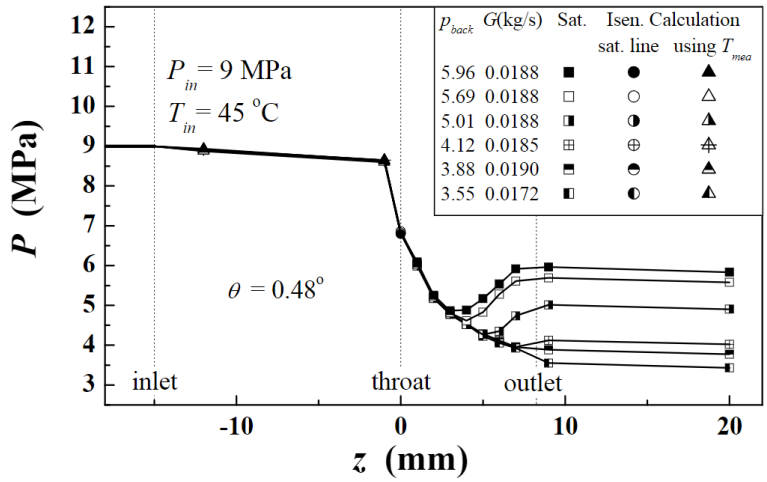

Figure 4.1: Experiment by Nakagawa et al. with an inlet temperature of 45 °C and 90 bar pressure [1].

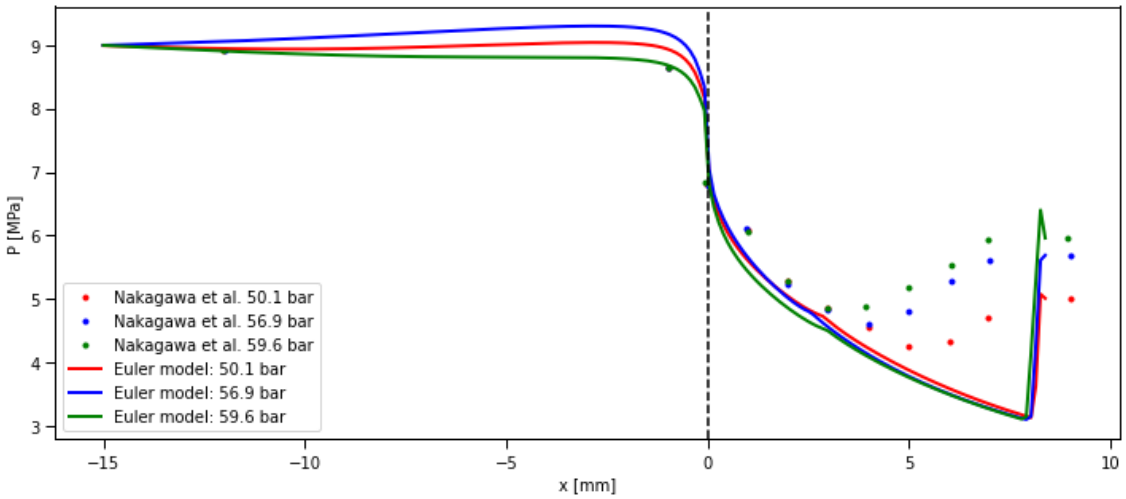

Figure 4.2: Results of Euler model compared to the experimental shock waves by Nakagawa et al. [1].

The results of these simulations in the Euler model can be seen in Figure 4.2. When no supersonic flow is assumed, the solver forces the flow to match the static pressure at the end that has been imposed on. However, since the shock waves are observed at the very end for each static exit pressure, these simulations do not show desirable results. The pressure in the throat, however, is consistent with the experimental data. Hence, the phase change is also expected to happen at the saturation line according to the model.

Of course, it is still interesting to see when the shock waves are obtained by

the model for this nozzle when they are not enforced at the end by the boundary condition. There are two possibilities to investigate this: first, the static end pressure could be increased. As is also visible in the experimental data, an increasing static end pressure decreases the length in the diverging part of the nozzle for the shock to happen. Secondly, the nozzle could be extended. The same divergent angle will be held, but longer diverging sections. At last, it is good to point out that an increasing inlet temperature would also change this. However, inlet conditions were held the same.

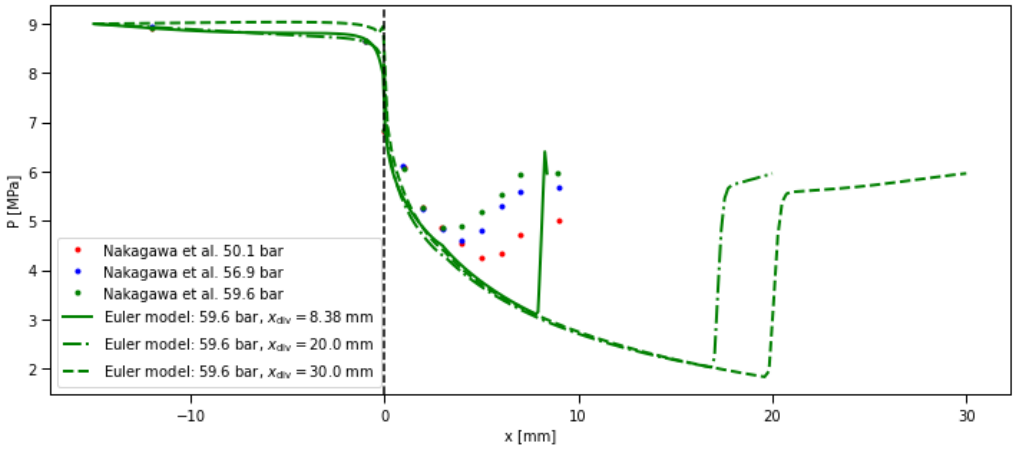

Figure 4.3: Results of Euler model compared to the experimental shock waves by Nakagawa et al. with extended divergent parts.

As can be seen in Figure 4.3, the extension of the divergent section of the nozzle indeed forces the shock wave to exist. For an extended length of a total of 10 mm, no shock wave is observed though. Only after an extension of 20 and 30 mm, the shock waves are expected. The decompression curves of these last two are very similar, as expected. The shock wave of the longest prolonged nozzle happens slightly further than the 20 mm version. The shock wave in the 20mm model is forced earlier, while the 30 mm model does not experience this situation at that point.

Another observation can be made about the shape of the shock wave. Experimentally, the shock waves are rather thick and exist over a longer part of the nozzle. In the model, however, very sharp and thin shock waves are expected. This difference is due to the fact that instantaneous mass transfer is assumed in the model. This is due to the effects of the HEM, as described in Chapter 2. The HEM simply obtains its mass fraction as the relative position in the two-phase area. This is of course not realistic as the mass transfer, in reality, takes time to develop and is not instantaneous.

Also, there are some differences noticeable in the converging section of the nozzle. The longer the extension of the divergent section, the less decrease in pressure is achieved in the converging section. The model with an extension of 20mm seems to

be the best fit for the data. This is also due to a difference in velocity.

As mentioned earlier, higher static end pressure also enforce the shock wave to exist. This can be seen in Figure 4.4. Again, similar behaviour is observed. The dotted curve with the higher exit pressure passes the throat in the saturation point. Also, a similar depressurisation is noticed till the shock. This shock wave is also for the higher pressure thin and sharp.

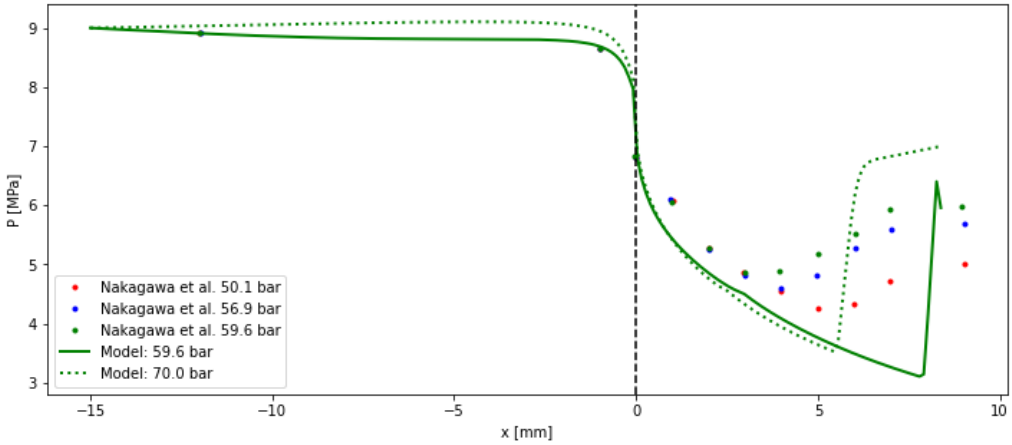

Figure 4.4: Results of Euler model compared to the experimental shock waves by Nakagawa et al. with higher static end pressure.

However, in the same paper by Nakagawa et al [1], also numerical simulations are executed for a longer nozzle. These simulations are performed for several exit pressures of which three have their exit still in the two-phase area. Since longer divergent sections created shock waves, as was seen in Figure 4.3), the Euler model should be able to replicate this. The results are shown in Figure 4.5.

In this Figure 4.5, the Euler model is able to reproduce the pressure curves to a considerably good level. It is noticeable, however, that with reducing exit pressures, the similarity decreases. Also, the Euler model shows unexpected behaviour for the exit pressure of 73.2 bar. After the shock wave, large deviations in pressure are observed. It is expected that the vicinity of the critical point and the combination of REFPROP being unstable in that region, led to this behaviour.

As already stated, the two highest exit pressures have their exit pressure in the single-phase area. This is obvious since the pressure is higher than the critical pressure. For the other three pressure curves, this is hard to notice without knowing the temperature since their pressure is below the critical pressure. A $T - s$ diagram would be preferable, in this case, to visually examine this. This can be seen in Figure 4.6. Here, the expansion curves of 62.7 bar and 88.1 bar as exit pressure have been plotted in a $T - s$ diagram.

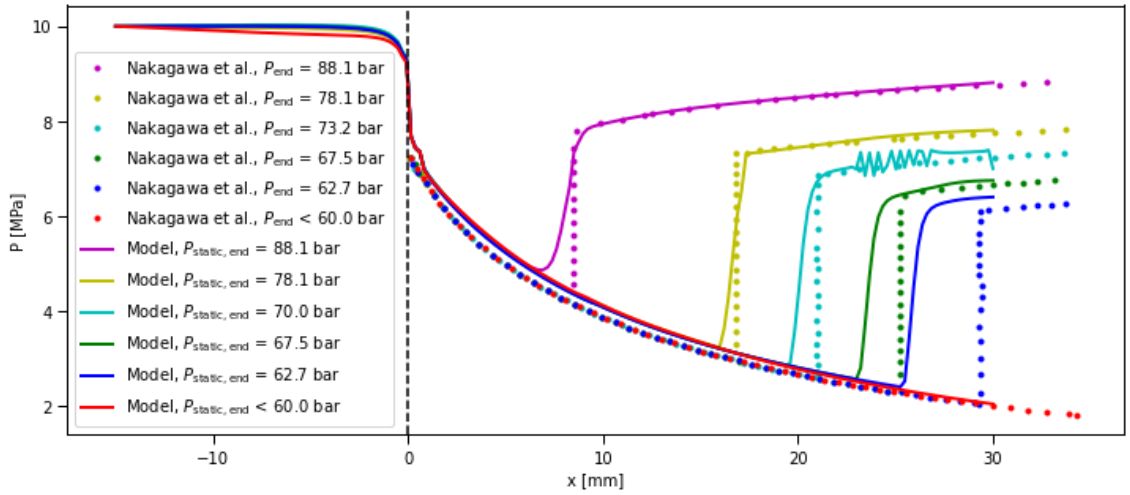

Figure 4.5: Results of Euler model compared to the numerical shock waves by Nakagawa et al. with higher static end pressure.

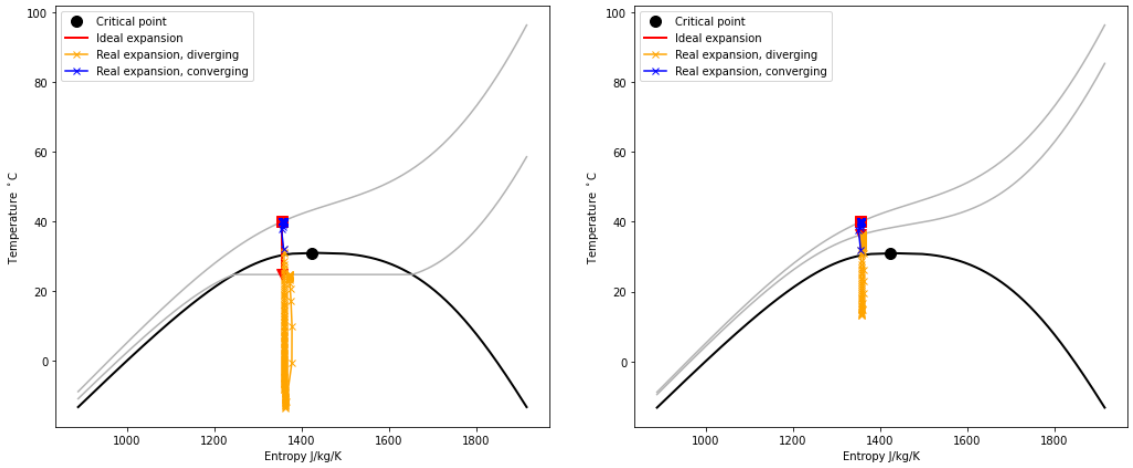

(a) Two-phase exit

(b) Single phase exit

Figure 4.6: Temperature-entropy diagram with the real expansion of the flow in the nozzle. The difference between a two-phase exit and a single-phase exit is highlighted.

In Figure 4.6, the expansion curves are plotted in this $T - s$ diagram. The converging part of the nozzle is plotted with the blue lines and crosses, while the yellow lines and crosses show the diverging part. By separating the expansion in these two sections, it is also clearly visible that the throat is located at the phase line. The shocks are visible too since the yellow lines go up and down. They also show an increase in entropy, which is expected during a shock wave.

The expansion curve of the lower exit pressure (62.7 bar) dives significantly

deeper into the two-phase area than the higher exit pressure (88.1 bar). This should also be visible in their holdup fraction along the nozzle which for the single-phase flow should return to zero. However, for the tho-phase flow, a remaining vapour holdup fraction is expected. This is clearly visible in Figure 4.7.

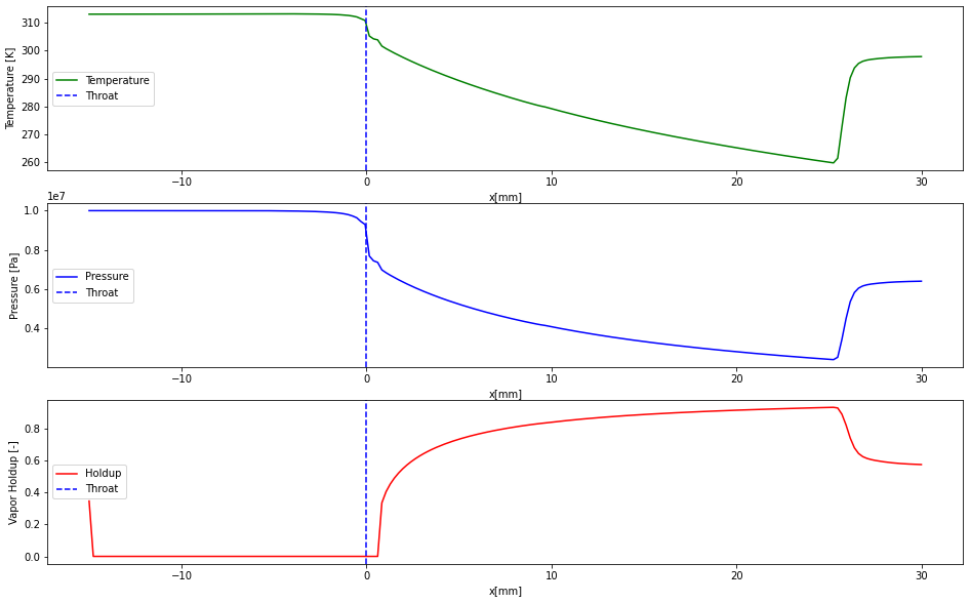

(a) Two-phase exit

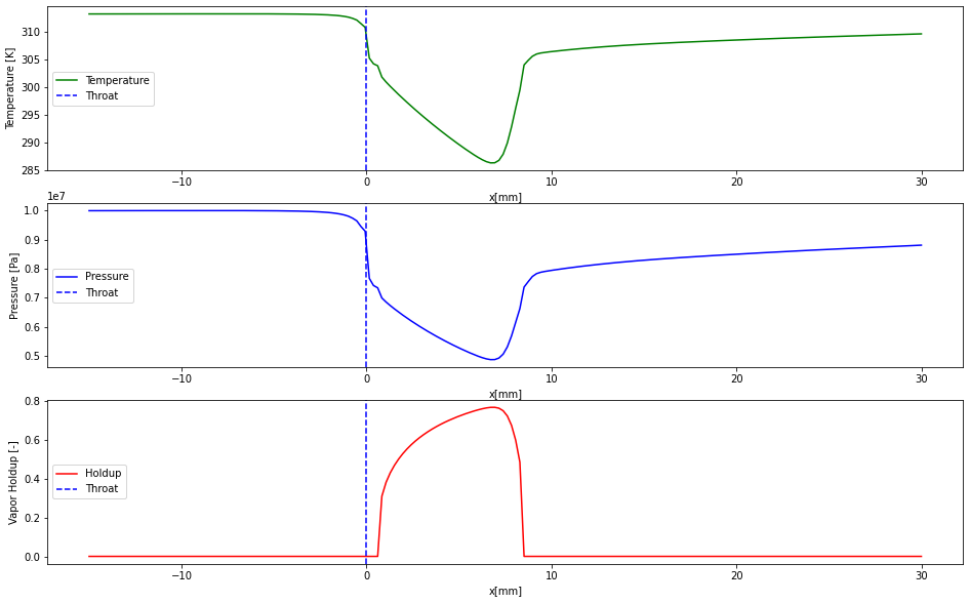

(b) Single phase exit

Figure 4.7: Holdup fraction together with the temperature and pressure along the nozzle axis.

4.2 Supersonic exit

After the first reference paper by Nakagawa et al. [1], a second reference case with a supersonic exit will be examined in which the experimental data will be compared [2]. In this paper, in contrast to the first reference paper, actual pressure data is available. Whereas before pressure was calculated as saturated pressure at a certain temperature by a thermocouple, this experiment has actual strain gauge taps that measure the static pressure.

In this reference paper, simulations are performed with four different nozzles. Their geometries can be seen in Table 4.1. The rest of the geometry of these nozzles can be found in Figure 3.1. Simulations of these nozzles have similar inlet conditions as the experiments in Section 4.1.

Table 4.1: Dimensional parameters of the nozzles of Nakagawa et al. with inlet conditions [2].

Nozzle	θ (degrees)	h_{outlet} (mm)	T_{inlet} (K)	p_{inlet} (bar)
1	0.076	0.39	310.15 K	91 bar
2	0.153	0.54	310.45 K	91 bar
3	0.306	0.84	308.95 K	91 bar
4	0.612	1.44	309.65 K	91 bar

Isenthalpic simulations are performed for all these four nozzles. These are significantly quicker than the Euler model equations and hence have an advantage in solving the flow when no discontinuities are present. As already extensively explained in Chapter 2, entropy and total enthalpy are assumed constant in these calculations. The results of these simulations are shown in Figure 4.8.

As clearly can be seen, very similar results have been obtained with respect to the Isentropic Homogeneous Model (IHE) by Nakagawa et al. This is expected since they used a similar method. However, their numerical results show only the diverging section. Moreover, for nozzle 1 and nozzle 2, no supersonic solution was observed in their simulations. According to the author, the velocity of the fluid was lower than the speed of sound in that case. Of course, this is very dependent on the type of speed of sound formulation. When using the HEM speed of sound formulation, a supersonic solution was possible and the flow was choked at the throat. This can be seen in Figure 4.9.

Here, it is clear that due to the HEM the phase change and the choked condition started at the saturation line, as explained in 3.1.5. After the throat, the expansion continues and the flow becomes supersonic. A maximum Mach number of 1.78 is reached according to the HEM model.

Also, a clear trend is visible in the similarity between the experimental results and the isenthalpic model. The larger diverging angle, the smaller the deviation between the isenthalpic model and the experimental results. At small diverging

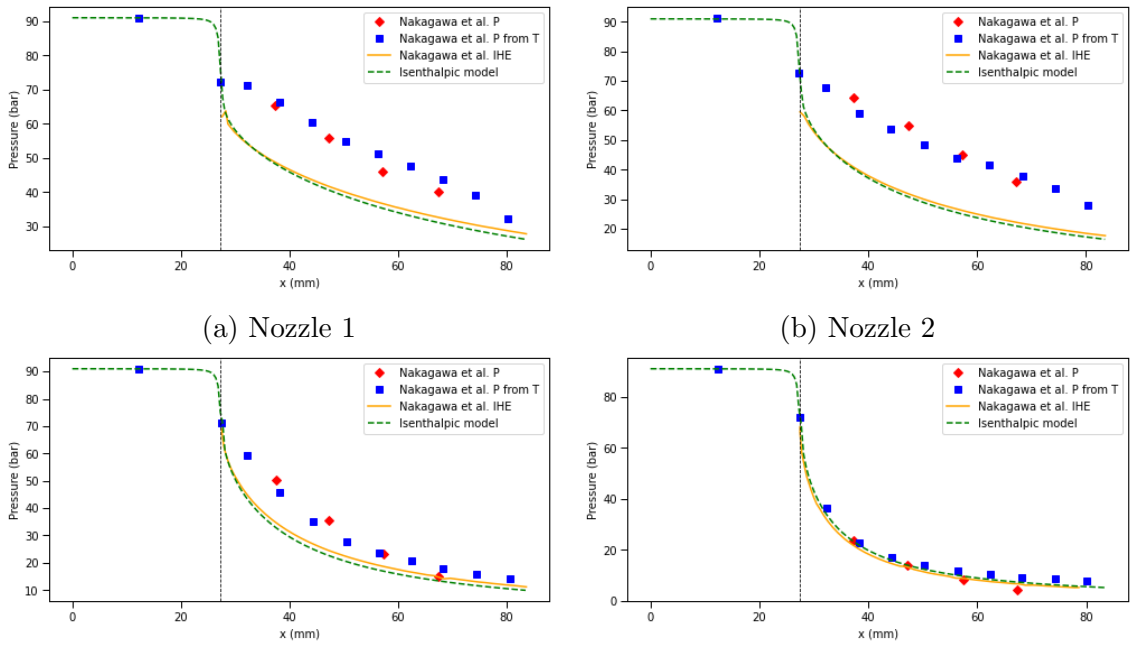

(a) Nozzle 1

(b) Nozzle 2

(c) Nozzle 3

(d) Nozzle 4

Figure 4.8: Decompression curves of the four nozzles with the experimental data as a reference by Nakagawa et al. [2].

angles, the slope of the experimental data approaches linearity, while at wide angles this is far from being the case. Of course, no friction at the wall is simulated in the isenthalpic model and both the temperature and pressure measurements in the experiment perform their measurements at the wall. Decreasing friction at the wall at wide diverging angles could be the explanation.

4.3 EMT results

4.3.1 Supersonic exit

The last model that has been employed, is also the most comprehensive. In Fluent realistic mass transfer models have been implemented to account for a more genuine approach. The cavitation models that were described in Section 2.4 have been used to simulate the cavitation in the nozzles. This section will provide the results of these simulations and compare them to both the other models and the experiments. These outcomes will be discussed qualitatively.

The first simulation that has been performed in Fluent was the case of the supersonic exit. With respect to the reference paper which initiated these experiments, two of the four experiments will be replicated in Fluent. This will be the case for nozzle 2 and nozzle 3, see Table 4.1 for their geometries.

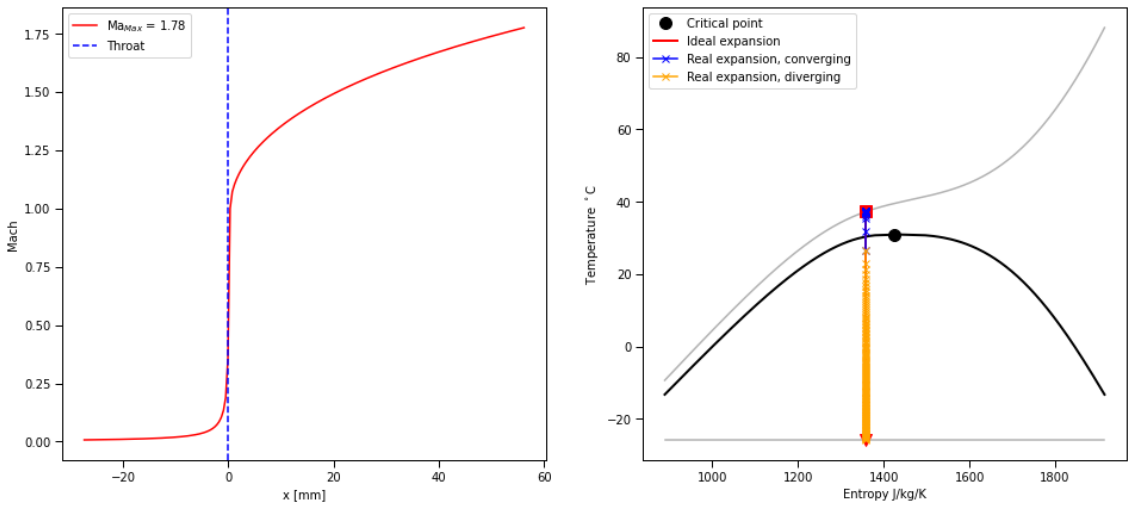

Figure 4.9: Mach number along the nozzle together with expansion curve in the $T - s$ diagram. The flow becomes choked at the saturation line.

In Figure 4.10, the depressurisation curves of all the models are shown by dashed lines. The experimental results of the author are displayed by points. The throat is depicted by the black dashed line between 20 mm and 40 mm.

In this graph, it is clear that the Enhanced Mass Transfer (EMT) model shows the best similarity with the experimental results. Although it is not perfectly analogous, the EMT model shows also the same expansion behaviour as the experiments. Whereas the isenthalpic model and the Euler model show exponential behaviour, the EMT model displays more linearly decompression. This is for the two more narrow nozzles (nozzles 1 and 2 in Table 4.1) also the case.

The results by the EMT model show the greatest deviation of the experimental data in the beginning, just after the throat. From there on, it gradually decompresses to the same pressure at the end. Also, large deviations between the different models are noticeable at this point around the throat. Therefore, it is interesting to further zoom in on this point, as can be seen in Figure 4.11.

In Figure 4.11, the deviations around the throat are more clear. The EMT model shows a very abrupt change of pressure around this point, while the other models have more gradually changing pressure. Also, the point where the model crosses the throat differs between the models. The shock and isenthalpic models are more close to the experimental data point at the throat than the EMT model. However, there is actually a good reason for this.

The EMT model was not able to converge to a solution with the exact inlet conditions ($p = 9.1MPa, T = 310K$). This is due to the fact that the tabulated properties tend to change dramatically around this point. As described in Chapter 3, the implementation of the right thermodynamic properties involved using a significant amount of Look-up Tables. In the case of the UDRGM, also four different

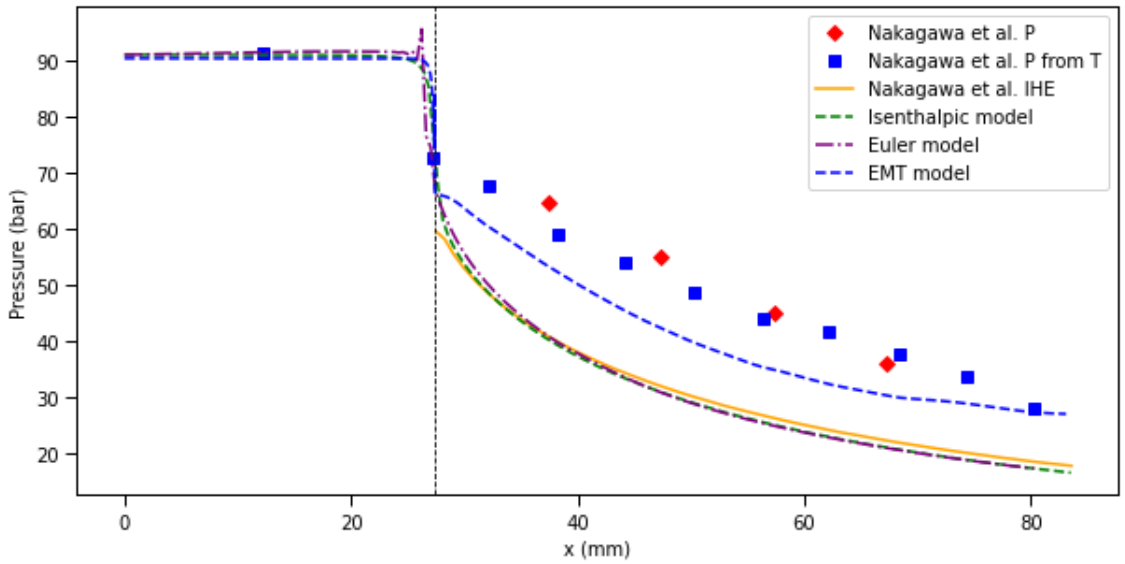

Figure 4.10: Depressurisation curves of all the models in dashed lines. The thick line and points refer to the results of the author.

derivative properties had to be provided (see Table 3.5). Together with the specific heat at constant pressure, these properties show extremely volatile behaviour around the critical point, as can be seen for two of these properties in Figure 4.12.

For the properties shown in Figure 4.12, strong deviations are indeed observed in the vicinity of the critical point. When performing simulations in Fluent with these tables around the critical point, Fluent diverged and was not able to deliver a solution. That is why the inlet temperature has been lowered by a few degrees to avoid the critical point. This of course has consequences for the results. Starting at a lower inlet temperature will lead to crossing the phase line at a different point. For example: when starting at $T = 310$ K, $p = 91$ bar, the starting entropy is closer to the critical value compared to starting at $T = 300$ K, $p = 91$ bar ($s/s_{\text{crit}} = 0.94$ and $s/s_{\text{crit}} = 0.84$ respectively). The entropy is a convenient property to compare these inlet conditions since it will depressurise isentropic to the throat.

The pressure points of those isentropes crossing the phase line can be easily calculated by means of REFPROP. When evaluating $s/s_{\text{crit}} = 0.94$ and $s/s_{\text{crit}} = 0.84$, the saturation pressures are around 72 bar and 60 bar respectively and thus explain the lower pressure at the throat. In the end, the inlet conditions were chosen such that they were as close to 310 K but also converged. Of course, it will remain uncertain if a higher pressure at the throat also will lead to more similarity. This is a flaw in the current model which would be interesting to solve, but no successful attempt was obtained in doing so.

For the other nozzle (nozzle 3, see Table 4.1), a more steep depressurisation is expected than the expansion in nozzle 2. This more sudden depressurisation is

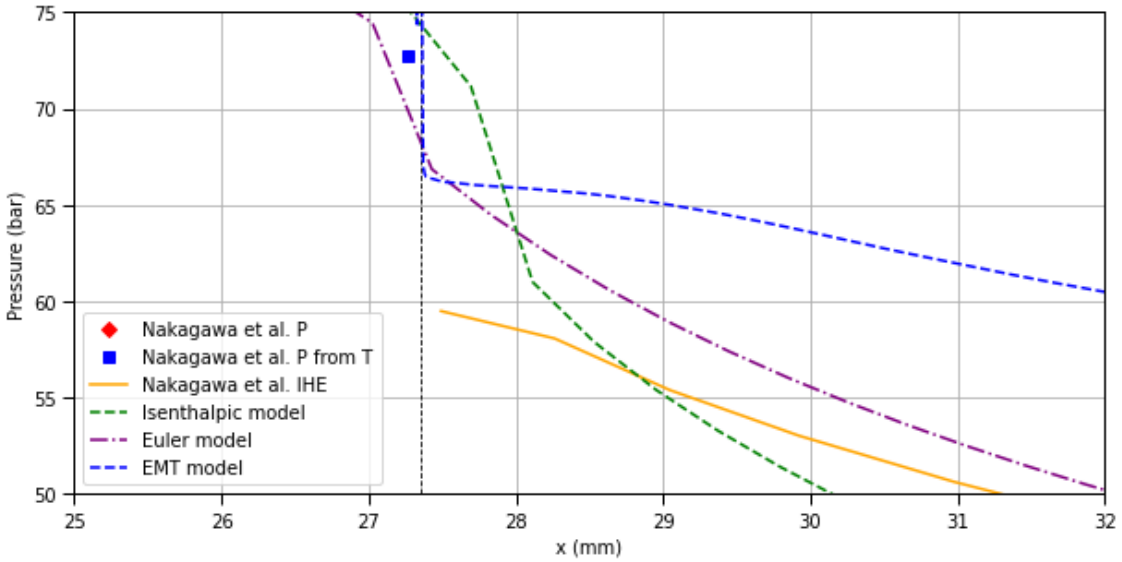

Figure 4.11: Zoomed in part of Figure 4.10 at the throat.

logical since a wider diverging angle is applied. This was also predicted by both the isenthalpic and the Euler model. The results of the simulation of the flow in the EMT model can be seen in Figure 4.13

Similar behaviour is observed with respect to a more narrow nozzle. It matches the experimental pressure data by Nakagawa et al. quite well. Also, it did not expect such a steep depressurisation as the other two models. The flaw of the critical point, however, is still present. The EMT model was not able to converge a solution when starting at 310 K. Lower temperatures had to be initiated to find a converging solution. This has the same effect as before, where the expansion curve intersects the phase line at too low pressure.

4.3.2 Shocks

For the experiment with the supersonic exits, the EMT model was able to match the experimental pressure points to a reasonably good level. This difference in outcome compared to the other models is most likely due to the difference in mass transfer treatment. Empirical cavitation models explained in 2.4 were implemented whereas this was not carried out in the other two models.

The EMT model was also tested for the reference case with experiments of shock waves. The same experiment was replicated as in Figure 4.1. Just as for the Euler model, only simulations were performed where a shock occurred before the exit of the nozzle ($P_{\text{exit}} = 50.1\text{bar}, P_{\text{exit}} = 56.9\text{bar}, P_{\text{exit}} = 59.6\text{bar}$). As was shown in earlier sections of this chapter, the Euler model was not able to capture any shocks properly like in the experiments. Although it was possible to enforce a thin and sharp shock

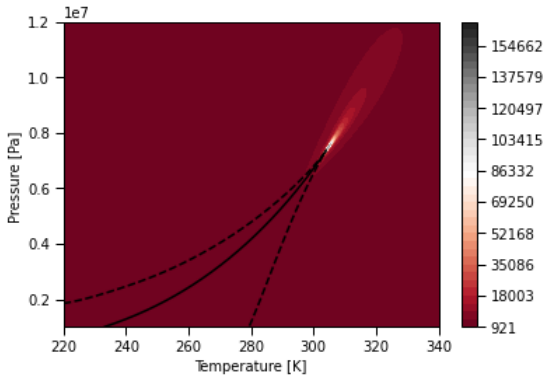

(a) Specific heat C_p for LuT in $[\mathrm{J \cdot kg^{-1}K^{-1}}]$

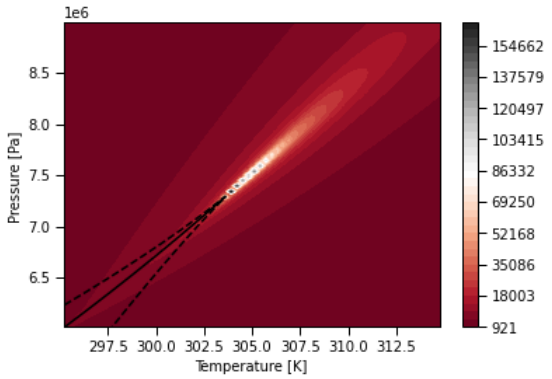

(b) Specific heat C_p for LuT in $[\mathrm{J \cdot kg^{-1}K^{-1}}]$, zoom on critical point

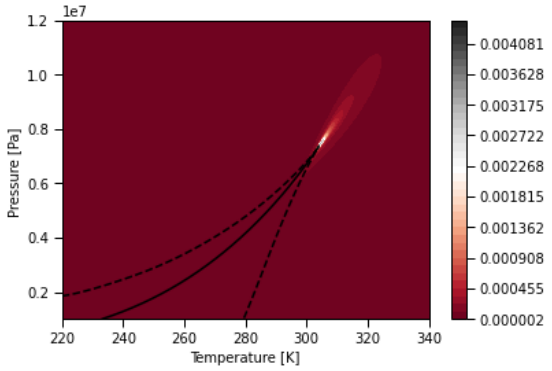

(c) Derivative property $\left(\frac{\partial \rho}{\partial p}\right)_T$ in $[\mathrm{kg \cdot m^{-3}Pa^{-1}}]$

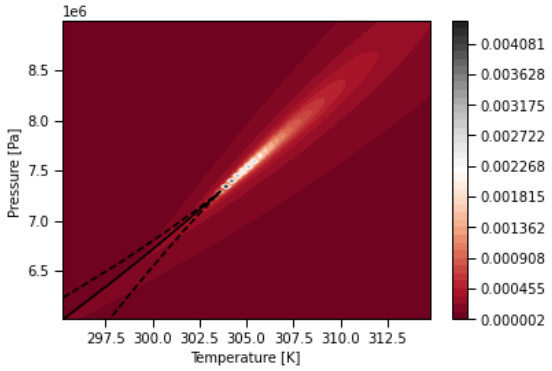

(d) Derivative property $\left(\frac{\partial \rho}{\partial p}\right)_T$ in $[\mathrm{kg \cdot m^{-3}Pa^{-1}}]$, zoom on critical point

Figure 4.12: Contours of Look-up Tables used for Fluent simulations. Extreme deviations are noticeable near the critical point.

right at the end of the nozzle, this did not result in the desired outcome.

It was determined the exit pressures were too low for the current nozzle length. Longer divergent sections and higher exit pressure were used in extra simulations to validate this hypothesis. As shown and discussed earlier in this chapter, the Euler model was able to perform better simulations. Also, the numerical experiments by Nakagawa et al [1] were replicated with a proper level of similarity.

The results of the simulations by the EMT model for the shock wave experiments can be seen in Figure 4.14. The experimental data by Nakagawa is shown by solid points with a different colour corresponding to the exit pressure. The results by the EMT model are displayed by dashed lines matching the colour of their right reference case.

As can be seen clearly, Fluent is able to simulate the flow with the presence of shocks. Although for the lowest pressure ($P_{\mathrm{exit}} = 50.1\mathrm{bar}$) the shock appears at the

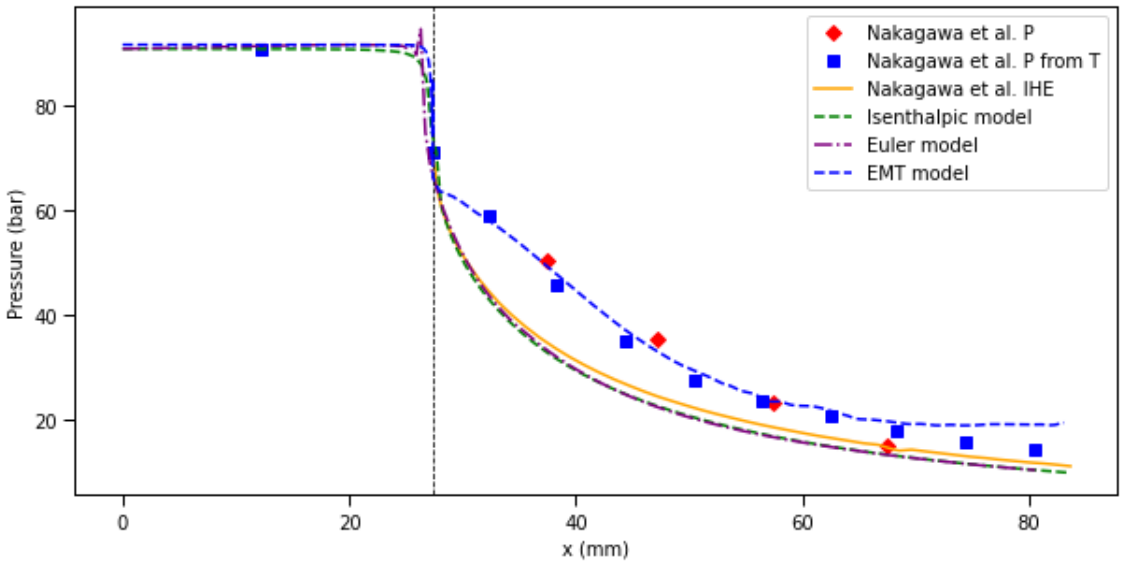

Figure 4.13: Depressurisation curves of all the models in dashed lines. The thick line and points refer to the results of the author.

exit of the nozzle, the other two exit pressures show the shock wave in an earlier stage. However, it is also evident that the flow does not match the experimental data set over the whole length of the nozzle. At the beginning of the expansion after the throat, depressurisation shows similar behaviour. It is only when the shock wave appears in the experiments, that the model starts to diverge with the experimental data.

In the experiments, slow and thick shock waves are observed. This happens because the mass transfer is not instantly fast and takes time to develop. As could be seen earlier with the Euler model, this could not be incorporated and very thin shock waves were created. Similar results are visible with these simulations performed by Fluent. More thin and sharp shock waves are observed and also lower pressures are obtained during the depressurisation. However, as explained in Section 2.4, it is possible to tweak this solution by means of the evaporation and condensation coefficients for the cavitation model (F_{vap} and F_{cond} in Equations 2.12, 2.13).

The default values of these coefficients are 50 and 0.01 for F_{vap} and F_{cond} respectively. These can be modified to any value and can be case specific. While evaluating the current depressurisation curves, it is possible to achieve more desirable results by adjusting the coefficient in the favoured direction. In this case, during evaporation, the model tends to follow the experimental data considerably. However, from the onset of the shock wave with the increase in pressure till further downstream, the current model diverges. Thus, by lowering the condensation coefficient F_{cond}, it should be possible to delay this part.

In Figure 4.15, the effect of this operation is shown. By lowering F_{cond} with a

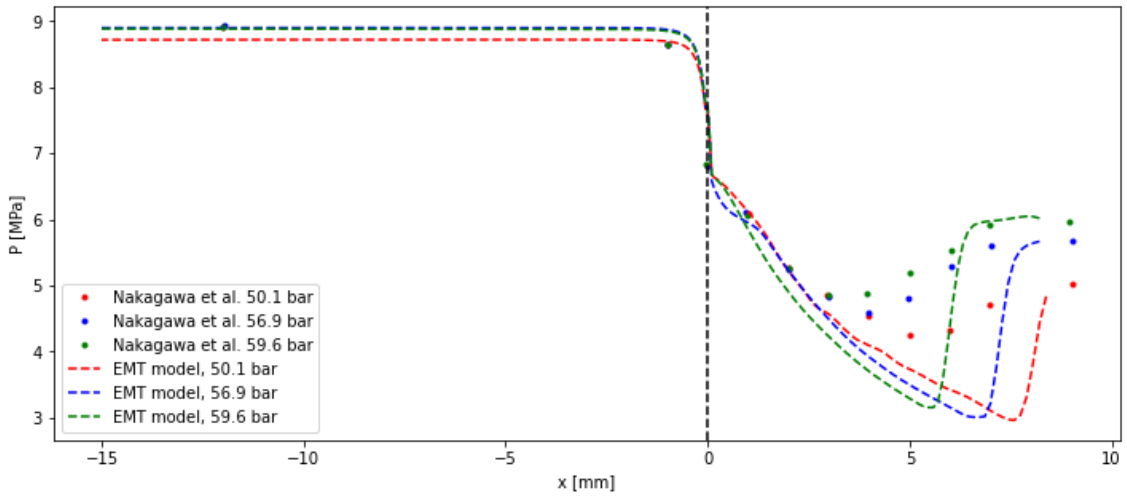

Figure 4.14: Depressurisation curves of the EMT model for different exit pressures.

factor 10 (from 10^{-2} to 10^{-3}) the dotted line was created. The original simulation, shown by the dashed line, is also visible to compare the results. As can be seen clearly, the improved similarity is achieved with the modification of the cavitation model. The pressure does not decrease as much as before and starts earlier with increasing the pressure. Thus, a thicker shock wave is created.

This can be fully fine-tuned to achieve the desired results. Also, the other adjustable parameters can be modified such that an even more similar outcome can be produced. These parameters, the bubble radius R_B and the nucleation site volume fraction α_{nuc}, were not modified though. The modification that was performed to achieve the dotted line in Figure 4.15 also explains why the simulations of the supersonic exit were considerably similar as well. Since no modification was necessary to the evaporation coefficient F_{vap}, the mass transfer model worked analogously with the supersonic exit where no condensation occurred. This provides additional confirmation that the cavitation model also works for multiple simulations. If new coefficients had been required for each simulation, this would not have improved the reproducibility of the model.

Although these modifications achieve proper results and seem consistent throughout the simulations, some remarks must be made. Reducing the F_{cond} made physically sense, since a thick shock wave was observed in the experimental data and a thin shock wave in the previous simulations. However, the physics might be different in reality. Since the surface tension of CO_2 is relatively low in the two-phase area, it could be possible that a mist or fog will occur instead of larger bubbles. It is clear that for the current multiphase model the modifications are the obvious choice, but this could be different with another model.

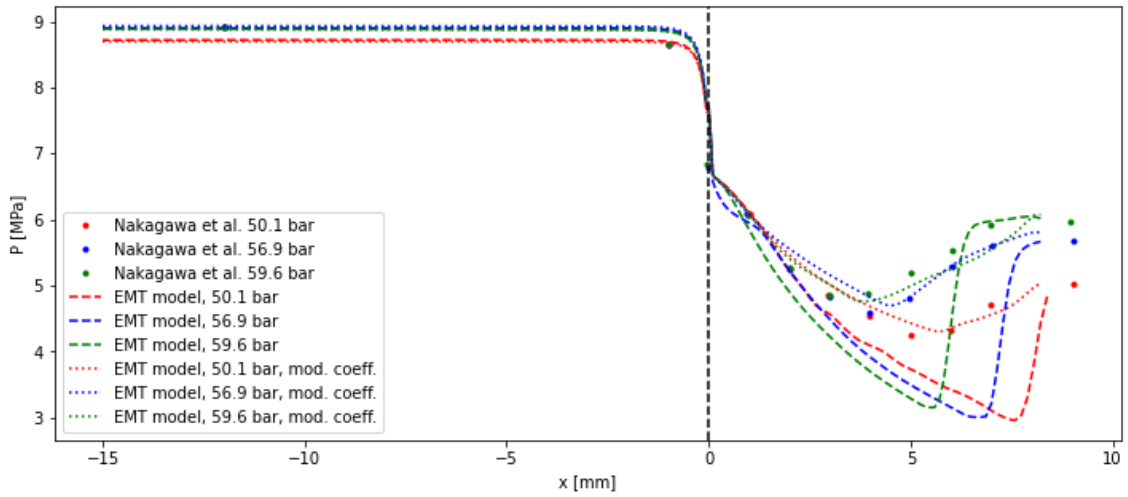

Figure 4.15: Modified coefficients for evaporation and condensation for the same exit pressure.

4.3.3 Two-dimensional

Next to the one-dimensional simulations of the EMT model, also two-dimensional simulations have been performed. However, only few calculations were possible due to time restrictions. Hence, not all simulations that were performed in 1D are reproduced in 2D. Only the nozzle with the supersonic exit is investigated with the wider divergent angle (Nozzle 3 in Table 4.1). Since the larger part of the simulations is thus still performed in the 1D EMT model, the emphasis will still be placed at the 1D results in this report.

All model specifications are held the same for the 2D EMT model, except for using a 2D mesh. Hence, flow variables will now also vary along the radial component. For the 1D mesh, it was not possible to apply a no-slip boundary condition at the wall. However, this is applied for the 2D mesh. Accordingly, proper wall treatment must take place. This has been performed with the k-ε model with enhanced wall treatment enabled.

In Figure 4.16, the results of the previous models are visible together with the new 2D EMT simulation. As where before pressure distribution along the the radial component was constant, the pressure date at the axis is shown for the 2D EMT model. Although similar behaviour is visible, a more steep depressurisation is observed in the first parts of the diverging section. Since mass flow is conserved and lower velocities are observed near the wall, higher velocities are expected at the axis. Hence, lower static pressures are likely at this section.

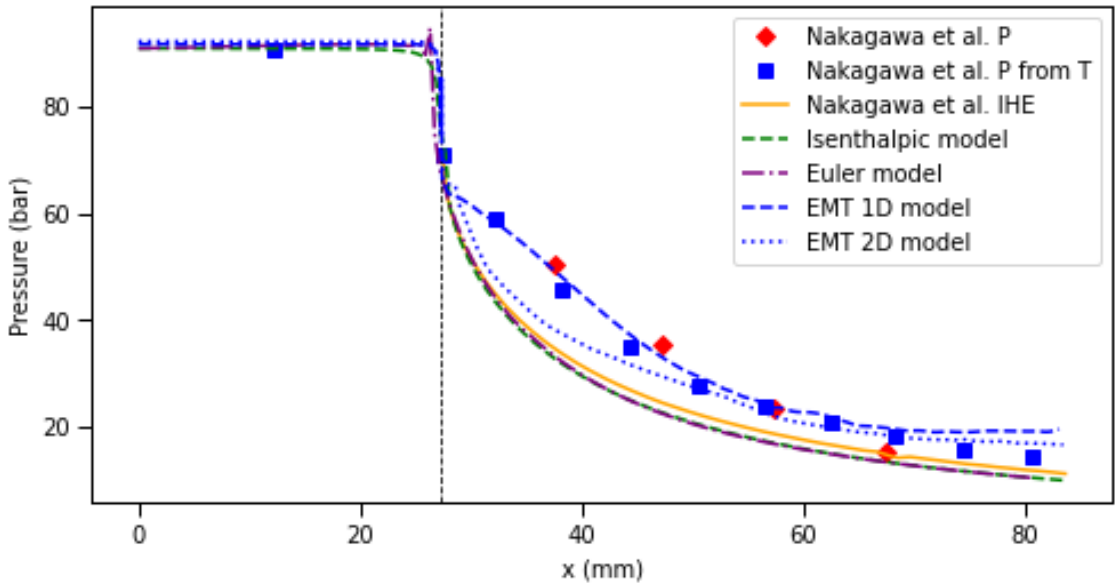

Figure 4.16: Simulation results of all the different models including the 2D EMT model depicted in dotted blue line

4.4 Thermodynamic behaviour

Till now, the focus of the results has mainly been on the pressure distribution throughout the nozzles. This emphasis was deliberately chosen because the experimental data available by the reference papers included only pressure data. With all three models compared to this data, there is a clear image of the similarity of these models with the experimental data. To apply the knowledge of CO_2 flow through nozzles to valves, more insight into the thermodynamic behaviour is necessary. Hence, more than just the pressure distribution is needed to know.

In Chapter 1, the challenges of the transportation of CO_2 in valves were explained. Since phase changes occur, a large temperature drop is expected as well. This could introduce complications to the infrastructure as the material of the walls could become brittle. Also, the mass flow could be influenced by the phase change. Hence, the flow distribution and the thermodynamic characteristics are, next to the pressure distribution, critical to know.

4.4.1 Phase distribution

The phase distribution in the flow is of interest to examine when vapour bubbles are expected. When this happens before the throat, the mass flow could be drastically decreased. If this process initiates after the throat, this property is influenced to a smaller extent. In the event of a shock wave, most of these bubbles will probably collapse as the pressure increases. Therefore, the critical point of this simulation is

the onset of evaporation.

Although this onset of evaporation is of urgent importance, it is simultaneously rather hard to determine. As was explained in 2.4, the bubble nucleation process is heavily related to non-equilibrium effects. Boiling delay effects are often empirically defined and hard to properly implement in CFD codes.

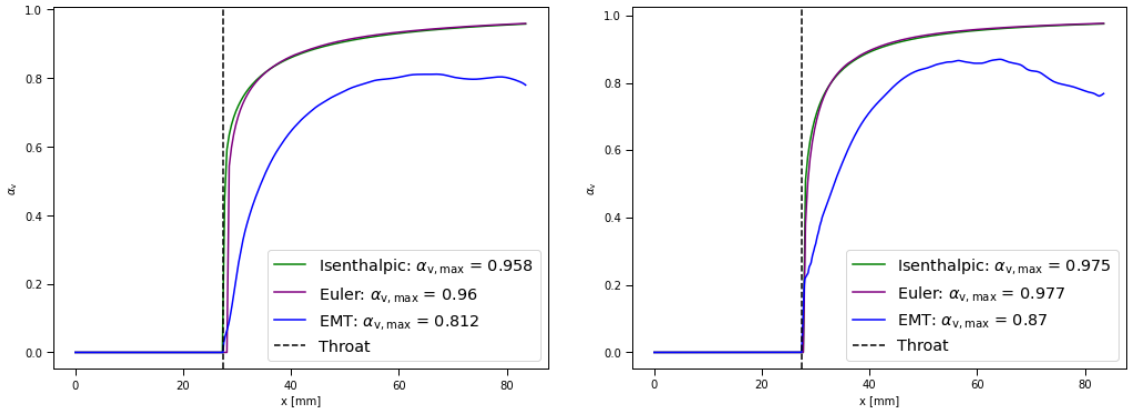

(a) Nozzle 2, supersonic exit

(b) Nozzle 3, supersonic exit

Figure 4.17: Vapour holdup distribution along the nozzle for the two supersonic nozzles. The curves are shown for all the three models.

The vapour holdup fraction of the CO_2 has been plotted in Figure 4.17 for nozzles with the supersonic outflow. The three different models have their own curves in the same colours as presented in earlier graphs. Both the wide and the narrow nozzle are shown next to each other.

The onset of evaporation is very similar for the different models. No evaporation occurs in the converging part of the nozzle and it only starts at the throat. This inherently means for the isenthalpic and Euler models that the phase line is not crossed before the throat. This is not necessarily the case for the EMT model, as this is a model where a real mass transfer model is built with delay effects.

The effect of this built-in mass transfer model is easily visible. The holdup fraction of this model deviates substantially from the other two models where evaporation happens much faster. The delay is built in by means of the coefficients that were discussed in Section 3.2.5 and its effect shown in Section 4.3.2. Therefore, it is possible that the phase line already was crossed in the converging part, but the delay caused the fluid to evaporate at a later stage.

For nozzle 3, a sudden jump is noticed at the throat for the vapour holdup. The effect of the wider nozzle could explain this more instantaneous vaporisation, but this cannot be stated with complete certainty. Also, a decrease in vapour holdup is noticed near the end of the nozzle. This is the point in Figure 4.13 where the pressure starts to stabilise and is not decreasing anymore. Therefore, some vapour already starts to condensate again.

The onset of vaporisation is also interesting to examine with the 2D EMT model. Local vaporisation could be detected which was not possible with the 1D model in radial direction. Along with local vapour holdup fraction, the local mass transfer rate can be examined. For the latter, it is the place where nuclei are formed. Whereas this was difficult to investigate locally in a 1D model, due to a single cell in the radial direction, the 2D model will be able to pinpoint a specific location. Again, this is only examined for the wide nozzle with supersonic outflow.

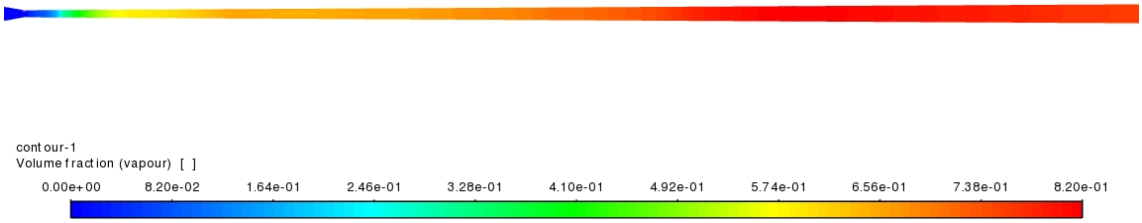

(a) Vapour holdup fraction

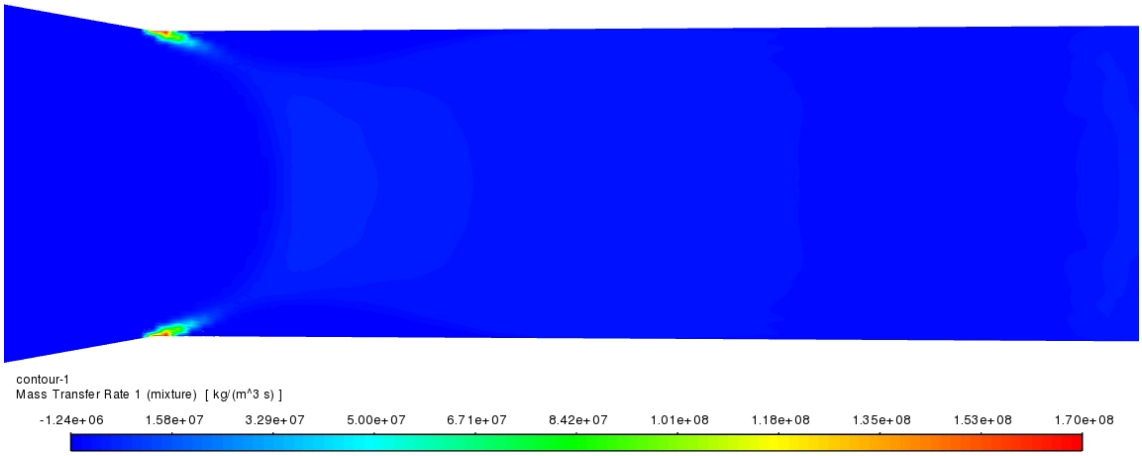

(b) Mass transfer rate at the throat in kg/(m^3 s)

Figure 4.18: Phase distribution of the 2D EMT model

In the upper contour plot of Figure 4.18, only a small part of the converging section is shown since no vapour is present there. It is also clear that the vast amount of vaporisation occurs after the throat and similar behaviour is shown as the one-dimensional results (Figure 4.17). However, from the mass transfer rate, it is shown that these bubbles are formed at the wall near the throat. Also, in the

beginning, the 2D results showed that the vapour formation is stronger at the axis but quickly moved forward as a front.

4.4.2 Sonic behaviour

The velocity of the fluid in the nozzle is interesting to examine whether the choked condition is true. This implies that at the throat $M = 1$ is obtained. The speed of sound is inextricably linked to this property as $M = u/c$. As already extensively discussed, this property is not trivial in two-phase flows and hence the choked condition is not always legitimate.

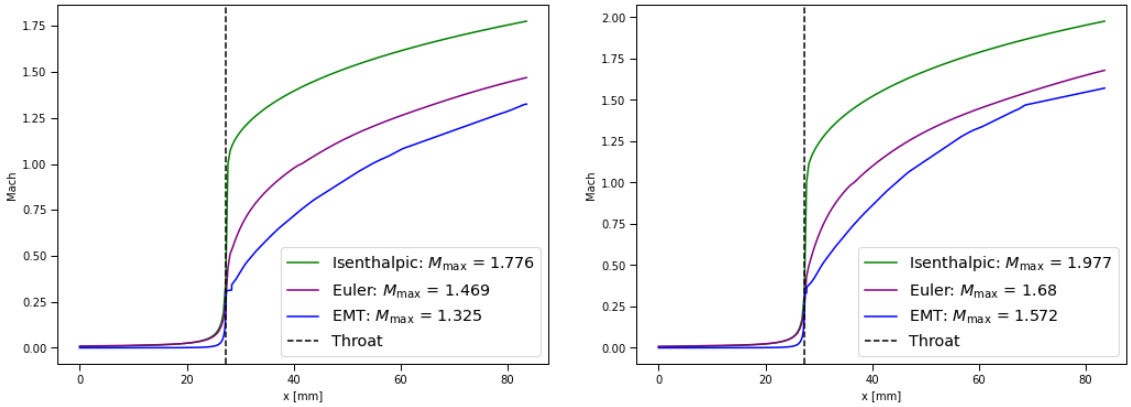

(a) Nozzle 2, supersonic exit

(b) Nozzle 3, supersonic exit

Figure 4.19: Mach distribution along the nozzle for the two supersonic nozzles. The curves are shown for all the three models.

In Figure 4.19, the Mach distribution for the two nozzles with supersonic outflow is shown for all three models. Large deviations between the models can be noticed and also the Mach value at the throat is not equal. Between the two nozzles, it is clear that a higher Mach is obtained for the wider nozzle. This is also expected since the pressure decreased to a much lower value as could be seen in Figure 4.13.

The isenthalpic model is the only model that shows the choked condition at the throat. For the Euler and EMT model, $M = 1$ is reached much later in the nozzle. It is expected of course that the isenthalpic model reaches this value at the throat since this model is based on that assumption (see Section 2.3). This assumption is not imposed on the Euler model and the EMT model.

The mixture speed of sound formulation for the EMT model is based on the pressure equilibrium and uses Equation 2.34. This can not be changed in the software and other formulations must be used in post-processing operations. The isenthalpic model uses instead the full equilibrium formulation.

4.4.3 Joule-Thomson cooling

As noted before, the Joule-Thomson effect is rather strong for CO_2 in gas and two-phase states. It can experience 1 $°C$/bar, which possibly leads to very low temperatures. Since this can influence the wall material, it is important to examine this effect.

The impact of the Joule-Thomson effect is interesting to examine but physically hard to grasp what it actually represents. Of course, the change in temperature with a certain change in pressure, but only with constant enthalpy. By simulating the flow with the different models, it became apparent that not all models make this assumption. To investigate this Joule-Thomson effect for those models, a more extensive calculation is needed. Of course, a simplification can be made $\mu_{\mathrm{JT}} = \Delta T/\Delta P$, but this may not be very accurate. By making use of the cyclic rule, a useful relation is obtained in which this coefficient can be examined:

$$\left(\frac{\partial T}{\partial P}\right)_H \left(\frac{\partial H}{\partial T}\right)_P \left(\frac{\partial P}{\partial H}\right)_T = -1 \tag{4.1}$$

where the first term of Equation 4.1 represents the Joule-Thomson coefficient μ_{JT} which is desired. The second term is the specific heat at constant pressure, C_p and the final term represents the inverse of the so-called isothermal Joule-Thomson coefficient μ_{T}. Since both these terms are already provided to Fluent in the Look-up Tables (Table 3.5), it is easy to calculate the Joule-Thomson coefficient, using the following relation:

$$\mu_{\mathrm{JT}} = -\frac{\left(\frac{\partial H}{\partial P}\right)_T}{\left(\frac{\partial H}{\partial T}\right)_P} = -\frac{\mu_{\mathrm{T}}}{C_p}. \tag{4.2}$$

However, both these terms on the right-hand side in Equation 4.2 are not defined in the two-phase area. By making use of the same mixing rules as in Equation 2.22, the mixture properties were defined using the mass fraction. The results of this implementation can be seen in Figure 4.20 for both experiments.

It was already clear in the introduction that only positive μ_{JT} values are possible for CO_2 as shown in Figure 2.2. Looking at the results in Figure 4.20, this is also the case. The highest values are obtained with the highest vapour fractions. This is evidently indicated by the results of the shock experiments. A clear drawback in the Joule-Thomson coefficient is noticed, indicating the shock.

Also, it is noted that during depressurisation, the nozzles follow the same path to their maximum value, regardless of the divergent angle or exit pressure. With this in mind, temperature drops can be easily approximated with a known pressure drop and vice versa. This is also expected since pressure and temperature are strongly linked at the saturation line. Hence, a depressurisation along the phase line is expected.

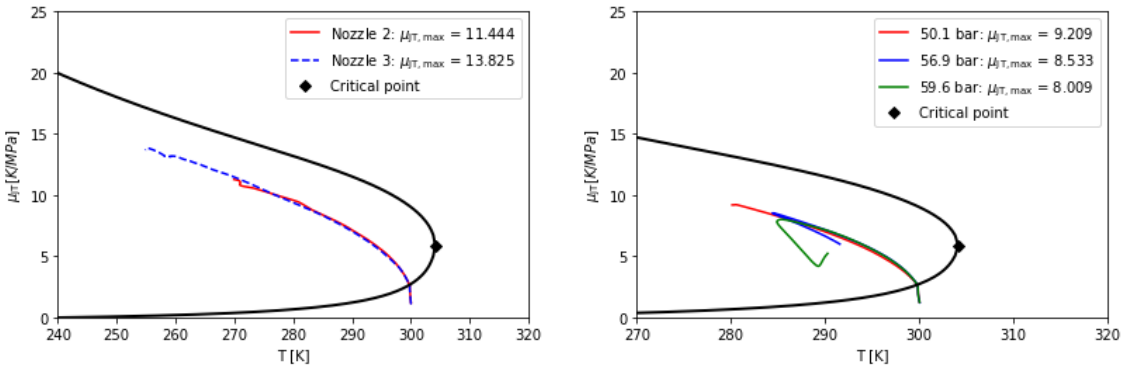

(a) Supersonic exit nozzles (b) Shock nozzles

Figure 4.20: Joule-Thomson coefficient (μ_{JT}) plotted versus the temperature. On the left, the supersonic nozzles. On the right, the nozzles with the presence of the shocks.

The $p-T$ diagrams of the Fluent simulations are shown below in Figure 4.21. Clearly, the depressurisation curves follow the saturation line as expected.

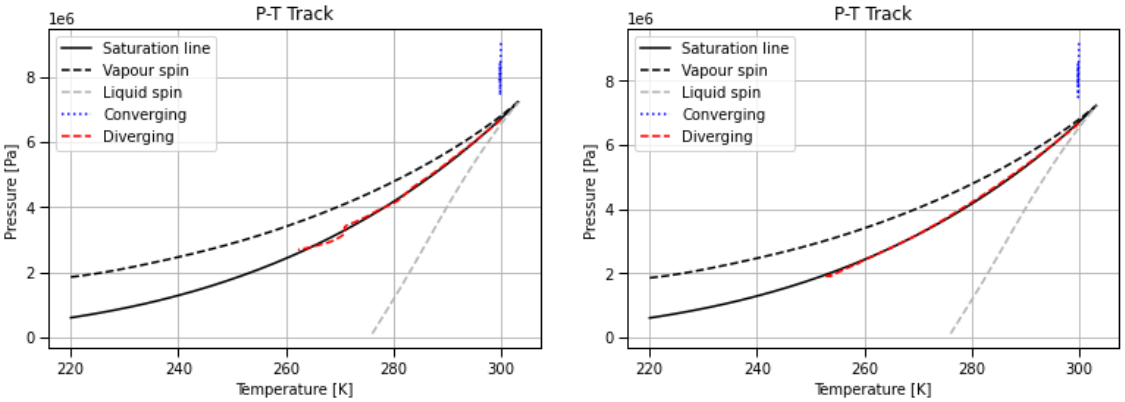

(a) Nozzle 2 (b) Nozzle 3

Figure 4.21: $p-T$ diagrams with depressurisation curves of the simulations. The expansions follow the saturation line.

Chapter 5

Conclusions

During CCS operations, a valve is used to control mass flow and maintain pressure control. However, choked flow can occur when pressure is reduced in this control component. This depressurisation can possibly generate a phase transition. When this happens, it causes a temperature drop in the fluid, since p and T are linked at the phase line. The effect of this decrease in temperature causes the material of the pipe or the valve to become brittle and coatings to lose their functionality. Obviously, this creates a problem for the CCS operations because it could lead to increased wear. Therefore, the following research question was formulated:

"How is the behaviour of a CO_2 flow influenced by passing through a control valve and what are the consequences for the CCS operations?"

This was done by replicating this flow in three different numerical codes. However, since experimental work with experimental data of CO_2 flow through valves is very limited, a different approach was chosen to mimic the same possible effects. Experimental work performed by Nakagawa et al. [1] [2] was taken as a reference case in which CO_2 flow was examined through nozzles. The validity of the conclusions drawn from the results of the nozzle will be discussed here.

This research is performed in several steps using these three different numerical codes in increasing complexity. The most simple model, the isenthalpic model, is able to model depressurisation with mass transfer modelled by the HEM. However, when shocks are present, this model is no longer valid and the Euler model with the shock capturing scheme is used with the same mass transfer mechanism. To model non-equilibrium effects, an actual mass transfer model is incorporated in the last model: the Enhanced Mass Transfer model (EMT). This model, in contrast to the other two codes written in Python, is built in Fluent.

In conclusion, the flow behaviour of the CO_2 flow is significantly influenced by passing through a nozzle. Large pressure drops create evaporation with significant vapour fractions as a result. The flow will choke because of this increasing vapour fraction, and maximum mass flow is determined. Also, large temperature drops

must be expected. These effects will also be the case for a valve. However, the extent of every aspect of these effects stays partially undecided.

Shock waves were examined since these are possible events to occur after the control valve. The Euler model was able to capture these shocks. However, sharp and thin shock waves were obtained, and only the EMT model with the built-in cavitation mass transfer could replicate the experimentally observed thick shock waves. Also, delayed mass transfer was accomplished in the EMT model. Slower condensation was desired than the prescribed default values of the cavitation model showed. Hence, by lowering this coefficient, it improved the resemblance of the model to reality.

A choked flow is expected at the throat of the valve. This was also the case for the simulations. Whereas the isenthalpic model choked at the throat, $M = 1$ was obtained only after the throat for the EMT model. Only then substantial vaporisation occurred and the mixture sound speed matched the mixture velocity. As simulations showed, this moment could be delayed to even 30mm after the throat. This has a substantial influence on the mass flow since this is the point where the critical mass flow rate is determined. The impact of the formulation of the speed of sound in the mixture could be significant, as this remains a long-standing challenge.

At the choked condition, a substantial amount of vapour was present in the fluid, especially in the case of the isenthalpic and Euler solver. The sudden evaporation of the HEM can explain this elevation right after the throat. The EMT model includes an actual mass transfer mechanism and is expected to be closer to reality. Moreover, delayed mass transfer was applied to correspond better to the experiments. This is probably also the case for valves, where evaporation takes time. Furthermore, no evaporation was noticed before the throat. This would mean, together with the choked condition after the throat, that the mass flow downstream should not be significantly decreased due to the formation of the vapour phase.

A temperature drop due to a pressure drop was investigated by examining the Joule-Thomson coefficient. The hypothesis in the introduction that a significant temperature reduction would occur could be confirmed. Considerably low temperatures were observed during depressurisation. This effect increased with developing vapour holdup fractions. Hence, in combination with the extensive generation of vapour, low temperatures can be expected after the throat. However, the stagnation temperature at the inlet could be decisive. Although the temperatures simulated in these nozzles fall within the range of possible inlet temperatures of CO_2, no higher temperatures could be simulated due to a flaw in the model.

Before expressing the expected consequences of this behaviour on the CCS operations, the overall simplification of a valve employing a nozzle must be discussed. The nozzles tested in these simulations had smooth geometries where a clear throat was present. However, this will not be so straightforward in the case of a genuine valve. The geometries of valves often do not have smooth transitions, and the narrowing to the throat or the expansion behind could be much more sudden and sharp.

This will undoubtedly affect the phase distribution and sonic behaviour around the throat.

The consequences of the affected behaviour of the CO_2 flow for the CCS operations must not be overlooked. Since the vapour generation is expected to happen after the throat, the mass flow will not be extensively reduced. Therefore, this will be of less concern. However, large temperature drops are expected. This must be taken into account since this can influence the material of the pipe. Also, the amount of vapour formed after the throat will have a large effect on the hydrostatic pressure gradient in the well downstream.

It must be noted that the effects are interdependent. Smaller vapour fractions will lead to smaller pressure and temperature drops. Also, the moment of choking could change, and the onset of evaporation too. This study must be seen as a preliminary investigation in which the possible effects were examined. In general, drawing firm conclusions from CO_2 flow passing through a nozzle for the impact of CO_2 flow through control valves is ambiguous. Experiments must be performed with high-pressure CO_2 flow through actual valves. With these experiments, simulations could be accomplished to validate and predict other conditions.

Chapter 6

Recommendations

This research was a first step towards 3D simulations of actual valves. Based on this work, there are some recommendations to consider. Firstly, possible improvements of the current work are emphasised. Also, some possibilities are highlighted that could lead to improvements if new features are introduced in future software releases. Finally, suggestions for future work will be given.

The handling of the thermodynamic properties was carried out using look-up tables created with REFPROP. As it turned out, thermodynamic inputs in the vicinity of the critical point resulted in problematic outcomes. As pointed out in Chapter 4, the gradients in thermodynamic properties could be excessive. Although this error can also be partially attributed to REFPROP, which is not accurate in this region, improved Look-up Tables could have resulted in converging solutions.

Improved tables do not just mean making the grid of the table finer and reducing the ΔP and ΔT. Although this procedure was tried, the solver still diverged. Other interpolation techniques (as opposed to bi-linear) could be a solution, where in the vicinity of critical regions of the table, smooth transitions are guaranteed. Also, another possibility would be in the field of AI: neural networks could help by learning the dictionaries and recognising critical areas. This would still make it possible to do proper calculations for large gradients without sacrificing CPU time, which would be the case with an ever finer grid.

Also, improvements with respect to the mesh could have been made. Although simulations in 1D were performed, more attention could have been paid to the localisation of unstable regions. A finer mesh was already applied near the throat (as seen in Chapter 3), but the shock waves were not considered in this treatment. Since large gradients are observed in flow quantities, mesh adaptation at the expected location of this shock wave could have improved the simulations. Dynamic mesh refinement could serve as a solution in this case.

Subsequently, improvements are achievable regarding the mass transfer mechanisms. As already pointed out in Section 2.4, surface tension is neglected in all cavitation models. However, in Chapter 1, the low surface tension of CO_2 was highlighted. Because of this property, more and smaller vapour bubbles are expected.

Unfortunately, it was impossible to test this hypothesis because of the simplifications made in the cavitation models. If it is desired to consider this, a mass transfer UDF will offer a possible solution in which the mass transfer mechanism must be defined entirely manually.

If future releases of Fluent enable more extensive multiphase flow simulations, there are several exciting things to consider. Currently, Fluent allows one phase to be fully defined by using 11 Look-up Tables. The other phase cannot be defined as precisely and only 5 tables can be used. As discussed before, this leads to decreased accuracy of the simulations. With the possibility of two fully defined phases, this cutback could be avoided. Secondly, if Eulerian-Lagrangian models were possible for materials other than H_2O, completely different simulations could be performed where the vapour phase would be treated as single particles. As noted before, this would only be valid for simulations with low vapour volume fractions.

Finally, as suggestions for future work, there are some considerations. Implementation of the HEM inside Fluent could be interesting. This could be achieved by simulating single-phase flow and using a UDRGM based on $p-\rho$ tables where the two-phase area is covered. No actual mass transfer models can be implemented this way, but faster convergence should be achieved with moderate accuracy. On the contrary, a full two-fluid model can be considered. This Eulerian-Eulerian method will solve two separate continuity, momentum and energy equations. A high degree of accuracy should be achievable, but convergence is more difficult and time-consuming.

Furthermore, the simulations of actual valves would be appealing. This will require more emphasis on mesh and local phenomena given the more complex geometry. However, without experiments to validate the model, this still seems ambitious. If these results of experiments are available for high-pressure CO_2 flow, 2D and finally 3D simulations could be conducted eventually and validated against experimental data.

Bibliography

[1] M. Nakagawa, M. S. Serrano, A. Harada, and M. Serrano Berana, "Shock Waves in Supersonic Two-Phase Flow of CO2 in Converging-Diverging Nozzles Shock Waves in Supersonic Two-Phase Flow of CO 2 in Converging-Diverging Nozzlesph (on study leave)," Tech. Rep., 2008. [Online]. Available: http://docs.lib.purdue.edu/iracc/926.

[2] M. Nakagawa, M. S. Berana, and A. Kishine, "Supersonic two-phase flow of CO2 through converging–diverging nozzles for the ejector refrigeration cycle," *International Journal of Refrigeration*, vol. 32, no. 6, pp. 1195–1202, Sep. 2009, ISSN: 0140-7007. DOI: 10.1016/J.IJREFRIG.2009.01.015.

[3] O. Portner H, D. Roverts, E. Poloczanska, *et al.*, "IPCC, 2022: Summary for Policymakers," in *Climate Change 2022: Impacts, Adaptation, and Vulnerability.Contribution of Working Group II to the Sixth Assessment Report of the Intergovernmental Panel on Climate Change*, Cambridge University Press, 2022, ISBN: 9789291691593. [Online]. Available: www.ipcc.ch.

[4] B. Metz, O. Davidson, H. de Conink, M. Loos, and L. Meyer, "IPCC Special Report on Carbon Dioxide Capture and Storage. Prepared by Working Group III of he Intergovernmental Panel Climate Change," Cambridge University Press, Cambridge, Tech. Rep., 2005, pp. -442.

[5] "GLOBAL STATUS OF CCS 2020," Tech. Rep.

[6] *Porthos - Project*, Mar. 2022. [Online]. Available: https://www.porthosco2.nl/project/.

[7] P. Friedlingstein, M. W. Jones, M. O'Sullivan, *et al.*, "Global Carbon Budget 2021," *Earth System Science Data Discussions*, vol. 2021, pp. 1–191, 2021. DOI: 10.5194/essd-2021-386. [Online]. Available: https://essd.copernicus.org/preprints/essd-2021-386/.

[8] V. E. Onyebuchi, A. Kolios, D. P. Hanak, C. Biliyok, and V. Manovic, "A systematic review of key challenges of CO2 transport via pipelines," *Renewable and Sustainable Energy Reviews*, vol. 81, pp. 2563–2583, Jan. 2018, ISSN: 1364-0321. DOI: 10.1016/J.RSER.2017.06.064.

[9] Munkejord S.T., Bernstone C., Clausen S., d. G. Koeijer, and Molnvik M., "Combining thermodynamic and fluid flow modelling for CO2 flow assurance," *Energy Procedia*, vol. 37, pp. 2904–2913, 2013.

[10] G. de Koeijer, J. H. Borch, M. Drescher, H. Li, O. Wilhelmsen, and J. Jakobsen, "CO2 Transport – Depressurization, Heat Transfer and Impurities," *Energy Procedia*, vol. 4, pp. 3008–3015, 2011.

[11] L. Klinkby, C. M. Nielsen, E. Krogh, I. E. Smith, B. Palm, and C. Bernstone, "Simulating rapidly fluctuating CO2 flow into the Vedsted CO2 pipeline, injection well and reservoir," *Energy Procedia*, vol. 4, pp. 4291–4298, Jan. 2011, ISSN: 1876-6102. DOI: 10.1016/J.EGYPRO.2011.02.379.

[12] S. T. Munkejord, J. P. Jakobsen, A. Austegard, and M. J. Mølnvik, "Thermo- and fluid-dynamical modelling of two-phase multi-component carbon dioxide mixtures," Tech. Rep., 2008.

[13] C. M. Allison and J. K. Hohorst, "Role of RELAP/SCDAPSIM in nuclear safety," *Science and Technology of Nuclear Installations*, vol. 2010, 2010, ISSN: 16876075. DOI: 10.1155/2010/425658.

[14] K. H. Bendlksen, D. Malnes, R. Moe, and S. Nuland, "The Dynamic Two-Fluid Model OLGA: Theory and Application," *SPE Production Engineering*, vol. 6, no. 02, pp. 171–180, May 1991, ISSN: 0885-9221. DOI: 10.2118/19451-PA. [Online]. Available: https://doi.org/10.2118/19451-PA.

[15] E. Aursand, P. Aursand, M. Hammer, and H. Lund, "The influence of CO2 mixture composition and equations of state on simulations of transient pipeline decompression," *International Journal of Greenhouse Gas Control*, vol. 54, pp. 599–609, Nov. 2016, ISSN: 17505836. DOI: 10.1016/j.ijggc.2016.07.004.

[16] E. W. Lemmon, I. H. Bell, M. L. Huber, and M. O. McLinden, *NIST Standard Reference Database 23: Reference Fluid Thermodynamic and Transport Properties-REFPROP, Version 10.0, National Institute of Standards and Technology*, 2018.

[17] Z. X. Zhang, G. X. Wang, P. Massarotto, and V. Rudolph, "Optimization of pipeline transport for CO2 sequestration," *Energy Conversion and Management*, vol. 47, no. 6, pp. 702–715, Apr. 2006, ISSN: 0196-8904. DOI: 10.1016/J.ENCONMAN.2005.06.001.

[18] P. Aursand, M. Hammer, S. T. Munkejord, and Ø. Wilhelmsen, "Pipeline transport of CO 2 mixtures: Models for transient simulation," Tech. Rep., 2013.

[19] F. M. White, *Fluid Dynamics*, 7th. 2011.

[20] T. Flåtten and H. Lund, "Relaxation two-phase flow models and the subcharacteristic condition," *Mathematical Models and Methods in Applied Sciences*, vol. 21, no. 12, pp. 2379–2407, Dec. 2011, ISSN: 02182025. DOI: 10.1142/S0218202511005775.

[21] S. Clausen and S. T. Munkejord, "Depressurization of CO2 - A numerical benchmark study," in *Energy Procedia*, vol. 23, Elsevier Ltd, 2012, pp. 266–273. DOI: 10.1016/j.egypro.2012.06.021.

[22] A. Morin, P. K. Aursand, T. Flåtten, and S. T. Munkejord, "Numerical Resolution of CO 2 Transport Dynamics," SIAM Conference on Mathematics forIndustry: Challenges and Frontiers, San Francisco, Tech. Rep., Oct. 2009. [Online]. Available: https://epubs.siam.org/terms-privacy.

[23] K. Bartels and A. Harmon, *Choked Flow in Control Valves*, Mar. 2022. [Online]. Available: https://www.isa.org/intech-home/2021/august-2021/departments/choked-flow-in-control-valves.

[24] Y. Liao and D. Lucas, "Computational modelling of flash boiling flows: A literature survey," *International Journal of Heat and Mass Transfer*, vol. 111, pp. 246–265, Aug. 2017, ISSN: 0017-9310. DOI: 10.1016/J.IJHEATMASSTRANSFER.2017.03.121.

[25] J. R. Travis, D. Piccioni Koch, and W. Breitung, "A homogeneous non-equilibrium two-phase critical flow model," *International Journal of Hydrogen Energy*, vol. 37, no. 22, pp. 17 373–17 379, Nov. 2012, ISSN: 0360-3199. DOI: 10.1016/J.IJHYDENE.2012.07.077.

[26] K. Banasiak and A. Hafner, "1D Computational model of a two-phase R744 ejector for expansion work recovery," *International Journal of Thermal Sciences*, vol. 50, no. 11, pp. 2235–2247, Nov. 2011, ISSN: 1290-0729. DOI: 10.1016/J.IJTHERMALSCI.2011.06.007.

[27] W. Angielczyk, Y. Bartosiewicz, D. Butrymowicz, *et al.*, "1-D Modeling Of Supersonic Carbon DioxideTwo-Phase Flow Through Ejector Motive Nozzle," Tech. Rep., 2010. [Online]. Available: http://docs.lib.purdue.edu/iracc/1102.

[28] M. Yazdani, A. A. Alahyari, and T. D. Radcliff, "Numerical modeling and validation of supersonic two-phase flow of CO 2 in converging-diverging nozzles," *Journal of Fluids Engineering, Transactions of the ASME*, vol. 136, no. 1, 2014, ISSN: 00982202. DOI: 10.1115/1.4025647.

[29] F. Giacomelli, F. Mazzelli, and A. Milazzo, "A novel CFD approach for the computation of R744 flashing nozzles in compressible and metastable conditions," *Energy*, vol. 162, pp. 1092–1105, Nov. 2018, ISSN: 0360-5442. DOI: 10.1016/J.ENERGY.2018.08.050.

[30] M. J. Moran, H. N. Shapiro, D. D. Boettner, and M. B. Bailey, *Fundamentals of engineering thermodynamics*. John Wiley & Sons, 2010, ISBN: 0470495901.

[31] Q. Dang Le, R. Mereu, G. Besagni, V. Dossena, and F. Inzoli, "Computational Fluid Dynamics Modeling of Flashing Flow in Convergent-Divergent Nozzle," *Journal of Fluids Engineering, Transactions of the ASME*, vol. 140, no. 10, Oct. 2018, ISSN: 1528901X. DOI: 10.1115/1.4039908.

[32] X. Xi, H. Liu, M. Jia, M. Xie, and H. Yin, "A new flash boiling model for single droplet," *International Journal of Heat and Mass Transfer*, vol. 107, pp. 1129–1137, 2017, ISSN: 0017-9310.

[33] O. Miyatake, I. Tanaka, and N. Lior, "A simple universal equation for bubble growth in pure liquids and binary solutions with a nonvolatile solute," *International journal of heat and mass transfer*, vol. 40, no. 7, pp. 1577–1584, 1997, ISSN: 0017-9310.

[34] R. Barbone, D. L. Frost, A. Makris, and J. Nerenberg, "Explosive boiling of a depressurized volatile liquid," in *IUTAM Symposium on Waves in Liquid/Gas and Liquid/Vapour Two-Phase Systems*, Springer, 1995, pp. 315–324.

[35] E. Sher, T. Bar-Kohany, and A. Rashkovan, "Flash-boiling atomization," *Progress in energy and combustion science*, vol. 34, no. 4, pp. 417–439, 2008, ISSN: 0360-1285.

[36] J. E. McDonald, "Homogeneous nucleation of vapor condensation. I. Thermodynamic aspects," *American Journal of Physics*, vol. 30, no. 12, pp. 870–877, 1962, ISSN: 0002-9505.

[37] C. Lettieri, D. Paxson, Z. Spakovszky, and P. Bryanston-Cross, "Characterization of Nonequilibrium Condensation of Supercritical Carbon Dioxide in a de Laval Nozzle," *Journal of Engineering for Gas Turbines and Power*, vol. 140, no. 4, Apr. 2018, ISSN: 15288919. DOI: 10.1115/1.4038082.

[38] C. E. Brennen, *Cavitation and bubble dynamics*. Cambridge university press, 2014, ISBN: 1107644763.

[39] G. H. Schnerr and J. Sauer, "Physical and Numerical Modeling of Unsteady Cavitation Dynamics," Tech. Rep., 2001. [Online]. Available: https://www.researchgate.net/publication/296196752.

[40] A. K. Singhal, M. M. Athavale, H. Li, and Y. Jiang, "Mathematical basis and validation of the full cavitation model," *J. Fluids Eng.*, vol. 124, no. 3, pp. 617–624, 2002, ISSN: 0098-2202.

[41] P. Zwart, T. Belamri, P. J. Zwart, and A. G. Gerber, "A two-phase flow model for predicting cavitation dynamics Optimization of HVAC design systems inside incubators View project CFD design and analysis of a displacement ventilation system inside an university lecture room View project A Two-Phase Flow Model for Predicting Cavitation Dynamics," Tech. Rep., 2004. [Online]. Available: https://www.researchgate.net/publication/306205415.

[42] "ANSYS Fluent User's Guide," Tech. Rep., 2021. [Online]. Available: http://www.ansys.com.

[43] Y. Fang, S. Poncet, Y. Bartosiewicz, M. Duponcheel, H. Nesreddine Hydro-Québec, and C. Michal Palacz, "ADVANCED NUMERICAL SIMULATIONS OF TWO-PHASE CO 2 EJECTORS," Tech. Rep., 2019.

[44] Y. Fang, M. De Lorenzo, P. Lafon, S. Poncet, and Y. Bartosiewicz, "An Accurate and Efficient Look-up Table Equation of State for Two-Phase Compressible Flow Simulations of Carbon Dioxide," *Industrial and Engineering Chemistry Research*, vol. 57, no. 22, pp. 7676–7691, Jun. 2018, ISSN: 15205045. DOI: 10.1021/acs.iecr.8b00507.

[45] P. J. Linstrom and W. G. Mallard, "The NIST Chemistry WebBook: A chemical data resource on the internet," *Journal of Chemical & Engineering Data*, vol. 46, no. 5, pp. 1059–1063, 2001, ISSN: 0021-9568.

[46] R. Span and W. Wagner, "A New Equation of State for Carbon Dioxide Covering the Fluid Region from the Triple-Point Temperature to 1100 K at Pressures up to 800 MPA," *Lehrstuhl für THermodynamik*, vol. 25, pp. 1513–1558, 1996.

[47] K. Erik, T. Giljarhus, S. Tollak Munkejord, and G. Skaugen, "Solution of the Span-Wagner equation of state using a density-energy state function for fluid-dynamic simulation of carbon dioxide," Tech. Rep., 2011.

[48] A. M. Log, S. T. Munkejord, and M. Hammer, "HLLC-type methods for compressible two-phase flow in ducts with discontinuous area changes," *Computers & Fluids*, vol. 227, p. 105 023, Sep. 2021, ISSN: 0045-7930. DOI: 10.1016/J.COMPFLUID.2021.105023.

[49] E. F. Toro, *Riemann solvers and numerical methods for fluid dynamics : a practical introduction*. Springer, 2006, p. 680, ISBN: 9783540252023.

[50] M. S. Liou and C. J. Steffen, "A New Flux Splitting Scheme," *Journal of Computational Physics*, vol. 107, no. 1, pp. 23–39, Jul. 1993, ISSN: 0021-9991. DOI: 10.1006/JCPH.1993.1122.

[51] S. Brown, S. Martynov, and H. Mahgerefteh, "Simulation of two-phase flow through ducts with discontinuous cross-section," *Computers & Fluids*, vol. 120, pp. 46–56, Oct. 2015, ISSN: 0045-7930. DOI: 10.1016/J.COMPFLUID.2015.07.018.

[52] G. Arnulfo, C. Bertani, and M. De Salve, "Prediction of two-phase choked-flow through safety valves," in *Journal of Physics: Conference Series*, vol. 501, Institute of Physics Publishing, 2014. DOI: 10.1088/1742-6596/501/1/012016.

[53] Y. Hou, C. Liu, J. Ma, J. Cao, and S. Chen, "Mass flowrate characteristics of supercritical CO2 flowing through an electronic expansion valve," *International Journal of Refrigeration*, vol. 47, pp. 134–140, Nov. 2014, ISSN: 0140-7007. DOI: 10.1016/J.IJREFRIG.2014.04.008.

[54] Y. Fang, S. Poncet, H. Nesreddine, and Y. Bartosiewicz, "An open-source density-based solver for two-phase CO2 compressible flows: Verification and validation," *International Journal of Refrigeration*, vol. 106, pp. 526–538, Oct. 2019, ISSN: 0140-7007. DOI: 10.1016/J.IJREFRIG.2019.05.016.

[55] K. Banasiak and A. Hafner, "Mathematical modelling of supersonic two-phase R744 flows through converging–diverging nozzles: The effects of phase transition models," *Applied Thermal Engineering*, vol. 51, no. 1-2, pp. 635–643, Mar. 2013, ISSN: 1359-4311. DOI: 10.1016/J.APPLTHERMALENG.2012.10.005.

[56] R. Hołyst and A. Poniewierski, *Thermodynamics for chemists, physicists and engineers*. Springer, 2012, vol. 344.

[57] M. S. Berana, M. Nakagawa, and A. Harada, "Shock waves in supersonic two-phase flow of CO2 in Converging-Diverging Nozzles," *HVAC and R Research*, vol. 15, no. 6, pp. 1081–1098, 2009, ISSN: 10789669. DOI: 10.1080/10789669.2009.10390880.

[58] S. K. Raman and H. D. Kim, "Solutions of supercritical CO2 flow through a convergent-divergent nozzle with real gas effects," *International Journal of Heat and Mass Transfer*, vol. 116, pp. 127–135, Jan. 2018, ISSN: 0017-9310. DOI: 10.1016/J.IJHEATMASSTRANSFER.2017.09.019.

[59] R. E. Henry and H. K. Fauske, "The two-phase critical flow of one-component mixtures in nozzles, orifices, and short tubes," 1971, ISSN: 0022-1481.

[60] Mahgerefteh H, Brown S, and Martynov S, *A study of the effects of friction, heat transfer, and stream impurities on the decompression behavior in CO2pipelines*, 2012. DOI: 10.1002/ghg.

[61] A. Cosham, D. G. Jones, K. Armstrong, D. Allason, and J. Barnett, "The decompression behaviour of carbon dioxide in the dense phase," in *International Pipeline Conference*, vol. 45141, American Society of Mechanical Engineers, 2012, pp. 447–464, ISBN: 0791845141.

[62] S. T. Munkejord, M. Hammer, and S. W. Løvseth, *CO2 transport: Data and models - A review*, May 2016. DOI: 10.1016/j.apenergy.2016.01.100.

[63] H. E. Jie, B. P. Xu, J. X. Wen, R. Cooper, and J. Barnett, "Predicting the decompression characteristics of carbon dioxide using computational fluid dynamics," in *Proceedings of the Biennial International Pipeline Conference, IPC*, vol. 3, 2012, pp. 585–595, ISBN: 9780791845141. DOI: 10.1115/IPC2012-90649.

[64] S. Brown, S. Martynov, H. Mahgerefteh, and C. Proust, "A homogeneous relaxation flow model for the full bore rupture of dense phase CO2 pipelines," *International Journal of Greenhouse Gas Control*, vol. 17, pp. 349–356, Sep. 2013, ISSN: 17505836. DOI: 10.1016/j.ijggc.2013.05.020.

[65] S. Brown, S. Martynov, H. Mahgerefteh, S. Chen, and Y. Zhang, "Modelling the non-equilibrium two-phase flow during depressurisation of CO2 pipelines," *International Journal of Greenhouse Gas Control*, vol. 30, pp. 9–18, Nov. 2014, ISSN: 17505836. DOI: 10.1016/j.ijggc.2014.08.013.

[66] S. T. Munkejord and M. Hammer, "Depressurization of CO2-rich mixtures in pipes: Two-phase flow modelling and comparison with experiments," *International Journal of Greenhouse Gas Control*, vol. 37, pp. 398–411, Jun. 2015, ISSN: 17505836. DOI: 10.1016/j.ijggc.2015.03.029.

[67] H. Lund, "A hierarchy of relaxation models for two-phase flow," *SIAM Journal on Applied Mathematics*, vol. 72, no. 6, pp. 1713–1741, 2012, ISSN: 00361399. DOI: 10.1137/12086368X.

[68] S. T. Munkejord, "Comparison of Roe-type methods for solving the two-fluid model with and without pressure relaxation," *Computers & Fluids*, vol. 36, no. 6, pp. 1061–1080, Jul. 2007, ISSN: 0045-7930. DOI: 10.1016/J.COMPFLUID.2007.01.001.

[69] ——, "A numerical study of two-fluid models with pressure and velocity relaxation," *Advances in Applied Mathematics and Mechanics*, vol. 2, no. 2, pp. 131–159, 2010, ISSN: 20700733. DOI: 10.4208/aamm.09-m0971.

[70] P. J. Martínez Ferrer, T. Flåtten, and S. T. Munkejord, "On the effect of temperature and velocity relaxation in two-phase flow models," *ESAIM: Mathematical Modelling and Numerical Analysis*, vol. 46, no. 2, pp. 411–442, Mar. 2012, ISSN: 0764583X. DOI: 10.1051/m2an/2011039.

[71] G. Linga and T. Flåtten, "A hierarchy of non-equilibrium two-phase flow models," *ESAIM: Proceedings and Surveys*, vol. 66, pp. 109–143, 2019. DOI: 10.1051/proc/201966006.

[72] Lund Halvor and Aursand Peder, "Two-Phase Flow of CO2 with Phase Transfer," *Energy Procedia*, vol. 23, pp. 246–255, 2012.

[73] R. Benintendi, "Non-equilibrium phenomena in carbon dioxide expansion," *Process Safety and Environmental Protection*, vol. 92, no. 1, pp. 47–59, Jan. 2014, ISSN: 0957-5820. DOI: 10.1016/J.PSEP.2013.11.001.

[74] A. Romei and G. Persico, "Computational fluid-dynamic modelling of two-phase compressible flows of carbon dioxide in supercritical conditions," *Applied Thermal Engineering*, vol. 190, p. 116 816, May 2021, ISSN: 1359-4311. DOI: 10.1016/J.APPLTHERMALENG.2021.116816.

[75] C. E. (E. Brennen, *Fundamentals of multiphase flow*. Cambridge University Press, 2005, p. 345, ISBN: 0521848040.

[76] B. Liu, X. Liu, C. Lu, A. Godbole, G. Michal, and A. K. Tieu, "Multi-phase decompression modeling of CO2 pipelines," *Greenhouse Gases: Science and Technology*, vol. 7, no. 4, pp. 665–679, Aug. 2017, ISSN: 21523878. DOI: 10.1002/ghg.1666.

[77] K. K. Botros, E. Hippert Jr, and P. Craidy, "Measuring decompression wave speed in CO2 mixtures by a shock tube," *Pipelines International*, vol. 16, pp. 22–28, 2013.

[78] Y. Li and J. Deng, "Numerical investigation on the performance of transcritical CO2 two-phase ejector with a novel non-equilibrium CFD model," *Energy*, vol. 238, p. 121 995, Jan. 2022, ISSN: 0360-5442. DOI: 10.1016/J.ENERGY.2021.121995.

[79] A. Elshahomi, C. Lu, G. Michal, X. Liu, A. Godbole, and P. Venton, "Decompression wave speed in CO2 mixtures: CFD modelling with the GERG-2008 equation of state," *Applied Energy*, vol. 140, pp. 20–32, Feb. 2015, ISSN: 03062619. DOI: 10.1016/j.apenergy.2014.11.054.

[80] C. Xiao, Z. Lu, L. Yan, J. Wang, and S. Yao, "Effects of flow velocity on transient behaviour of liquid CO2 decompression during pipeline transportation," *Processes*, vol. 9, no. 2, pp. 1–14, Feb. 2021, ISSN: 22279717. DOI: 10.3390/pr9020192.

Appendix A

Auxiliary figures

A.1 $p - T$ cooling

The total pressure and temperature drop along the axis of the nozzle are plotted in Figure A.1. The results for the narrow nozzle are represented by the red curves, whereas the blue curves represent the wide nozzle. The dashed line is in both cases the temperature and can be read off by means of the right-hand y-axis. The pressure, on the other hand, is shown by the normal lines and uses the left-hand y-axis as the benchmark. The nozzles with the supersonic exits are shown in Figure A.1a, while the shock experiments are shown in Figure A.1b.

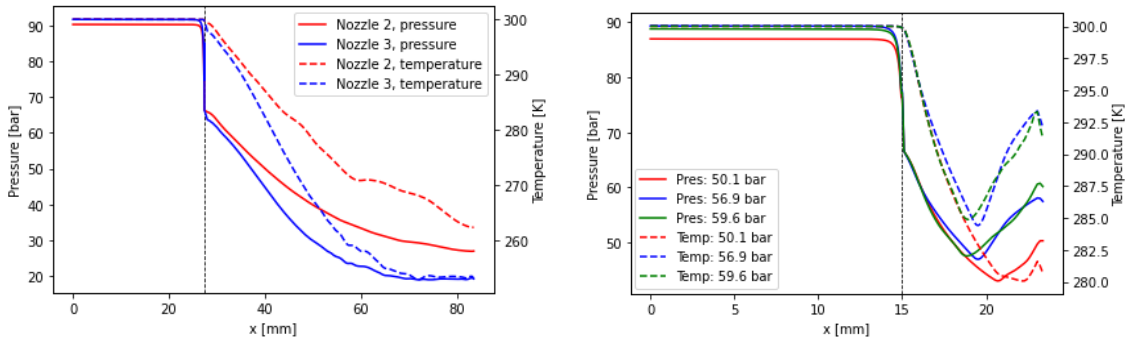

(a) Supersonic exit nozzles

(b) Shock nozzles

Figure A.1: Pressure and temperature plotted along the axis of the nozzles. On the left, the supersonic nozzles. On the right, the nozzles with the presence of the shocks.

Taking the total pressure and temperature drop, an average $°C/\text{bar}$ can be calculated. The outcome of these average calculations is shown in Table A.1 for all three models. A rough average temperature drop of around 0.60 $°C/\text{bar}$ is noticed for the supersonic nozzles in the EMT model. The isenthalpic and 1D Euler models show larger averages, which is expected due to higher vapour fractions. Using

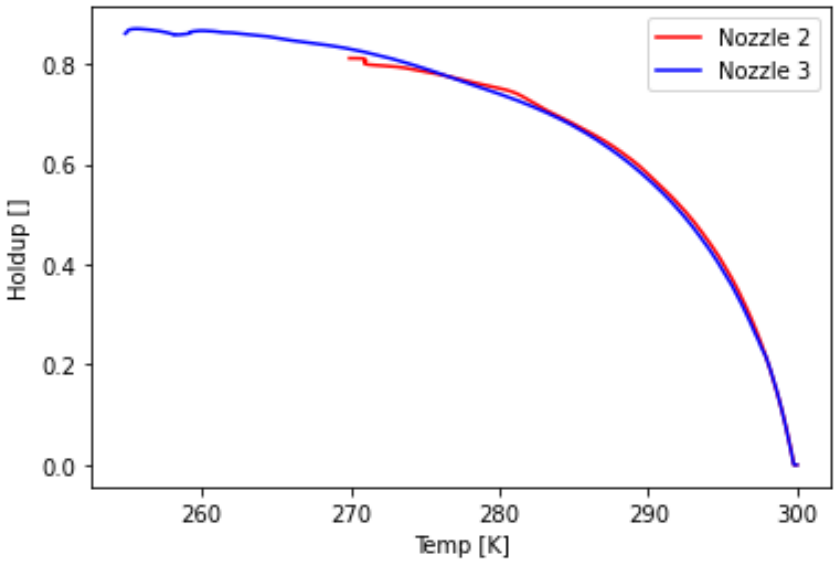

Figure A.2: Vapour holdup fraction for the different nozzles in the case of a supersonic exit. Plotted against the temperature.

this average calculation also for the shock experiments does not seem appropriate. The average values differ significantly from each other and also no cohesion between converging and diverging averages is found.

The simulations for the shock experiments were very unstable in the beginning and a lot of fine-tuning was needed before converging solutions were found. However, the residuals for the simulations did not always reach desirably low values. Although no fluctuations were found in the results anymore, this could be an explanation for the deviations in Table A.2.

Since it was obvious in Figure 4.21a - 4.21b, the depressurisation occurred along the phase line, it is also interesting to see whether the different nozzles have the same path of vaporisation. In a $p-T$ space, the two-phase area is obviously not visible. Different depressurisation behaviours would all show expansion along the phase line.

Therefore, the vapour holdup is plotted against the temperature. This is visible in Figure A.2. It is clear that the different nozzles follow the same path of vaporisation. This implies that the mass transfer mechanism incorporated in the EMT models shows consistent behaviour.

Table A.1: Pressure and temperature differences for the different nozzles. Total temperature drop due to total pressure drop with an average $°C$/bar.

	ΔP [bar]	ΔT [K]	$\left(\frac{\Delta T}{\Delta P}\right)_{\text{Total}}$ [K/bar]
Nozzle 2	74.57	63.06	0.85
Nozzle 3	81.08	76.16	0.94

(a) Isenthalpic model

	ΔP [bar]	ΔT [K]	$\left(\frac{\Delta T}{\Delta P}\right)_{\text{Total}}$ [K/bar]
Nozzle 2	73.82	61.68	0.84
Nozzle 3	80.58	74.85	0.93

(b) 1D Euler model

	ΔP [bar]	ΔT [K]	$\left(\frac{\Delta T}{\Delta P}\right)_{\text{Total}}$ [K/bar]
Nozzle 2	63.38	37.54	0.59
Nozzle 3	72.57	46.73	0.64

(c) EMT model

Table A.2: Pressure and temperature differences for the different nozzles. Total temperature drop due to total pressure drop with an average $°C$/bar. The shockwave case is subdivided into the converging (Con) and diverging (Div) sections.

	ΔP [bar]		ΔT [K]		$\left(\frac{\Delta T}{\Delta P}\right)_{\text{Total}}$ [K/bar]	
	Con	Div	Con	Div	Con	Div
Exit pressure: 50.1 bar	43.93	7.295	19.96	1.54	0.45	0.21
Exit pressure: 56.9 bar	42.36	10.52	15.63	7.68	0.37	0.73
Exit pressure: 59.6 bar	41.22	12.60	15.14	6.36	0.36	0.50

A.2 Additional shock figures

In Chapter 4, only vapour holdup fractions and sonic behaviour were shown for supersonic outflow experiments. This has been done in order to highlight the differences between the various models. The plots of the shock experiments are shown here in Figure A.3.

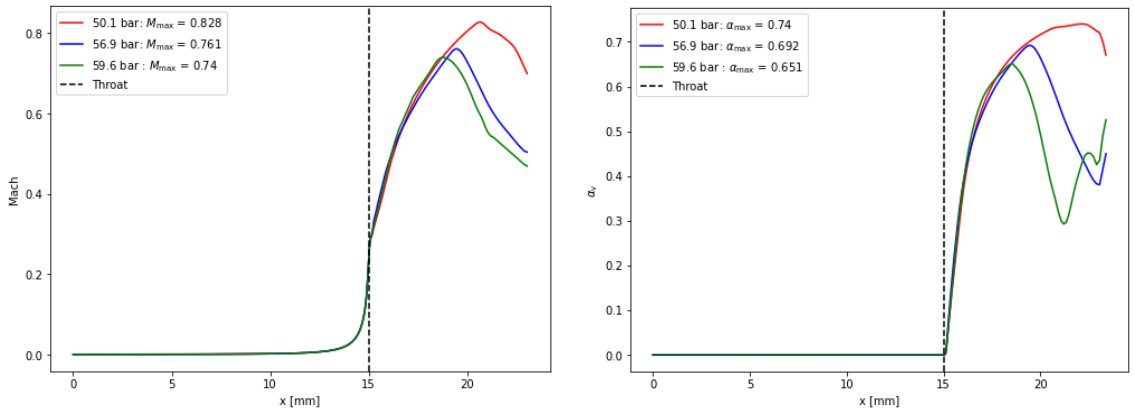

(a) Mach (b) Holdup

Figure A.3: Mach and holdup compare of the shock experiments. The colours show the different exit pressures.

Appendix B

Auxiliary geometries and meshes

The meshes used for the simulations of the shock wave can be seen in Figure B.1. Notice that these meshes did not have extended outlets since the exit pressures were specified for these experiments. Therefore, no prolonged nozzle was necessary.

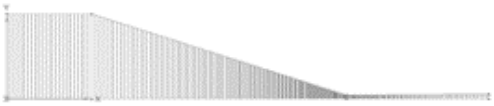

Figure B.1: Nozzle with one dimensional mesh. Finer mesh is observed near the throat. This nozzle is used for the reference case where shock waves are observed [1].

The mesh shown in Chapter 3 was used for the simulations of the supersonic outflow. More specifically, it was the mesh created for nozzle 3, see Table 4.1. The other mesh, for nozzle 2, can be seen below in Figure B.2. Although they look identical, the outlet height is slightly smaller.

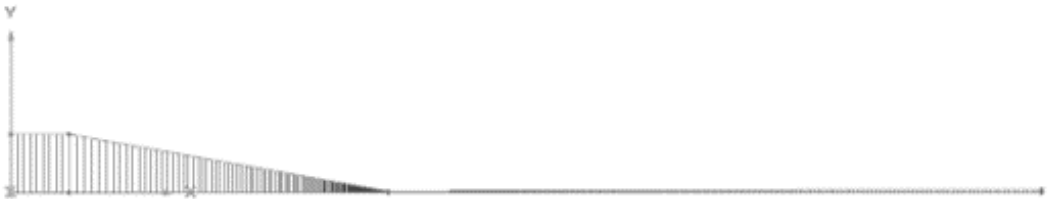

Figure B.2: Nozzle with one dimensional mesh. Finer mesh is observed near the throat. This nozzle is used for the reference case were supersonic outflow is observed for nozzle 2 [2].

For the replication of the numerical results by Nakagawa et al. [1], a different nozzle must be created. This one has the same divergent angle as the nozzle used

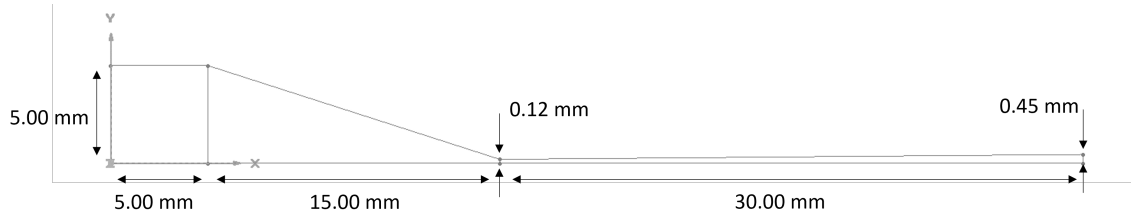

Figure B.3: Geometry nozzle for replication of numerical simulations by Nakagawa et al. [1]

for the experimental data, but a longer divergent section. This nozzle has been used with the Euler model for the results shown in Figure 4.5. The geometry for this nozzle can be found in Figure

For the 2D simulations a different mesh had to be made. The same spacing in the axial direction was used and along the radial direction cells were created. This resulted in a total number of cells of $4.5 \cdot 10^4$. Along the walls, a finer mesh was used to account for wall treatment. The 2D mesh can be seen in Figure B.4

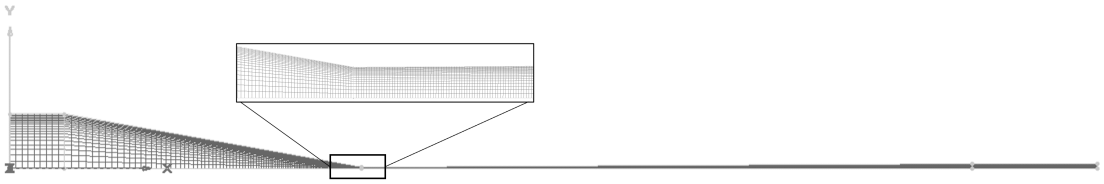

Figure B.4: Nozzle with two dimensional mesh. Finer mesh is observed near the walls and the throat. This nozzle is used for the reference case were supersonic outflow is observed for nozzle 3 [2].

Appendix C

LuT-dimensional analysis

Although using Lookup Tables is required in this scenario, there are several drawbacks to doing so. Aside from mapping just a portion of the thermodynamic lane, outside of which property retrieval is difficult or fails outright, it includes interpolation errors that are significantly bigger the larger the spacing between individual points is. Naturally, expanding the table size excessively is not useful, if only because of the high computational cost necessary for their compiling, creating and reading.

A LuT-dimension analysis was carried out to investigate the influence of the resolution of the LuT. In Table C.1, the different test are detailed. Three different tables were tested with 100x100, 400x400 and 700x700 tables.

These table sizes have been tested on one nozzle with identical conditions. The only change was the Look-up Table size. The results of a sample simulation with these different Look-up Tables can be seen in Figure C.1

Looking at the pressure curves, no significant differences are noticeable. The only minor change is near the shock where the finest table tends to show the shock wave slightly later. This is also confirmed when looking at the differences in the second and the third plot. The major change in difference noticed in the second plot originates primarily from the fact that the shock wave happens at a different location. For the remainder of the nozzle, pressure differences are low (< 0.2 bar). The exact same effect is noticed when examining the temperature. Hence, the error is smaller than the ΔP or ΔT for the 400x400 tables and therefore is a reasonable size.

Table C.1: LuT specifications of the dimensional analysis.

LuT size	ΔP [bar]	ΔT [K]	Size single table [MB]
100x100	1.20	1.20	0.167
400x400	0.30	0.30	2.66
700x700	0.17	0.17	8.14

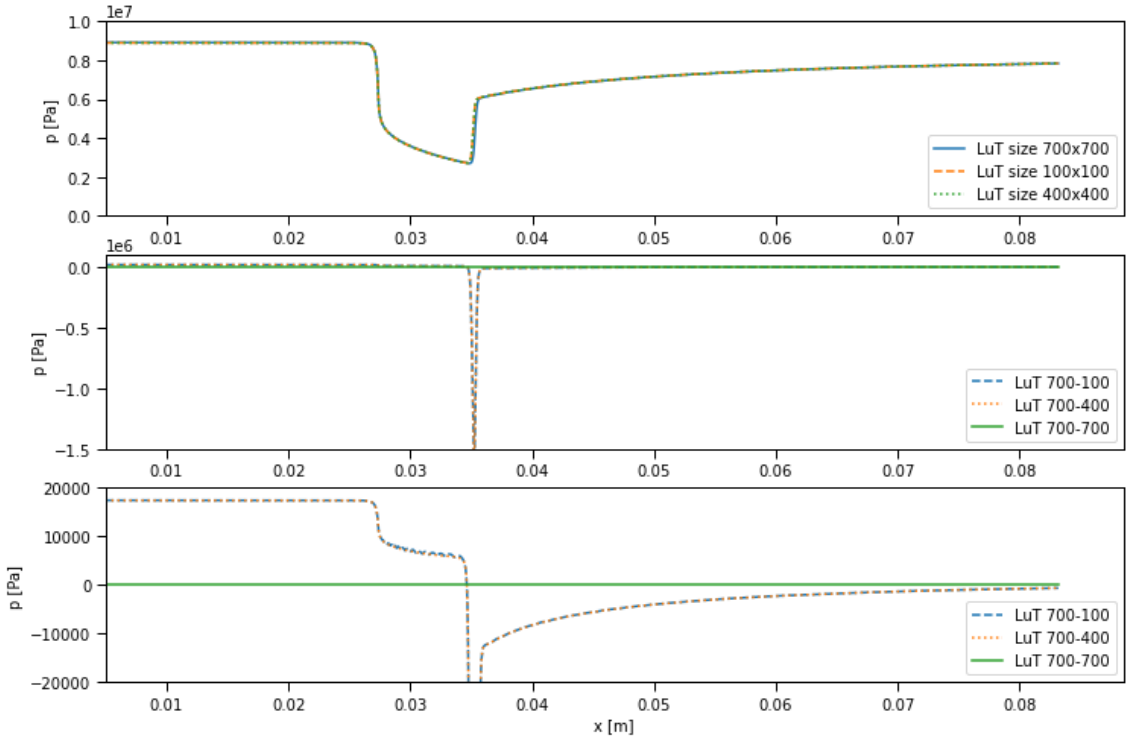

Figure C.1: Pressure curves of a sample simulation with a shock wave in high-temperature, high pressure inlet conditions. The upper plot shows the pressure curves, while the second and the third show these minus the pressure data of the finest Look-up Table (700x700). The third plot is a zoomed in version of the second plot.

Appendix D

Explanatory notes UDFs

Small sections of the UDRGM are shown below in Figure D.1-D.5 to indicate how Fluent handles this C-file. The following parts are shown: error handling, setup, reading LuT data, defining a property and export of property to Fluent.

```
void CO2MONOLUT_error(int err, char *f, char *msg)
{
    if (err)
        usersError("CO2MONOLUT_error (%d) from function: %s\n%s\n" ,err,f,msg);
}
```

Figure D.1: UDRGM: Error handling.

```
void CO2MONOLUT_Setup(Domain *domain, cxboolean vapor_phase, char *species_list,
    int(*messagefunc)(const char *format, ...),
    void (*errorfunc)(const char *format, ...))
{   /*Use this function for any initialization or model setups*/
    usersMessage = messagefunc;
    usersError = errorfunc;
    usersMessage("\nLoading spin_clip Library: %s\n", species_list);
    namefile [0] = ".\\lutsat_clip\\dens_v_sat_clip";
    namefile [1] = ".\\lutsat_clip\\cp_v_sat_clip";
    namefile [2] = ".\\lutsat_clip\\enth_v_sat_clip";
    namefile [3] = ".\\lutsat_clip\\entr_v_sat_clip";
    namefile [4] = ".\\lutsat_clip\\speed_v_sat_clip";
    namefile [5] = ".\\lutsat_clip\\visco_v_sat_clip";
    namefile [6] = ".\\lutsat_clip\\cond_v_sat_clip";
    namefile [7] = ".\\lutsat_clip\\rhot_v_sat_clip";
    namefile [8] = ".\\lutsat_clip\\rhop_v_sat_clip";
    namefile [9] = ".\\lutsat_clip\\entht_v_sat_clip";
    namefile [10] = ".\\lutsat_clip\\enthp_v_sat_clip";
    Tname = ".\\lutsat_clip\\temparr";
    Pname = ".\\lutsat_clip\\pressarr";
    FILE *Tpoint, *Ppoint, *Fpoint;
    Tpoint = fopen (Tname, "r+");
    Ppoint = fopen (Pname, "r+");

    int i, j, q;
```

Figure D.2: UDRGM: Setup handling.

```
    /* Reading properties from ASCII tables*/
    for(i=0; i<NUMPROP; i++)
        {
        Fpoint = fopen (namefile[i], "r+");
        for(j=0; j<DISCR_T; j++)
        {
            for(q=0; q<DISCR_P; q++)
            {
                fscanf (Fpoint, "%lf", &properties [i][q][j]);
            }
        }
        Message("First element: %lf \n", properties[i][0][0]);
        Message("Last element : %lf \n", properties[i][DISCR_P - 1][DISCR_T - 1]);
        Message ("LuT %d loaded \n", i);
        fclose (Fpoint);
        }

}
```

Figure D.3: UDRGM: Reading Look-up Tables.

```
double CO2MONOLUT_enthalpy(cell_t cell, Thread *thread, double T, double density, double P, double yi[])
{
    int ind = 2;
    double h = Interpolant (T, P, ind);
    return h; /*(J/Kg)*/
}
```

Figure D.4: UDRGM: Defining property using interpolation function which is defined elsewhere.

```
/************************************************************************/
/*Auxiliary Mixture Functions*/
/************************************************************************/

UDF_EXPORT RGAS_Functions RealGasFunctionList =
{
    CO2MONOLUT_Setup,                   /*initialize*/
    CO2MONOLUT_density,                 /*density*/
    CO2MONOLUT_enthalpy,                /*enthalpy*/
    CO2MONOLUT_entropy,                 /*entropy*/
    CO2MONOLUT_specific_heat,           /*specific_heat*/
    CO2MONOLUT_mw,                      /*molecular_weight*/
    CO2MONOLUT_speed_of_sound,          /*speed_of_sound*/
    CO2MONOLUT_viscosity,               /*viscosity*/
    CO2MONOLUT_thermal_conductivity,    /*thermal_conductivity*/
    CO2MONOLUT_rho_t,                   /*drho/dT|constp*/
    CO2MONOLUT_rho_p,                   /*drho/dp|constT*/
    CO2MONOLUT_enthalpy_t,              /*dh/dT|constp*/
    CO2MONOLUT_enthalpy_p               /*dh/dp|constT*/
};
/************************************************************************/
```

Figure D.5: UDRGM: Exporting properties to Fluent.